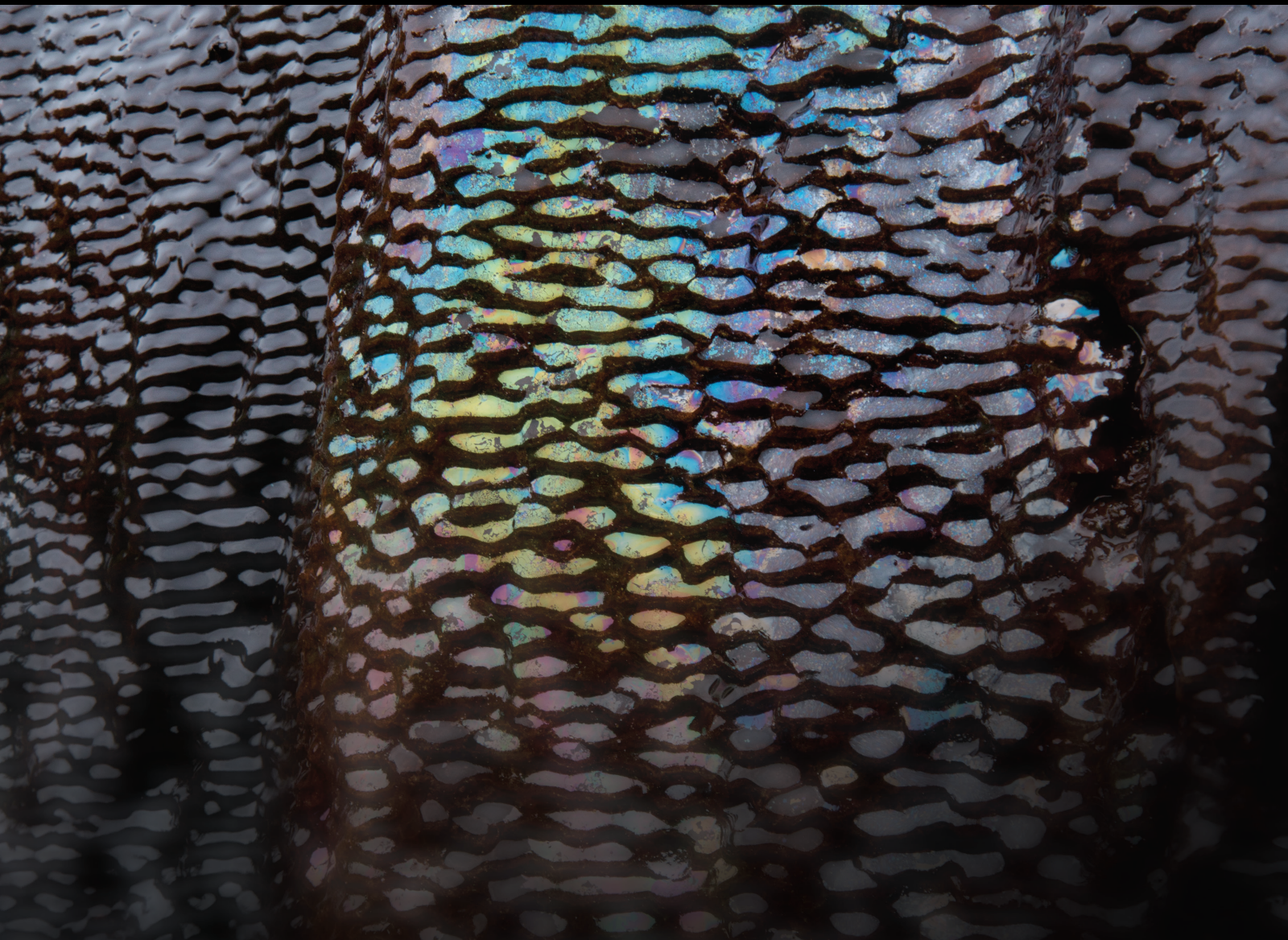


# Advantages, Limitations and Technologies of Recent Advancements in Coal Seam Gas Extraction

Lead Guest Editor: Mandadige S. A. Perera

Guest Editors: Vikram Vishal, Tharaka Rathnaweera, and Wei Wu





---

# **Advantages, Limitations and Technologies of Recent Advancements in Coal Seam Gas Extraction**

**Advantages, Limitations and  
Technologies of Recent Advancements  
in Coal Seam Gas Extraction**

Lead Guest Editor: Mandadige S. A. Perera

Guest Editors: Vikram Vishal, Tharaka  
Rathnaweera, and Wei Wu



---





Copyright © 2020 Hindawi Limited. All rights reserved.

This is a special issue published in "Geofluids." All articles are open access articles distributed under the Creative Commons Attribution License, which permits unrestricted use, distribution, and reproduction in any medium, provided the original work is properly cited.



























# Chief Editor

































Umberta Tinivella, Italy

## Associate Editors

Paolo Fulignati , Italy  
Huazhou Li , Canada  
Stefano Lo Russo , Italy  
Julie K. Pearce , Australia

## Academic Editors

Basim Abu-Jdayil , United Arab Emirates  
Hasan Alsaedi , USA  
Carmine Apollaro , Italy  
Baojun Bai, USA  
Marino Domenico Barberio , Italy  
Andrea Brogi , Italy  
Shengnan Nancy Chen , Canada  
Tao Chen , Germany  
Jianwei Cheng , China  
Paola Cianfarra , Italy  
Daniele Cinti , Italy  
Timothy S. Collett , USA  
Nicoló Colombani , Italy  
Mercè Corbella , Spain  
David Cruset, Spain  
Jun Dong , China  
Henrik Drake , Sweden  
Farhad Ehya , Iran  
Lionel Esteban , Australia  
Zhiqiang Fan , China  
Francesco Frondini, Italy  
Ilaria Fuoco, Italy  
Paola Gattinoni , Italy  
Amin Gholami , Iran  
Michela Giustiniani, Italy  
Naser Golsanami, China  
Fausto Grassa , Italy  
Jianyong Han , China  
Chris Harris , South Africa  
Liang He , China  
Sampath Hewage , Sri Lanka  
Jian Hou, China  
Guozhong Hu , China  
Lanxiao Hu , China  
Francesco Italiano , Italy  
Azizollah Khormali , Iran  
Hailing Kong, China


Karsten Kroeger, New Zealand  
Cornelius Langenbruch, USA  
Peter Leary , USA  
Guangquan Li , China  
Qingchao Li , China  
Qibin Lin , China  
Marcello Liotta , Italy  
Shuyang Liu , China  
Yong Liu, China  
Yueliang Liu , China  
Constantinos Loupasakis , Greece  
Shouqing Lu, China  
Tian-Shou Ma, China  
Judit Mádl-Szonyi, Hungary  
Paolo Madonia , Italy  
Fabien Magri , Germany  
Micòl Mastroicco , Italy  
Agnes Mazot , New Zealand  
Yuan Mei , Australia  
Evgeniy M. Myshakin , USA  
Muhammad Tayyab Naseer, Pakistan  
Michele Paternoster , Italy  
Mandadige S. A. Perera, Australia  
Marco Petitta , Italy  
Chao-Zhong Qin, China  
Qingdong Qu, Australia  
Reza Rezaee , Australia  
Eliahu Rosenthal , Israel  
Gernot Rother, USA  
Edgar Santoyo , Mexico  
Mohammad Sarmadivaleh, Australia  
Venkatramanan Senapathi , India  
Amin Shokrollahi, Australia  
Rosa Sinisi , Italy  
Zhao-Jie Song , China  
Ondra Sracek , Czech Republic  
Andri Stefansson , Iceland  
Bailu Teng , China  
Tivadar M. Tóth , Hungary  
Orlando Vaselli , Italy  
Benfeng Wang , China  
Hetang Wang , China  
Wensong Wang , China  
Zhiyuan Wang , China  
Ruud Weijermars , Saudi Arabia

Bisheng Wu , China  
Da-yang Xuan , China  
Yi Xue , China  
HE YONGLIANG, China  
Fan Yang , China  
Zhenyuan Yin , China  
Sohrab Zendeboudi, Canada  
Zhixiong Zeng , Hong Kong  
Yuanyuan Zha , China  
Keni Zhang, China  
Mingjie Zhang , China  
Rongqing Zhang, China  
Xianwei Zhang , China  
Ye Zhang , USA  
Zetian Zhang , China  
Ling-Li Zhou , Ireland  
Yingfang Zhou , United Kingdom  
Daoyi Zhu , China  
Quanle Zou, China  
Martina Zucchi, Italy


## Contents

---



**Numerical Investigation of Hydraulic Fracture Propagation in Naturally Fractured Reservoirs Based on Lattice Spring Model**

Kaikai Zhao , Pengfei Jiang, Yanjun Feng, Xiaodong Sun, Lixing Cheng, and Jianwei Zheng  
Research Article (18 pages), Article ID 8845990, Volume 2020 (2020)

**Effect of Gas Adsorption on the Application of the Pulse-Decay Technique**

Shaicheng Shen, Xiaochun Li, Zhiming Fang , and Nao Shen  
Research Article (11 pages), Article ID 8872888, Volume 2020 (2020)

**A Crack Propagation Control Study of Directional Hydraulic Fracturing Based on Hydraulic Slotting and a Nonuniform Pore Pressure Field**

Yugang Cheng , Zhaohui Lu, Xidong Du , Xuefu Zhang, and Mengru Zeng  
Research Article (13 pages), Article ID 8814352, Volume 2020 (2020)

## Research Article

# Numerical Investigation of Hydraulic Fracture Propagation in Naturally Fractured Reservoirs Based on Lattice Spring Model

**Kaikai Zhao**<sup>1,2,3</sup>, **Pengfei Jiang**<sup>3,4,5</sup>, **YanJun Feng**<sup>3,4,5</sup>, **Xiaodong Sun**<sup>3,4,5</sup>, **Lixing Cheng**<sup>3,4,5</sup>  
and **Jianwei Zheng**<sup>3,4,5</sup>

<sup>1</sup>Coal Mining and Designing Branch, China Coal Research Institute, Beijing 100013, China

<sup>2</sup>Engineering Geology and Resource Geotechnics Group, Simon Fraser University, Burnaby, BC, V5A 1S6, Canada

<sup>3</sup>State Key Laboratory of Coal Mining and Clean Utilization, Beijing 100013, China

<sup>4</sup>Coal Mining and Designing Department, Tiandi Science and Technology Co., Ltd., Beijing 100013, China

<sup>5</sup>CCTEG Coal Mining Research Institute, Beijing 100013, China

Correspondence should be addressed to Kaikai Zhao; [kaikai\\_zhao@outlook.com](mailto:kaikai_zhao@outlook.com)

Received 31 August 2020; Revised 25 September 2020; Accepted 6 October 2020; Published 24 October 2020

Academic Editor: Mandadige S. A. Perera

Copyright © 2020 Kaikai Zhao et al. This is an open access article distributed under the Creative Commons Attribution License, which permits unrestricted use, distribution, and reproduction in any medium, provided the original work is properly cited.

Hydraulic fracturing has been extensively employed for permeability enhancement in low-permeability reservoirs. The geometry of the hydraulic fracture network (HFN) may have implications for the optimization of hydraulic fracturing operations. Various parameters, including the in situ stress, treatment parameters (injection rate and fluid viscosity), and orientation of natural fractures (NFs), can significantly affect the interactions between hydraulic fracture (HF) and NFs and the final HFN. In this study, a lattice-spring code was employed to determine the impact of various parameters on the geometry of the HFN. The modelling results indicated that with a large stress difference, the global orientation of the fracture propagation was restricted to the direction of maximum principal stress, and the number of fracture branches was reduced. The geometry of the HFN changed from circular to elliptical. In contrast, with an increase in the fluid viscosity/injection rate, the evolution of the geometry of the HFN exhibited the opposite trend. The global orientation of HF propagation tended to remain parallel to the direction of maximum principal stress, regardless of the branching and tortuosity of the fracture. The variations in the ratio of tensile fracture (HF) to shear fracture (shear slip on NF) can be significant, depending on the stress state, treatment parameters, and preexisting NF network, which determine the dominant stimulation mechanism. This study provides insight into the HF propagation in naturally fractured reservoirs.

## 1. Introduction

Hydraulic fracturing treatment has been widely applied in the shale gas reservoir [1] as well as coal seam gas reservoir [2]. It is increasingly being used for preconditioning of the orebody in cave mining [3]. In the naturally fractured formation, a hydraulic fracture (HF) may encounter natural fractures (NFs) of various scales, such as joints, bedding planes, and faults. Several types of interactions (e.g., diversion, offsetting, and crossing) can occur when the HF encounters the NF. Therefore, hydraulic fracturing treatment in a naturally fractured reservoir may give rise to a complex hydraulic fracture network (HFN) instead of a symmetric, planar, biwing HF [4]. By predicting the HFN geometry, the accuracy of

the hydrofracture simulation for fractured reservoirs can be improved [5].

Various parameters, including the in situ stress, treatment parameters (injection rate and fluid viscosity), and geometric and mechanical properties of the NF, can significantly affect the HF–NF interactions and the final HFN. Numerous experiments have been performed to investigate the interactions between HFs and NFs. Zhou et al. [6, 7] argued that the stress difference, shear strength of the NF, and approach angle (intersection angle between the HF and NF) are crucial factors determining the HF propagation behavior in the fractured formation. HFs tend to cross preexisting NFs under a large stress difference and approach angle, whereas they undergo diversion/deflection due to the NF under a small



stress difference and approach angle. In laboratory experiments performed by Beugelsdijk et al. [8] With a small value of the product of the injection rate  $Q$  and the fluid viscosity  $\mu$  ( $Q\mu$ ), fluid tended to leak into the NFs, resulting in tortuous HF propagation paths following the NFs. With a high  $Q\mu$  value, the HF tended to cross most NFs, and the overall propagation path was relatively straight. Zou et al. [9] performed a series of experiments to investigate HF propagation using computed tomography scanning technology. The results indicated that the NF network (NFN) was activated for a small horizontal stress difference of  $<6$  MPa, and a simple transverse fracture pattern was observed for a large horizontal stress difference of  $>9$  MPa. Additionally, a dominant HF was observed for treatment with a high injection rate, whereas the NFN was activated to a large extent under a low injection rate. In the field, the HFN has been characterized by combining microseismic analysis with surface and downhole tilt fracture mapping [10]. As shown in Figure 1, field observations revealed varying degrees of complexity, ranging from a simple, relatively planar fracture to a complex fracture network. Mayerhofer et al. [11] proposed the concept of the stimulated reservoir volume (three-dimensional (3D) volume of the microseismic event cloud) as a correlation parameter for good performance. The stimulated reservoir volume can approximate the size of the created HFN. Because of the limitations regarding the size of the rock sample and the precision of the measurement device, it is challenging to perform a sensitivity analysis or quantitatively evaluate the effects of various parameters on the interactions between an HF and multiple NFs, as well as the final HFN.

Comprehensive numerical models have been proposed to investigate the HF propagation in naturally fractured formations, which can be categorized according to their numerical methods: the finite element method (FEM), including the extended finite element method (XFEM) [12, 13] and cohesive zone method [14, 15], boundary element method (BEM) [16], displacement discontinuity method (DDM) [17, 18], distinct element method (DEM) [19, 20], and lattice method [21]. The simulation methods for hydraulic fracturing have recently been comprehensively reviewed [22–24]. Taleghani and Olson [25] presented an XFEM model considering the interactions between HF and NFs. The modelling results indicated that the fracture-pattern complexity is significantly affected by the stress anisotropy, rock toughness, and NF strength, as well as the orientation of the NF. Abbas et al. [26] adopted an XFEM model to examine the effects of different combinations of parameters (i.e., formation moduli, far-field stresses, and injection rates) on the HF height and the size of the HF opening. Ghaderi et al. [27] used the XFEM method to simulate the deformation of the NF during the approaching stage of the HF. The results indicated that the tensile and shear debonding of the NF change with respect to the angle and distance from an NF. Zhang et al. [16] investigated the HF deflection behaviors at bedding interfaces using a two-dimensional BEM model. The HF deflection and fluid invasion depend on various parameters, including the elastic-modulus contrasts, in situ stresses, interfacial frictional coefficients, and fluid viscosities. Olson [28] presented a complex fracture network model to simulate HF propagation and the interaction between an

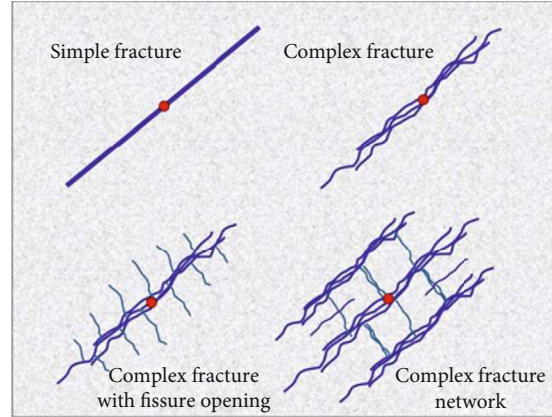


FIGURE 1: Schematics of the levels of complexity observed in HF [4].

HF and an NF using a pseudo-3D DDM. Kresse and Weng [18] developed an unconventional fracture model for simulating HF propagation, rock deformation, and fluid flow in a complex fracture network.

The DEM has been widely adopted in various rock engineering projects [29, 30]. The typical DEM can effectively reproduce the open/slip of an NF and the interaction between blocks and an HF. However, no new HF propagation beyond the prebuilt trajectories can be reproduced. The synthetic rock mass (SRM) approach compensates for the deficiency of the prebuilt trajectory in conventional DEM models [31]. The SRM scheme has been incorporated in the lattice scheme code XSite [32]. Bakhshi et al. [33] adopted XSite to investigate the intersection of an HF with an NF with consideration of the effects of the intersection angle and the mechanical properties of the NF. Zhao et al. [34] employed XSite to simulate the 3D interaction between an HF and an NF, with consideration of the effects of the stress difference, treatment parameters, and NF properties. Liu et al. [35] adopted XSite to study the stress interference between multiple HF in a horizontal well. Wan et al. [36] used XSite to investigate the effects of the rock properties and in situ stresses on HF containment. In most of the foregoing studies, the wellbore/open-hole was treated as an injection point or a predefined fracture path, and the effects of stress concentration around the wellbore (and potentially on the fracture tortuosity and branching near the wellbore) were neglected.

This study focused on the numerical modelling of the HF propagation in a naturally fractured formation and the evolution of the HFN geometry. A series of XSite simulation was conducted to investigate the effects of the stress difference ( $\Delta\sigma = \sigma_1 - \sigma_3$ ), the treatment parameters (fluid viscosity and injection rate), and the orientation of the NF. Additionally, the HF propagation in several typical NFNs was analyzed.

## 2. Modelling Methodology

The code XSite, based on the lattice method (see Figure 2) and SRM approach (see Figure 3), is a more computationally

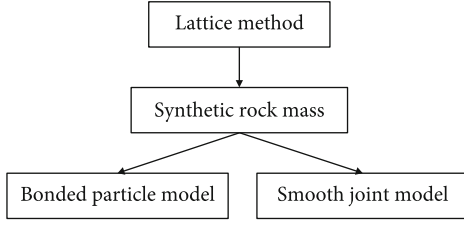


FIGURE 2: Schematic diagram of lattice simulation method.

efficient version of the 3D particle flow code. In SRM, the bonded particle model (BPM) was employed to represent intact material, and the smooth joint model (SJM) was used to describe the joints behaviors [32]. Lattice simulation is a simplification of the BPM in which the particles and contacts are replaced by nodes and springs.

There are two methods used to generate the springs that connect the nodes: regular and Voronoi. Voronoi lattice tessellation is utilized in the presented simulations, with the springs placed based on Voronoi tessellation in 3D space, where the springs are created at common faces of the discretization domains. The lattice is created by multiplication of the periodic brick (p-brick) in three orthogonal directions. The p-brick is a quasirandom arrangement of nodes within a cube of unit edge length. The final model geometry is achieved by trimming of the “excess” lattice extending outside the analyzed domain [32].

**2.1. Mechanical Formulation.** As shown in Figure 4, the lattice is composed of numerous quasirandomly distributed nodes connected by springs. Joints are overlaid on the lattice using the SJM methodology.

The central difference method is employed to compute the transitional degrees of freedom [32]:

$$\dot{u}_i^{(t+\Delta t/2)} = \dot{u}_i^{(t-\Delta t/2)} + \sum F_i^{(t)} \frac{\Delta t}{m}, \quad (1)$$

$$u_i^{(t+\Delta t)} = u_i^{(t)} + \dot{u}_i^{(t+\Delta t/2)} \Delta t, \quad (2)$$

where  $\dot{u}_i^{(t)}$  and  $u_i^{(t)}$  represent the velocity and position of component  $i$  ( $i = 1, 3$ ) at time  $t$ .  $\sum F_i^{(t)}$  represent the sum of all the force components  $i$  acting on a node of mass  $m$ , with time step  $\Delta t$ .

The angular velocities of component  $i$  at time  $t$  are calculated using

$$\omega_i^{(t+\Delta t/2)} = \omega_i^{(t-\Delta t/2)} + \frac{\sum M_i^{(t)}}{I} \Delta t, \quad (3)$$

where  $\sum M_i^{(t)}$  is the sum of all moment-components acting on the node of moment of inertia  $I$ .

The force change in the spring is determined by the displacements of the node [32]:

$$F^N \leftarrow F^N + \dot{u}^N k^N \Delta t, \quad (4)$$

$$F_i^S \leftarrow F_i^S + \dot{u}_i^S k^S \Delta t, \quad (5)$$

where  $N$  represents “normal,”  $S$  represents “shear,”  $F$  represents the spring force.  $k^N$  and  $k^S$  represent the spring normal and shear stiffness, respectively. If the force exceeds the spring strength, the spring breaks and a microcrack is formed.

Joint slip and opening follow the relationship [37]

$$\begin{aligned} &\text{If } F^n - pA < 0 \text{ then } F^n = 0, F_i^s = 0, \\ &\text{else } F_i^s \leftarrow \frac{F_i^s}{|F_i^s|} \min \{ (F^n - pA) \tan \phi, |F_i^s| \}, \end{aligned} \quad (6)$$

where  $F^n$  represents the normal force,  $F_i^S$  represents the shear force vector,  $p$  represents the pressure,  $A$  represents the apparent area, and  $\phi$  represents the friction angle.

The following relationship determines the bonded joint status: if  $F^n - pA + \sigma_c A < 0$  or  $|F_i^s| > \tau_c A$ , the bond fails in tension or shear (where  $\sigma_c$  is the bond tensile strength,  $\tau_c$  is the bond shear strength), else,  $F_i^s \leftarrow F_i^s$ , the bond remains intact.

**2.2. Flow Formulation.** As shown in Figure 5, the flow in HF is simulated using fluid elements linked by pipes. The fluid elements act as microcracks which are positioned at the centers of the broken springs or springs overlapped by the joint.

Lubrication theory is used to calculate the flow rate from node A to node B along a pipe:

$$q = \beta k_r \frac{a^3}{12\mu_f} [p^A - p^B + \rho_w g(z^A - z^B)], \quad (7)$$

where  $a$  represents the aperture;  $\mu_f$  represents the fluid viscosity;  $p^A$  and  $p^B$  represents the hydraulic pressures at nodes “A” and “B,” respectively;  $z^A$  and  $z^B$  represents the elevations of nodes “A” and “B,” respectively;  $\rho_w$  represents the fluid density;  $g$  represents the gravitational acceleration; and  $\beta$  is a calibration parameter that reflects the conductivity.

The relative permeability,  $k_r$ , is a function of saturation,  $s$ :

$$k_r = s^2(3 - 2s), \quad (8)$$

The pressure increment,  $\Delta P$ , during the flow timestep,  $\Delta t$  is calculated as

$$\Delta P = \frac{Q}{V} K_f \Delta t_f, \quad (9)$$

where  $Q$  is the sum of flow rate from the pipes connected to the fluid element,  $V$  is the volume of the fluid element, and  $K_f$  is the apparent fluid element bulk modulus.

**2.3. Hydromechanical Coupling.** The fluid flow and mechanical process are fully coupled (see Figure 6). The mechanical deformation and damage are computed based on the variation in fluid pressure. In contrast, the variation in fluid pressure depends on the mechanical deformation. The HF permeability is decided by the HF aperture and mechanical deformation.

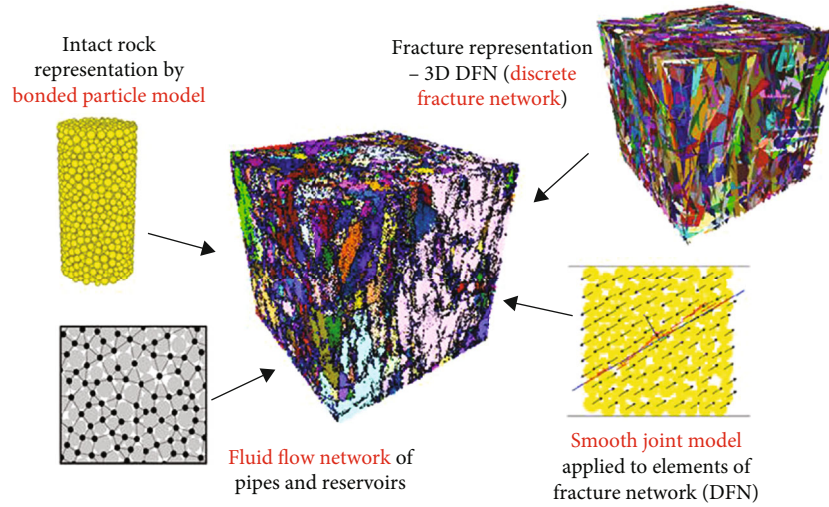


FIGURE 3: Schematic diagram of the synthetic rock mass (SRM) approach [21].

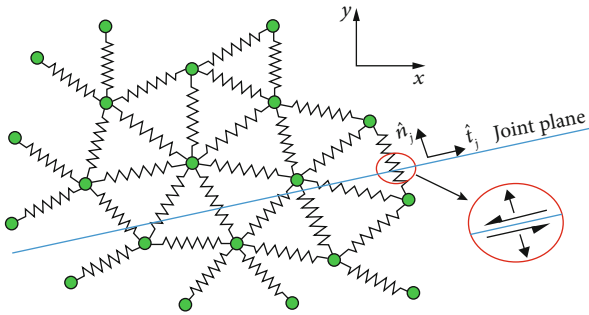


FIGURE 4: Schematic of a lattice array [37].

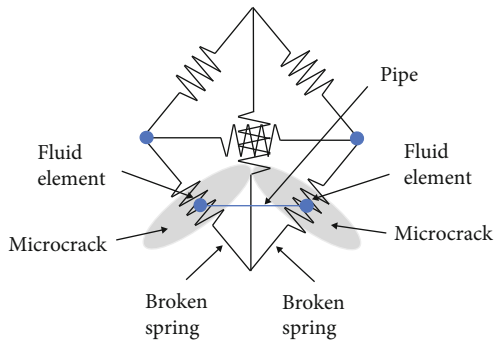


FIGURE 5: Schematic of the pipe network [32].

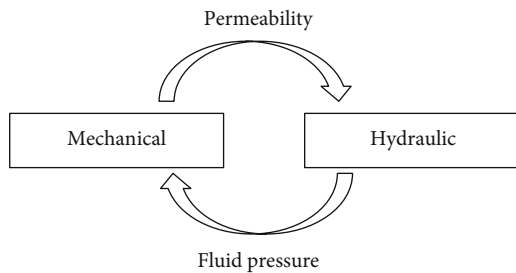


FIGURE 6: Couplings between mechanical and hydraulic processes.

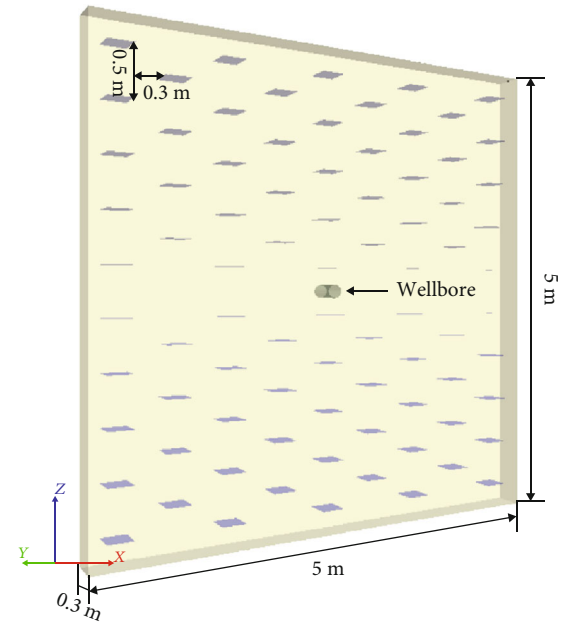


FIGURE 7: Setup of the base model.

**2.4. Fracture Propagation Criteria.** The criteria for HF propagation are based on an  $J$ -integral formulation. The stress intensity factor,  $K_I$ , can be calculated as

$$K_I = \sqrt{JE}, \quad (10)$$

where  $E$  represents the Young's modulus. If  $K_I < K_{IC}$  (where  $K_{IC}$  is the rock toughness); then, the spring tensile strength is utilized to detect spring failure. Otherwise,  $K_I$  is compared to  $K_{IC}$  to detect spring failure.

**2.5. Model Setup.** Figure 7 shows the typical model setup. The dimensions of the rock mass were  $5 \text{ m} \times 5 \text{ m} \times 0.3 \text{ m}$ . NFs with dimensions of  $0.25 \text{ m} \times 0.25 \text{ m}$  were evenly distributed in the rock mass. The initial aperture of the NFs was

TABLE 1: Mechanical and hydraulic model input parameters.

Categories	Variables	Values
In situ stress	Stress difference, $\Delta\sigma$ (MPa)	0, 2.5, 5, 7.5, 10
Treatment parameters	Injection rate, $Q$ ( $\text{m}^3/\text{s}$ )	0.002, 0.003, 0.004, 0.005, 0.007
	Fluid viscosity, $\mu$ (mPa-s)	1, 2, 3, 4, 5
Natural fracture	Dip angle, $\theta$ ( $^\circ$ )	0, 15, 30, 45, $60^\circ$
	Young's modulus, $E$ (GPa)	11.74
Intact rock	Poisson's ratio, $\nu$	0.221
	Tensile strength, $\sigma_t$ (MPa)	7.5
	UCS, $\sigma_c$ (MPa)	75

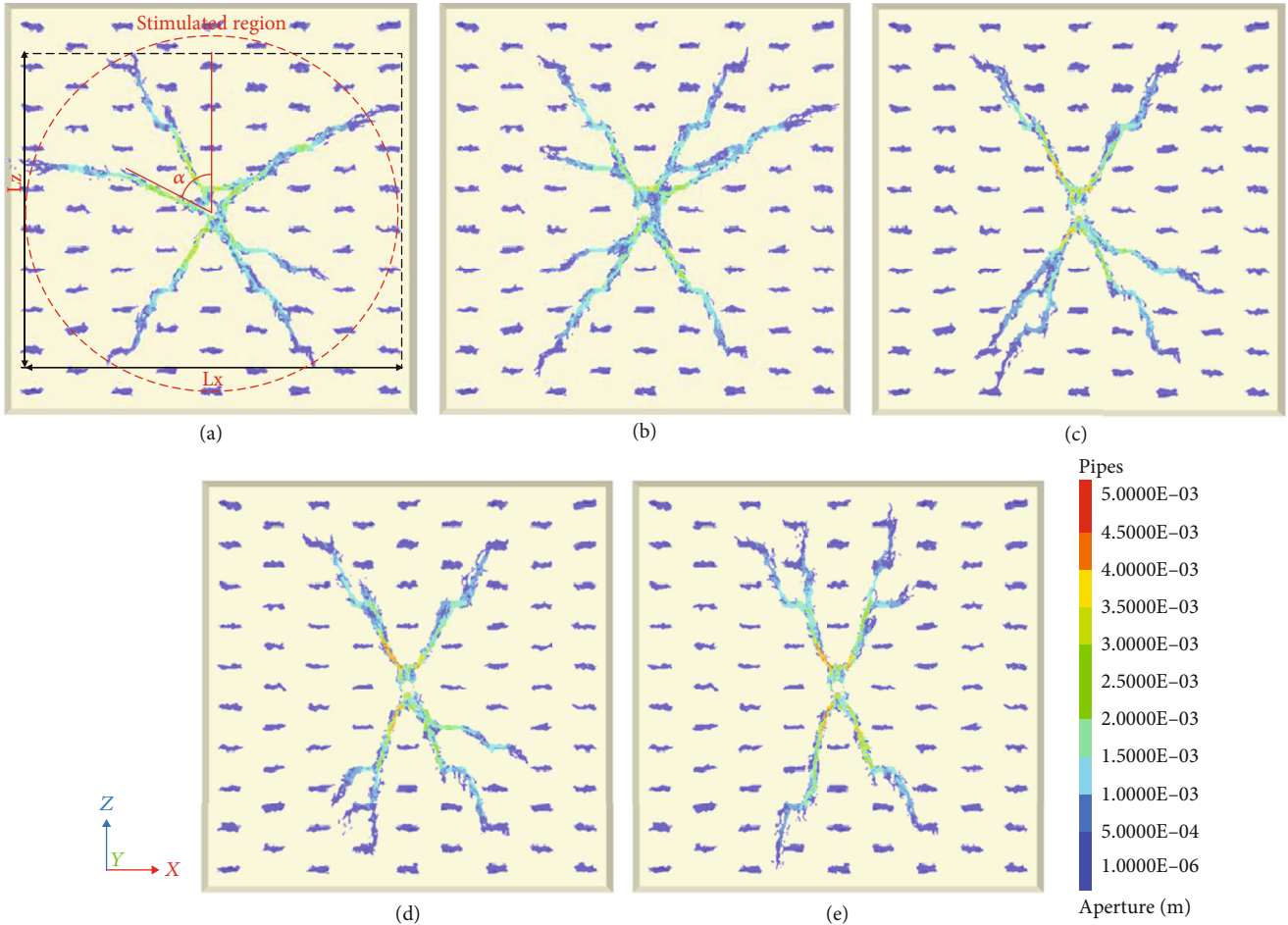


FIGURE 8: HF propagation in the NFN with varying stress differences: (a) 0 MPa, (b) 2.5 MPa, (c) 5 MPa, (d) 7.5 MPa, and (e) 10 MPa.

0.1 mm. A wellbore was placed at the center of the model, parallel to the  $y$ -axis. The wellbore had a radius of 0.075 m and a length of 0.3 m. The horizontal stress was set as  $\sigma_x = \sigma_y = 5$  MPa for all the models. The mechanical and hydraulic parameters for the typical model are presented in Table 1.

### 3. Results

3.1. *Effect of Stress Difference.* For the five models, the vertical stress,  $\sigma_z$ , was set as 5, 7.5, 10, 12.5, and 15 MPa, and  $\sigma_x =$

$\sigma_y = 5$  MPa. The corresponding stress differences were 0, 2.5, 5, 7.5, and 10 MPa, respectively. Simulations were conducted under a constant injection rate of  $0.005 \text{ m}^3/\text{s}$  and a fluid viscosity of 1 mPa-s for 1 s.

As shown in Figure 8, multiple radial branches from the wellbore were simulated, and the tortuosity of the propagation pathway due to the interactions between the NF and the HF was determined. The NF locally altered the HF propagation pathway through the diversion of the HF or induced branching of the HF. As the stress difference changed from 0 to 10 MPa, the dominant propagation direction of the HFN

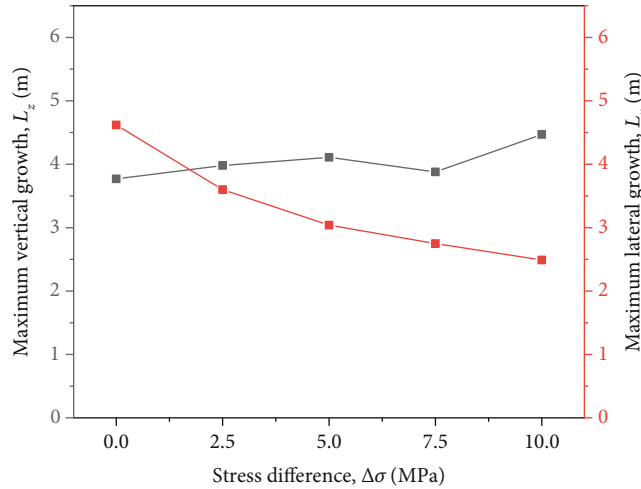


FIGURE 9: Variations of the maximum vertical growth ( $L_z$ ) and lateral growth ( $L_x$ ) under varying stress differences.

became more evident, tending to follow the direction of maximum principal stress. The geometry of the stimulated region (represented by red dotted lines) changed from circular to elliptical, and the long axes tended to be along the direction of maximum principal stress. More branches were observed in small-stress-difference cases than in large-stress-difference cases. The branches were inhibited under a large stress difference, and the dominant propagation direction was restricted to the direction of maximum principal stress.

Figure 9 shows the variations in the maximum vertical growth ( $L_z$ ) and maximum lateral growth ( $L_x$ ) of the HFN for the five models. With an increase in the stress difference,  $L_x$  decreased from 4.62 to 2.49 m (by 2.13 m). Conversely,  $L_z$  increased with an increase in the stress difference (except for the discrete points, the case of  $\Delta\sigma = 7.5$  MPa was examined). For the case of  $\Delta\sigma = 0$  MPa,  $L_x$  was greater than  $L_z$ . When the stress difference exceeded zero,  $L_z$  was greater than  $L_x$ . Moreover, the difference between  $L_z$  and  $L_x$  increased as the stress difference increased from 2.5 to 10 MPa.

Figure 10 shows the variation of the maximum deviation angle  $\alpha$  (maximum angle between the branching and the direction of  $\sigma_1$ ) for the five models. In general,  $\alpha$  decreased with the increasing stress difference.  $\alpha$  decreased significantly (by  $31^\circ$ ) as the stress difference increased from 0 to 5 MPa.  $\alpha$  decreased slightly (by  $13^\circ$ ) as the stress difference increased from 5 to 10 MPa.

**3.2. Effect of Fluid Injection Rate.** Five models were used for the simulations, with assumed injection rates of 0.002, 0.003, 0.004, 0.005, and  $0.007 \text{ m}^3/\text{s}$ . The volume of the injection fluid was  $0.005 \text{ m}^3$  for all the models. The other parameters were as follows:  $\sigma_x = \sigma_y = 5 \text{ MPa}$ ,  $\sigma_z = 7.5 \text{ MPa}$ , and  $\mu = 1 \text{ mPa}\cdot\text{s}$ .

As shown in Figure 11, in general, the geometry of the stimulated region changed from elliptical to circular with an increase in the injection rate. Additionally, there were fewer primary branches at lower injection rates (see Figures 8(a) and 8(b)). Four primary branches were observed in the lowest injection rate case ( $Q = 0.002 \text{ m}^3/\text{s}$ ), and each branch was longer than the corresponding branch in the

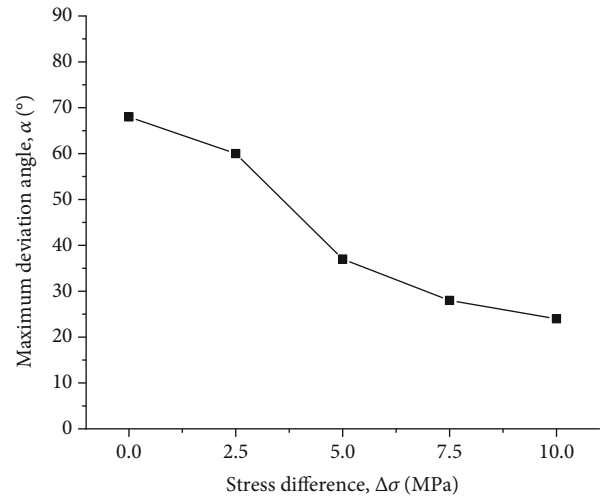


FIGURE 10: Variation of the maximum deviation angle ( $\alpha$ ) for varying stress differences.

highest injection rate case ( $Q = 0.007 \text{ m}^3/\text{s}$ ). The HF mainly propagated along the direction of  $\sigma_1$  for low injection rates. However, no clear dominant propagation direction was observed at the highest injection rate ( $Q = 0.007 \text{ m}^3/\text{s}$ ).

As shown in Figure 12, the  $L_z$  was greater than the  $L_x$  for all five models, and among the models, the difference between the  $L_z$  and the  $L_x$  was the smallest for  $Q = 0.007 \text{ m}^3/\text{s}$ .

As shown in Figure 13,  $\alpha$  increased with the injection rate. There was no significant variation in  $\alpha$  as the injection rate increased from 0.002 to  $0.004 \text{ m}^3/\text{s}$ . However, there was a significant increase ( $53^\circ$ ) in  $\alpha$  as the injection rate increased from 0.004 to  $0.007 \text{ m}^3/\text{s}$ .

**3.3. Effect of Fluid Viscosity.** Five models were used for the simulations, with hydraulic fracturing fluid viscosities of 1, 2, 3, 4, and  $5 \text{ mPa}\cdot\text{s}$ . The stress state was set as follows:  $\sigma_x = \sigma_y = 5 \text{ MPa}$ ,  $\sigma_z = 7.5 \text{ MPa}$ . The simulations were conducted under a constant injection rate of  $0.002 \text{ m}^3/\text{s}$  for 2.5 s.

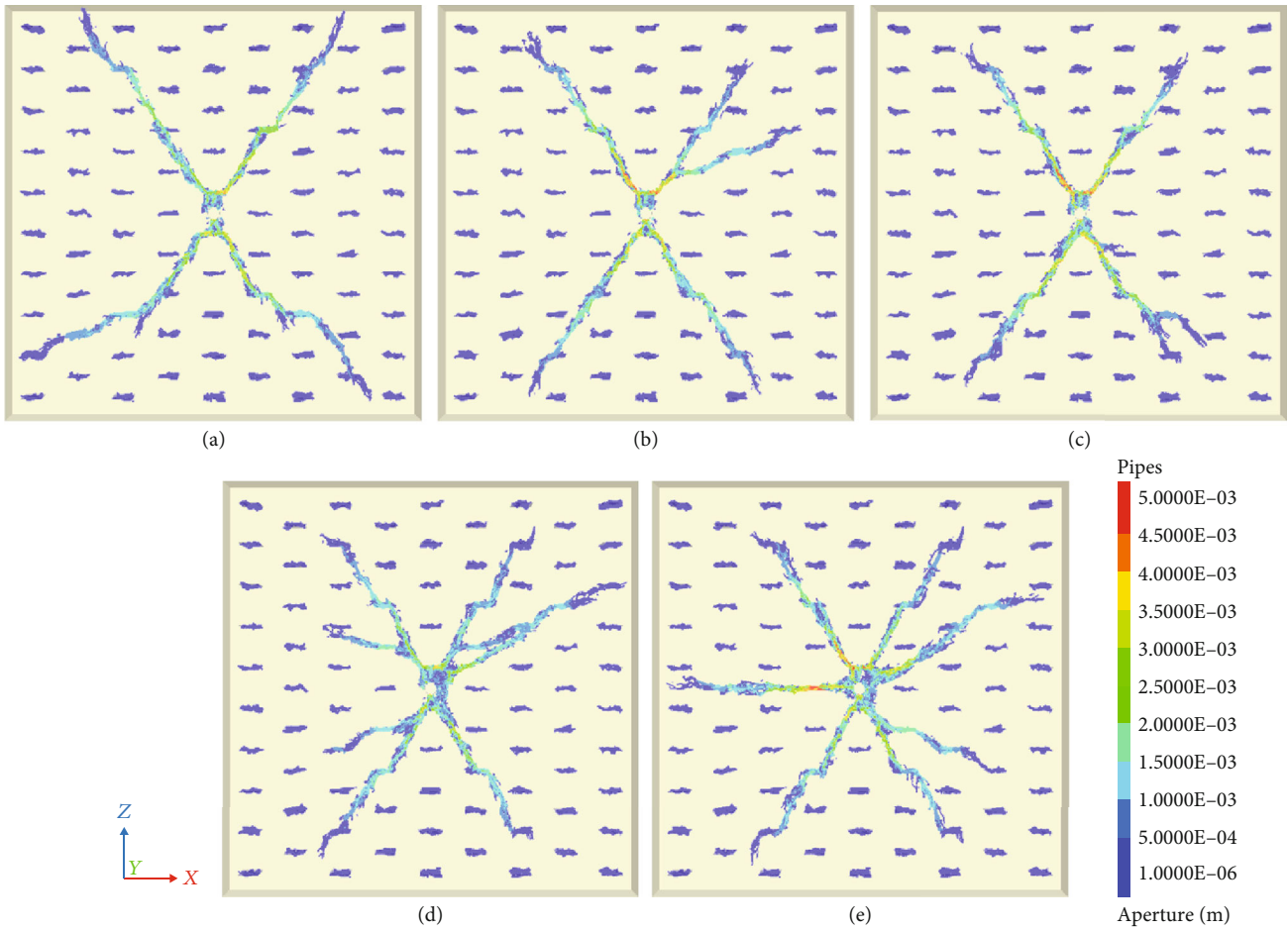


FIGURE 11: HF propagation in the NFN with injection rates of (a) 0.002 m<sup>3</sup>/s, (b) 0.003 m<sup>3</sup>/s, (c) 0.004 m<sup>3</sup>/s, (d) 0.005 m<sup>3</sup>/s, and (e) 0.007 m<sup>3</sup>/s.

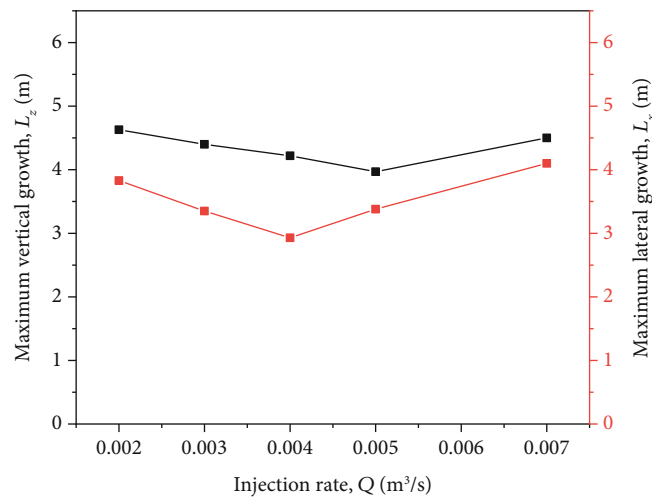


FIGURE 12: Variations of the maximum vertical and lateral growth for different injection rates.

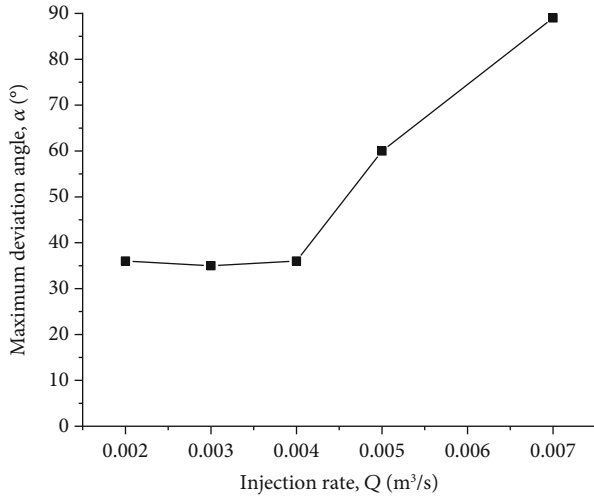


FIGURE 13: Variation of the maximum deviation angle for different injection rates.

As shown in Figure 14, the geometry of the stimulated region changed from elliptical to circular as the fluid viscosity increased from 1 to 5 mPa·s. The size of the stimulated region decreased with the increasing fluid viscosity. Additionally, more branches were induced under treatment with higher-viscosity fluids. The HF mainly propagated along the direction of  $\sigma_1$  for cases with a relatively low-viscosity fluid. However, no dominant propagation direction was observed for the high-viscosity cases of  $\mu = 4$  and 5 mPa·s.

As shown in Figure 15,  $L_z$  was greater than  $L_x$  (except for the case of  $\mu = 4$  mPa·s), and the difference between  $L_z$  and  $L_x$  for the high-fluid viscosity cases of  $\mu = 3, 4,$  and 5 mPa·s was smaller than that for the lower-fluid viscosity cases of  $\mu = 1$  and 2 mPa·s.

As shown in Figure 16,  $\alpha$  tended to increase with the fluid viscosity. A significant increase ( $53^\circ$ ) in  $\alpha$  was observed when the fluid viscosity increased from 2 to 4 mPa·s. The deviation angle was maximized (approximately  $90^\circ$ ) in the high-fluid viscosity cases of  $\mu = 4$  and 5 mPa·s.

**3.4. Effect of NF Orientation.** Five models were used for the simulations, with dip angles of  $0^\circ, 15^\circ, 30^\circ, 45^\circ,$  and  $60^\circ$ . The angles between the NFs and the direction of  $\sigma_1$  were  $90^\circ, 75^\circ, 60^\circ, 45^\circ,$  and  $30^\circ$ , respectively. The stress state was as follows:  $\sigma_x = \sigma_y = 5$  MPa,  $\sigma_z = 5.5$  MPa. Simulations were performed under a constant injection rate of  $0.0005 \text{ m}^3/\text{s}$  for 2 s.

As shown in Figure 17, the HFN geometry varied significantly with changes in the NF dip angle. The direction of the long axis of the stimulated region changed from subhorizontal to subvertical as the NF dip angle increased from  $0^\circ$  to  $60^\circ$ . As shown in Figure 14(a), the two HF branches were initiated at the wellbore and then encountered the two NFs closest to the wellbore. Fluid invasion into the two NFs occurred, causing the open and shear slip of the NFs and then extending from the edges of the NFs. This process occurred again when the HF encountered the next NF. Thus, a step-like HFN was formed in the case of  $\theta = 0^\circ$ . With an increase in the dip angle (and a corresponding reduction in the angle between the NF

and the direction of  $\sigma_1$ ), the number of primary branches decreased, and the main propagation direction of the HF network became closer to the direction of  $\sigma_1$ . There were four primary branches in the case of  $\theta = 0^\circ$ , whereas only two branches were observed for  $\theta = 60^\circ$ .

As shown in Figure 18, as the dip angle increased from  $0^\circ$  to  $60^\circ$ ,  $L_z$  decreased from 3.06 to 0.84 m (by 2.22 m). Conversely,  $L_x$  increased from 1.66 to 4.72 m. In the case of  $\theta = 0^\circ$ ,  $L_x$  was greater than  $L_z$ , whereas  $L_z$  exceeded  $L_x$  for  $\theta > 15^\circ$ . The maximum difference between  $L_z$  and  $L_x$  occurred for  $\theta = 60^\circ$ .

Taking case  $\theta = 45^\circ$  as an example for detailed investigation, Figure 19 shows the microcracks (tensile failure of intact rock) and slip event (shear failure in NF). The HFN comprised the tensile failure in the intact rock and the shear failure in the connected NFs. The connected NFs appeared to be fully activated by shear slippage. Additionally, isolated NFs were subjected to shear failure, and slip events were observed on isolated NFs.

The displacement field is shown in Figure 20. Three primary branches divided the intact block into three separate blocks, which were characterized by different displacement fields. In general, the displacement decreased with the increasing distance from the wellbore. Most of the block experienced displacement of  $>0.2$  mm. The largest displacement was observed for block 3.

**3.5. HF Propagation in Different NFNs.** We investigated the HF propagation behavior in different NFNs and considered three types of simplified NFNs. The type A NFN comprised several large, parallel-distributed NFs (Figure 21). In the type B NFN, there were vertical NFs between adjacent horizontal NFs, and all the NFs were isolated from each other (Figure 22). In type C NFN, the vertical NFs were connected with the horizontal NFs (Figure 23). The rock mass volume was  $9 \text{ m} \times 9 \text{ m} \times 0.6 \text{ m}$ . A starter crack with a radius of 0.15 m was located at the center of the model, normal to the  $x$ -axis. The stress state was as follows:  $\sigma_z = 13$  MPa,  $\sigma_x = \sigma_y = 5$ . Simulations were conducted under the injection rate of  $Q = 0.003 \text{ m}^3/\text{s}$  for 12 s.

As shown in Figure 21(b), a vertical HF was induced and crossed all the horizontal NFs, yielding a fishbone-like HFN. In general, the aperture of the horizontal NF decreased with the increasing distance from the starter crack (the injection point). For instance, the two horizontal NFs closest to the injection point had greater apertures ( $>1$  mm) than the other horizontal NFs. Note that the aperture is varied in along the horizontal NF plane. Figure 21(c) shows the approximately radial distribution of the fracture fluid pressure, which decreased with increasing distance from the injection point. Figure 21(d) shows the shear slip on the horizontal NFs. Among the NFs, the largest shear slip was observed on the two horizontal NFs closest to the injection point.

As shown in Figure 22(b), the vertical flow pathway contained the newly induced HF and several vertical NFs. The flow network did not connect most of the vertical NFs. No significant difference in the fracture aperture was observed in comparison with type A. The approximately radial distribution pattern of the fracture fluid pressure is presented in

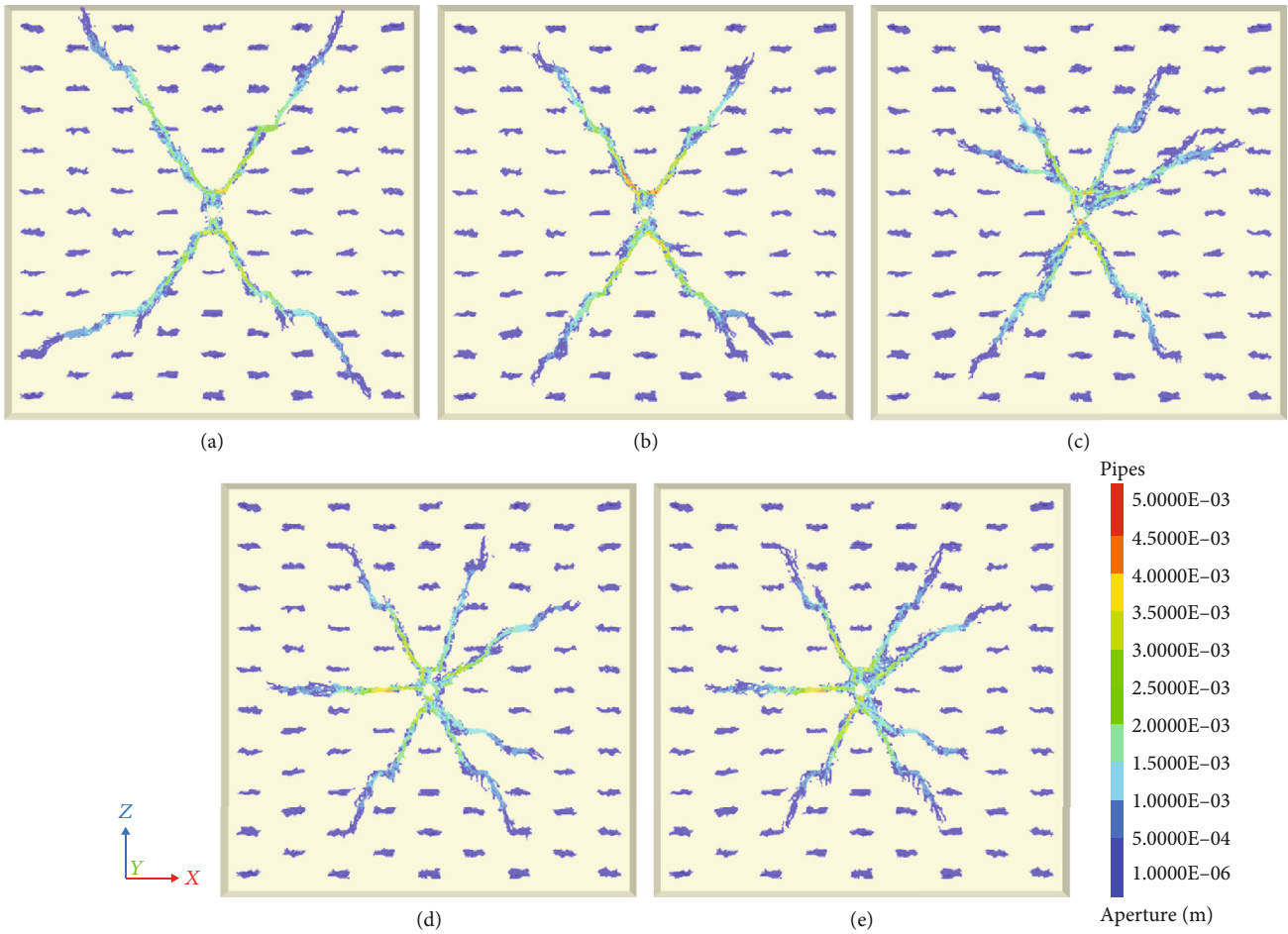


FIGURE 14: HF propagation in the NFN with different fluid viscosities: (a) 1 mPa-s, (b) 2 mPa-s, (c) 3 mPa-s, (d) 4 mPa-s, and (e) 5 mPa-s.

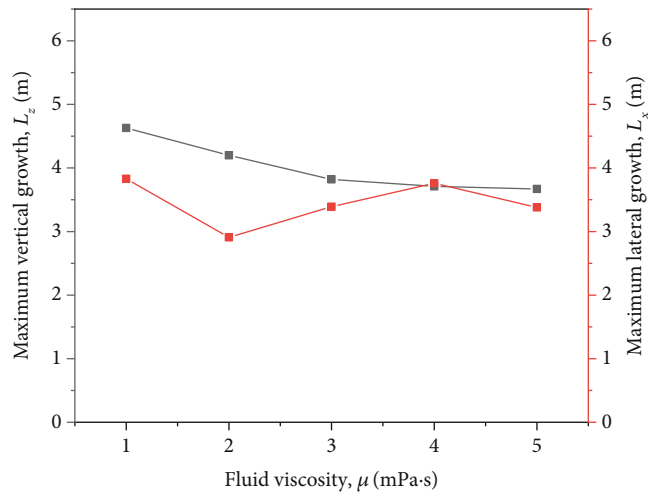


FIGURE 15: Variations of the maximum vertical and lateral growth for different fluid viscosities.



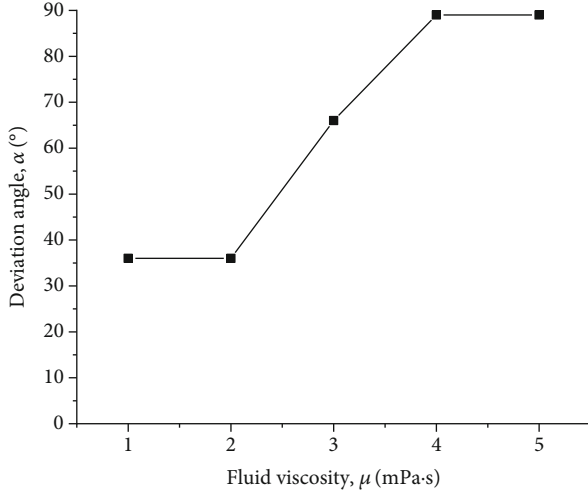


FIGURE 16: Variation of the maximum deviation angle for different fluid viscosities.

Figure 22(c). The fluid pressure varied slightly compared with type A. The induced shear slip on the horizontal NFs was similar between types A and B. Additionally, the vertical NFs connected by the HF appeared to be fully activated by shear failure. Most of the other vertical NFs also underwent a slight slip. In general, the HF propagation was similar between types A and B.

The HF propagation for type C differed significantly from the two aforementioned cases. As shown in Figure 23(b), the fluid was forced to pass through the connected NFN, and only a few new HFs were induced. The HF extended from the tip of the vertical NF, which was located on the edge of the NFN. The dominant flow path was still along the preferential fracture plane (the direction of maximum principal stress). As shown in Figure 23(c), the distribution pattern of the fracture fluid pressure was approximately radial. However, the fluid pressure gradient was reduced in comparison with those for types A and B, owing to the high connectivity of the NFN. Specifically, the size of the region with high fluid pressure ( $>20$  MPa) was smaller than those for types A and B. The fluid pressure on the edge of the network exceeded approximately 8 MPa. The number of vertical NFs that experienced shear slip was significantly larger than that for type B (Figure 23(d)). A large shear zone along the vertical direction was simulated, in which the vertical NFs appeared to be fully activated by shear slippage.

## 4. Discussion

**4.1. Analysis of Geometry of HFN.** The objective of this study was to examine the effects of various parameters on the HFN geometry and the complexity of the stimulation mechanism in naturally fractured formations. It has been well documented that the HF propagation pathway is dominated by in situ stress. According to the fracture mechanism and HF theory, it was argued that a larger stress difference leads to a shorter distance between the reoriented HF and the location of the maximum principal stress [38]. Liu et al. [39] concluded that the HF always propagates along the path of least

resistance, regardless of the direction of HF initiation. Additionally, an NF is opened or dilated when the HF propagates to the intersection point, resulting in a complex HFN with an elliptical stimulated region. Figure 24 shows a schematic of several types of behavior that have been observed in minebacks or laboratory tests. Despite the tortuosity of propagation pathway, HF always propagates along the path of least resistance [40]. Those interaction behaviors (e.g., crossing, diversion, and arrest) have been well reproduced in XSite simulations.

As shown in Figure 25, at the local scale, fluid tends to follow the NF rather than induce a new HF in the intact rock, as it must minimize the local work. However, on a large scale, the global orientation of the HF tends to remain parallel to  $\sigma_1$  owing to the global work minimization requirements [41].

As shown in Figure 26, in a large size triaxial experiment, Chen et al. [42] found that the fracture network evolution pattern is dependent on the horizontal principal stress difference. Under small stress difference, a radial fracture network would be induced. In contrast, under large stress difference, a dominant fracture with some small multibranch fractures would occur.

In our models, multiple radial HFs can be initiated at the wellbore, and an HFN with complex geometry can be induced owing to the HF–NF interactions (e.g., crossing, diversion, and arrest). In general, the global orientation of HF propagation tended to remain parallel to the direction of maximum principal stress. As shown in Figure 27, the HFN under a small stress difference was characterized by multiple radial branches, which are evenly distributed. With the increasing stress difference, the number of HF branches decreases, and the global orientation of the HF propagation is restricted to the direction of  $\sigma_1$ . However, with an increase in the fluid viscosity or injection rate, the evolution of the HFN geometry exhibits the opposite trend.

Treatment with a sufficiently high-viscosity fluid prevents the fluid from leaking into the surrounding rock, which results in a significant stress concentration. As the injection rate increases, the leakage into the surrounding rock becomes less important [43]. Moreover, poroelastic stress changes can locally modify the given tectonic stress regime [44, 45]. Consequently, with a high-viscosity fluid/high injection rate, multiple radial HFs can be initiated from the wellbore, and the HF pathway becomes relatively independent of the far-field stress field. Variations in the NFN, e.g., in the NF dip angle or the connectivity, can significantly alter the geometry of the corresponding HFN. The HF–NF interaction behaviors, such as crossing, diversion, and arrest, lead to high complexity in the analysis of the HFN.

The in situ stress dominates the HF propagation pathway on a large scale, whereas the treatment parameters (fluid viscosity/injection rate) and the NFs can alter the HF path on a local scale. The in situ stress, treatment parameters, and the NFs may act together to describe the propagation of HFN. The dominant stimulation mechanism in the NFN is determined by the contributions of different factors, which can vary significantly.

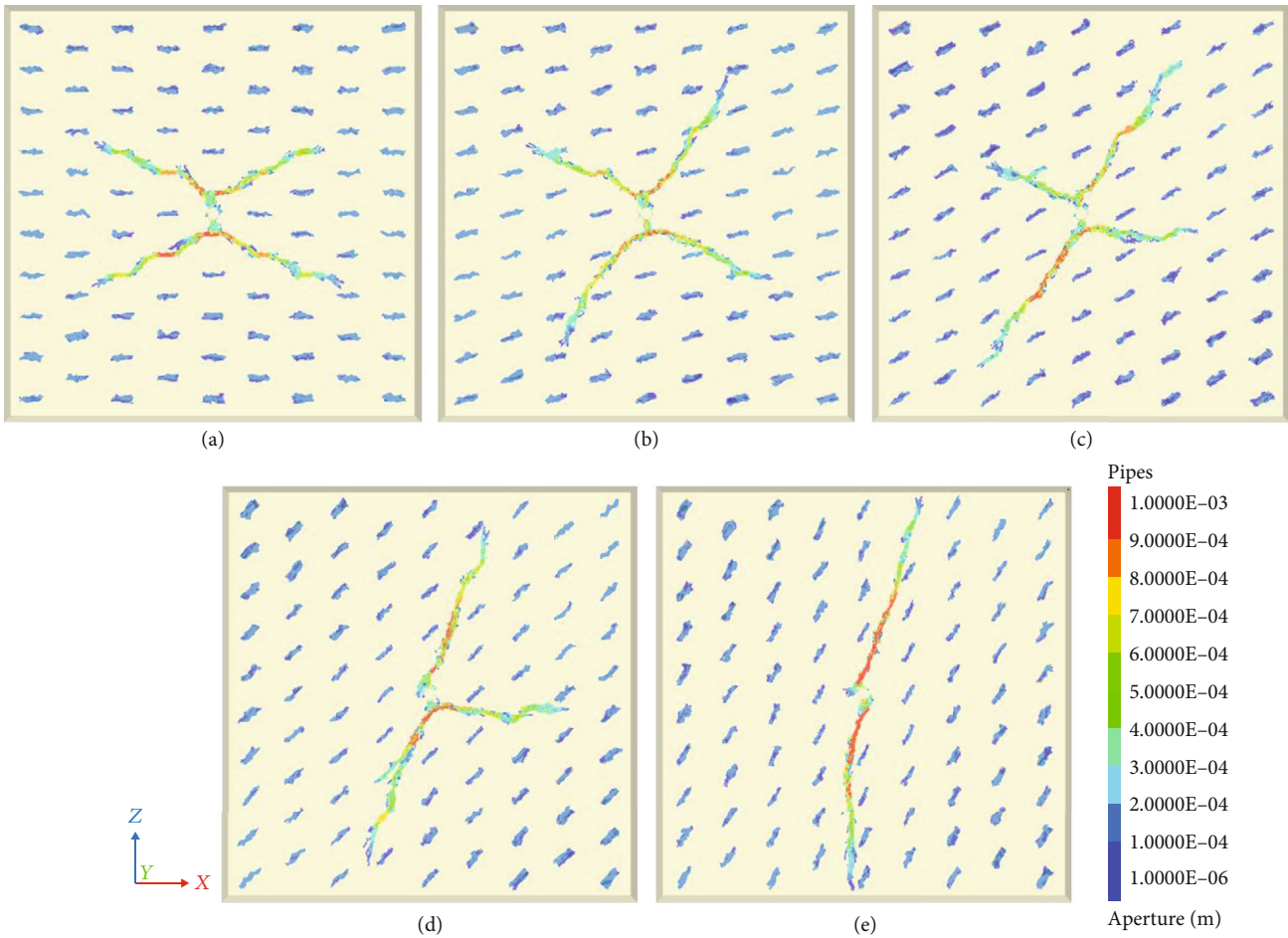


FIGURE 17: HF propagation in the NFN with different NF dip angles: (a)  $0^\circ$ , (b)  $15^\circ$ , (c)  $30^\circ$ , (d)  $45^\circ$ , and (e)  $60^\circ$ .

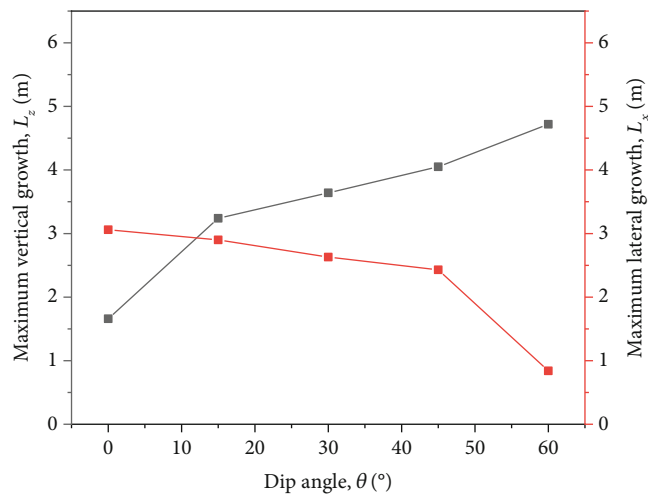


FIGURE 18: Variation of the maximum deviation angle for different NF dip angles.

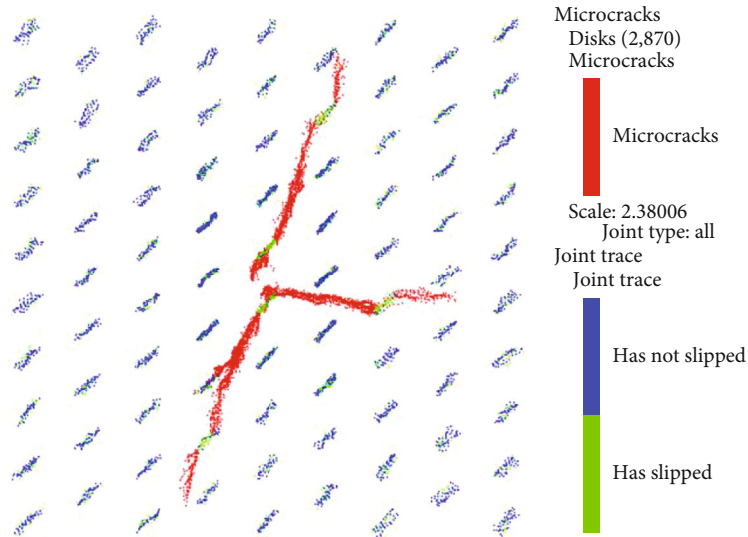


FIGURE 19: Microcracks in intact rock and shear slip on NFs for  $\theta = 45^\circ$ .

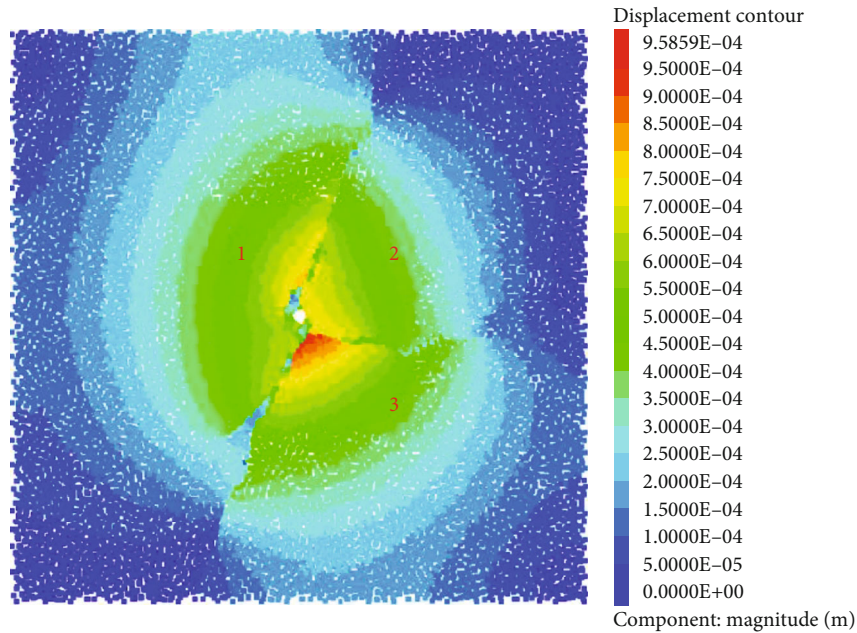


FIGURE 20: Discontinuous displacement field for  $\theta = 45^\circ$ .

4.2. *Analysis of Stimulation Mechanism in NFN.* As shown in Figure 28, McClure and Horne [46] presented four conceptual models for stimulation mechanisms: pure-opening model (POM), pure-shear stimulation (PSS), primary fracturing with shear stimulation leak off (PFSSL), and mixed-mechanism stimulation (MMS). The POM model assumes that no shear slippage occurs on the NF. The PSS model assumes that stimulation occurs through shear slippage on the NF and is hardly affected by the propagation of the new HF. The PFSSL model assumes that the continuous HF grows away from the wellbore, and fluid leaks into the connected NFs, resulting in shear slippage. The MMS model assumes that the HF can be terminated against the NF. This inhibits

the development of the continuous HF, forcing the fluid to pass through a network consisting of the new HF and NF.

POM and PSS are extreme cases that are unlikely to occur for naturally fractured formations. PFSSL and MMS are more probable for field treatment. The variations in the ratio of the tensile fracture (new HF) to the shear fracture (shear slip on NF) can be significant. They depend on the stress state, treatment parameters, and NFN, which determine the dominant stimulation mechanism. For instance, under a small stress difference, multiple radial HFs grow from the wellbore, connecting more NFs and forming a larger stimulated region compared with the large-stress difference case (see Figure 8). Additionally, the NF is more likely to experience

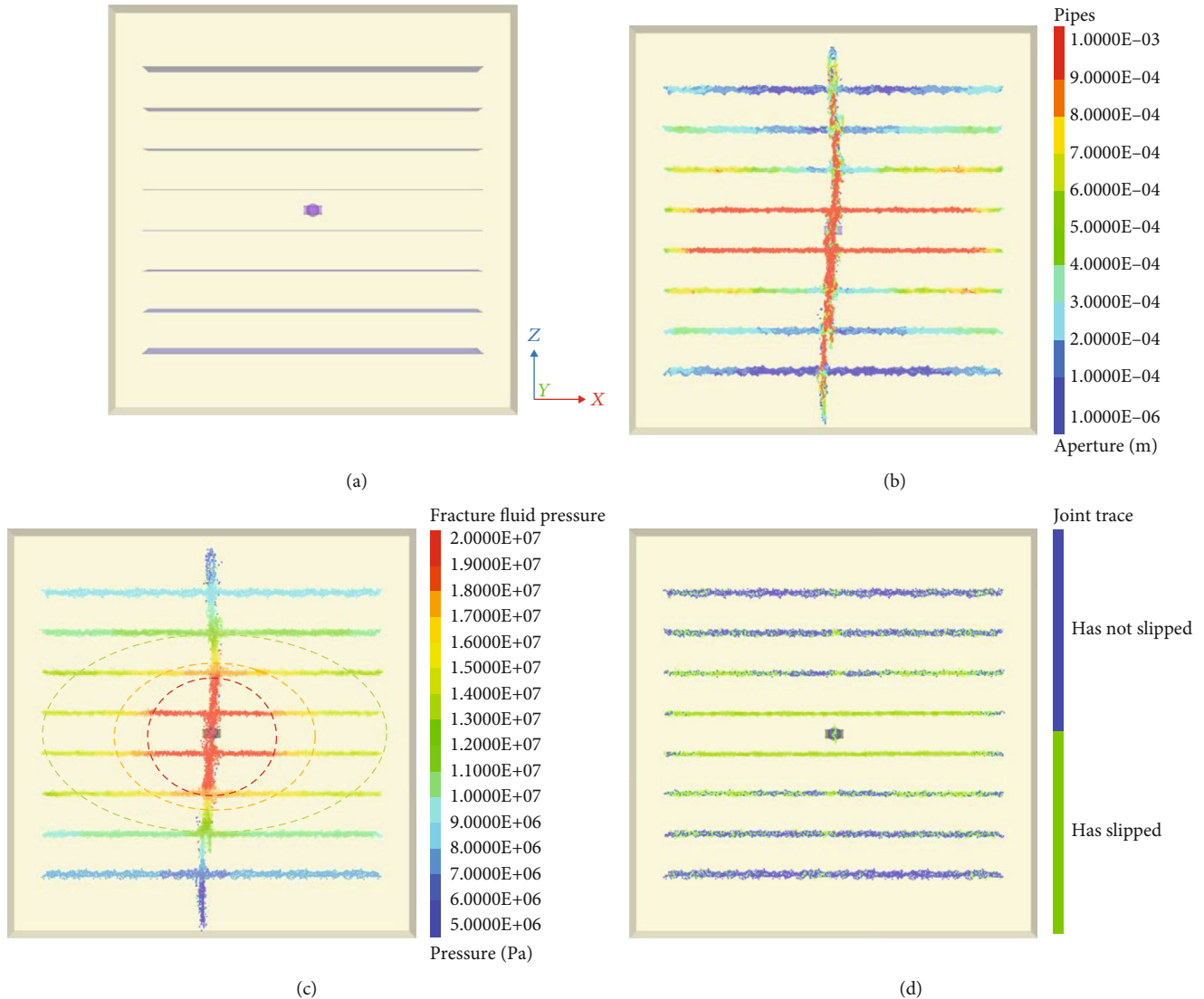


FIGURE 21: Type A NFN: (a) model setup, (b) fracture aperture, (c) fracture fluid pressure, and (d) shear slip on the NFN.

shear slip under smaller stress difference. Therefore, the shear slippage may play a significant role in the stimulation mechanism under a small stress difference. Conversely, the new induced HF may play a major role under a large stress difference. With a larger stress difference, the stimulated region is smaller, and the HF propagation is restricted to the direction of  $\sigma_1$ . Thus, fewer NFNs can be reached by the HF, and the NFNs are more stable. The dominant stimulation mechanism can be altered (at least to some extent) by changing the treatment parameters (injection rate and fluid viscosity) to modify the HFN geometry (see Figures 11 and 14). The type of NFN also affects the simulation mechanism. For a rock mass that contains well-connected NFNs, the fluid tends to follow the NFN, and only a few new HFNs are induced. In this case, shear slippage plays a dominant role in the stimulation of the NFN (see Figure 23). In contrast, for rocks containing isolated NFNs, the formation of the continuous HF is more dominant.

Quantitative evaluation of the stimulated region remains difficult. As shown in Figure 29, Chen et al. [41] reported a discrepancy between the stimulated (dilated) zone and the sand zone. The shear dilation effect can radiate outward by 200–300 m in some cases, resulting in a stimulated zone around the sand zone that has a larger volume than the sand zone.

Neither the analysis of McClure and Horne nor that of Dusseault considered the isolated NFN, which may experience shear slip. In the present study, there was a dilated zone involving unconnected NFNs, which experienced shear slip. As shown in Figure 19, many unconnected NFNs also underwent shear slip. The slip on unconnected NFNs may be attributed to poroelastic stress changes in the rock mass, which is supported by microseismicity interpretation [47] and theoretical analysis [48]. Even though activation of unconnected NFNs cannot enhance the conductivity of the HFN, the stress acting on the NFN plane and the elastic strain energy can be

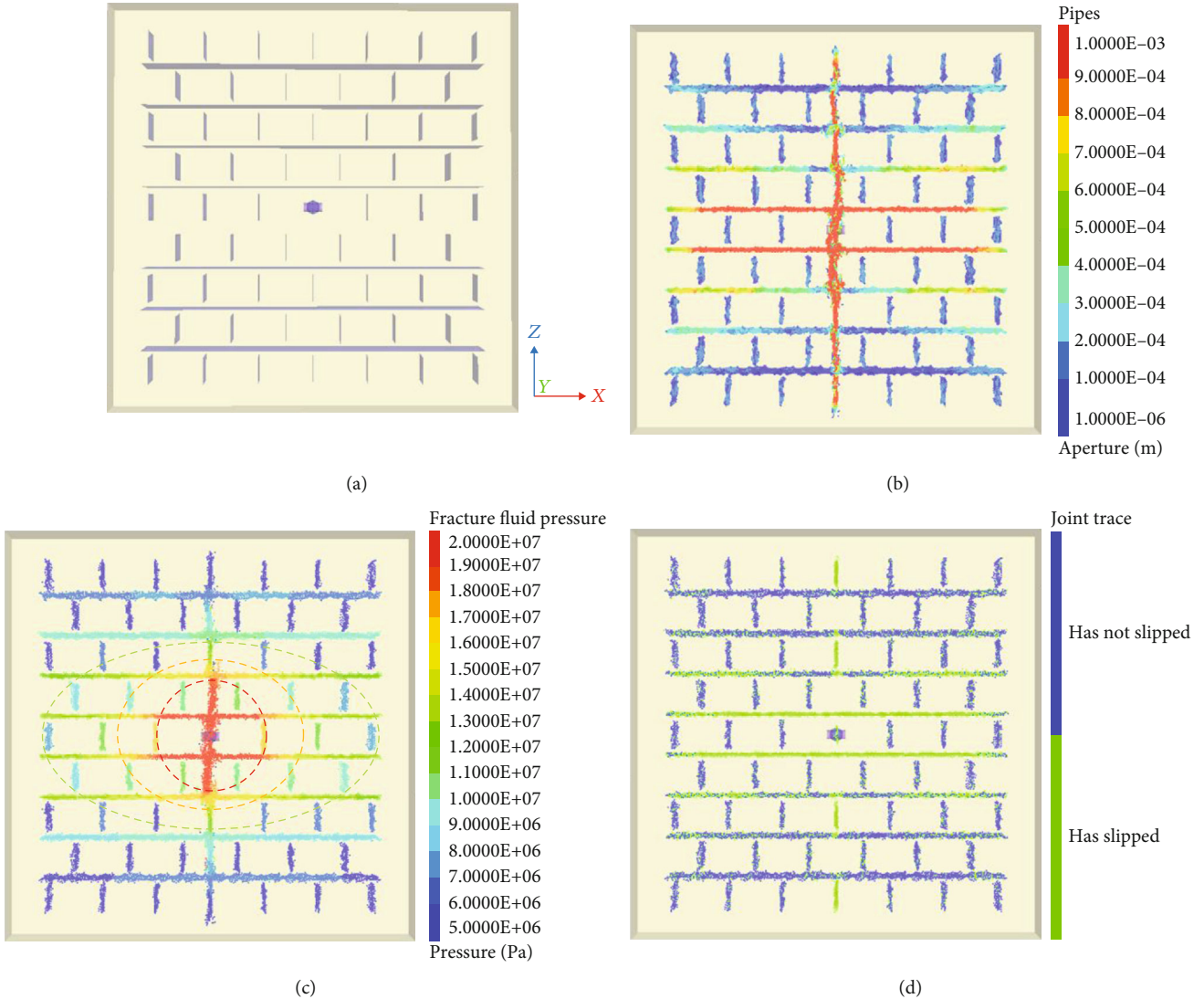


FIGURE 22: Type B NFN: (a) model setup, (b) fracture aperture, (c) fracture fluid pressure, and (d) shear slip on the NF.

reduced, which may be beneficial for mitigating rockburst or destressing underground excavations [49]. As shown in Figure 20, the variation in the displacement in a large area around the HF was observed. The displacement field can reflect the redistribution of stress. The stimulated region may contain the unconnected NFs experienced shear slip, modified displacement field, and redistribution of stress; it is not limited to the connected HFN. The stimulated region is larger than typically acknowledged, and a highly complex stimulation mechanism can be expected in naturally fractured formations.

**4.3. Modelling Considerations and Future Work.** The assumed NFN geometry might not precisely represent the actual complex NFN, which may consist of irregularly oriented NFs with different mechanical properties. The assumed NFN is a reasonable simplification because it properly accounts for the interaction behaviors between the HF and multiple NFs and can thus be used to predict an HFN with a simplified geometry. A discrete fracture network (DFN),

which is based on geological mapping, stochastic generation, and geomechanical simulation, is recommended for a more realistic representation of the NFN [50, 51]. A DFN can explicitly represent the geometric properties of individual NFs (e.g., the size, position, orientation, shape, and aperture), as well as the topological relationships between individual NFs and NF set [52]. Numerical simulations have contributed significantly to our understanding of HF propagation in fractured formation. However, numerical methods, such as the XFEM, BEM, and DEM, have their own merits and limitations [22–24]. Hydraulic fracturing is a nonlinear and multiscale process that involves mechanical deformation, fluid flow, fracture propagation, and their interaction. Additionally, the mechanical uncertainty and spatial variability of naturally fractured formations present considerable challenges for sensitivity and risk analyses [53, 54]. In addition to numerical simulations, support from methodologies, analysis, and experiments are required for a clearer understanding of the formation of HFN in naturally fractured formations.

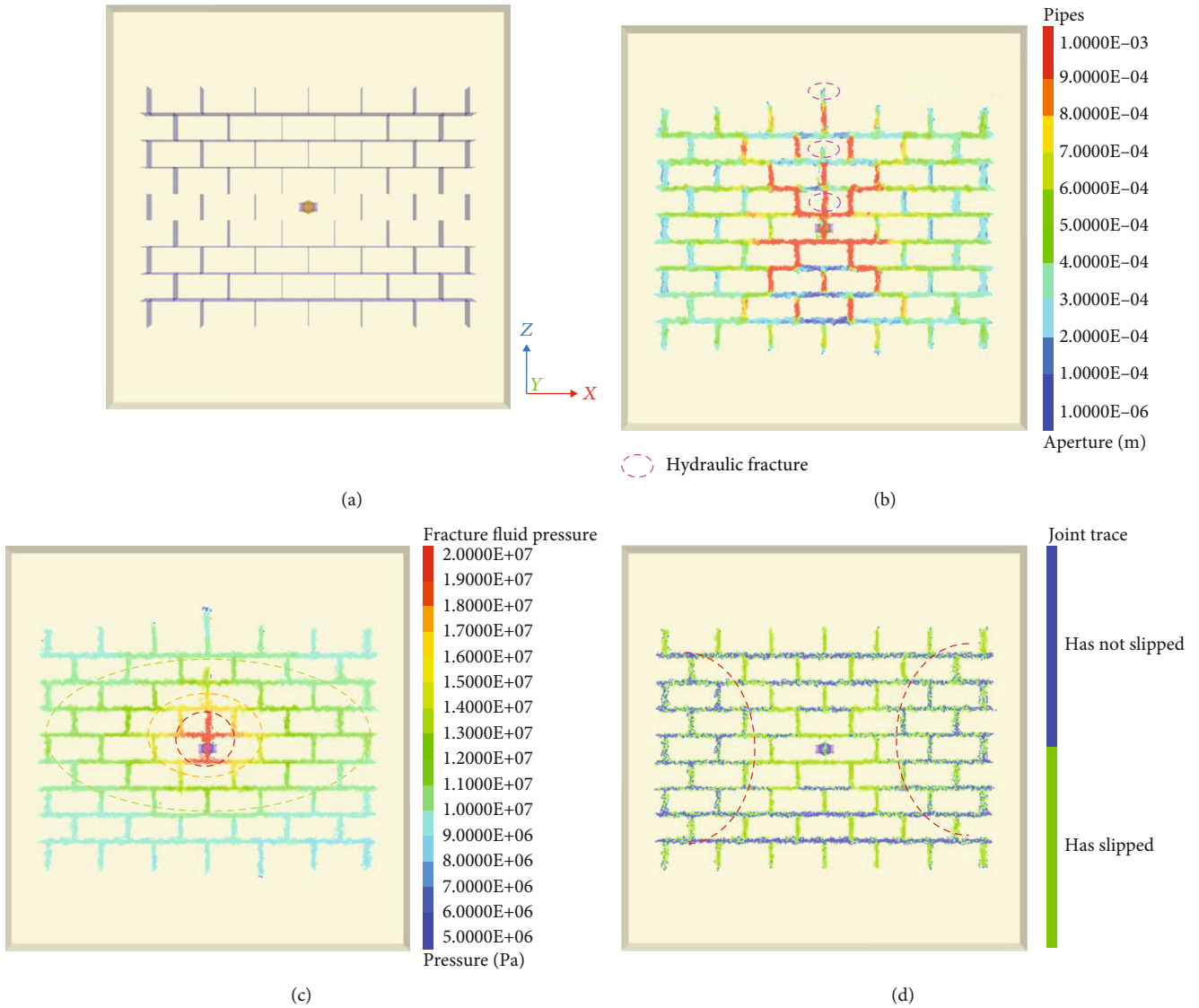


FIGURE 23: Type C NFN: (a) model setup, (b) fracture aperture, (c) fracture fluid pressure, and (d) shear slip on the NF.

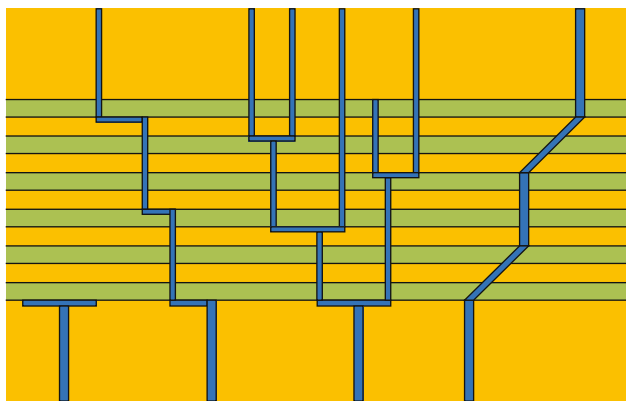


FIGURE 24: Schematic of types of observed fracture behavior crossing interfaces [40].

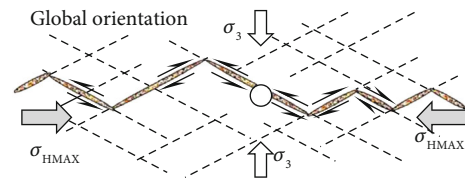


FIGURE 25: Schematic of the global orientation of fracture propagation in naturally fractured formation [41].

### 5. Conclusions

The lattice-spring code XSite was employed to determine the effects of various parameters on the geometry of the HFN. Sensitivity analyses were performed to investigate several controlling factors, such as the stress difference, injection rate, fluid viscosity, and NF orientation. The HF propagation in three types of HFNs was analyzed. According to the results, the following conclusions are drawn:

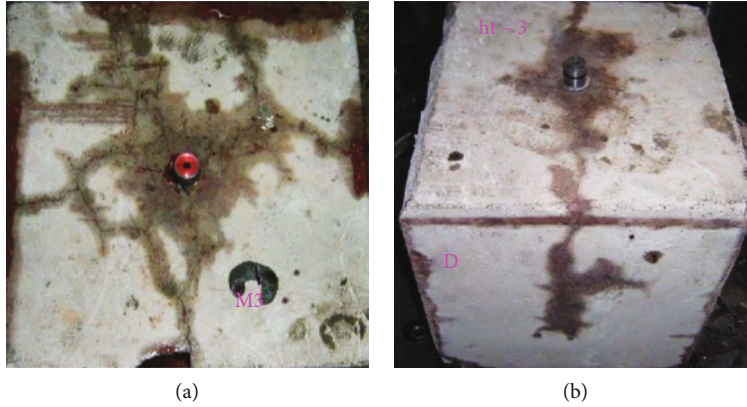


FIGURE 26: Experimental results of HF propagation pattern under different horizontal stress difference: (a) 5 MPa and (b) 10 MPa [42].

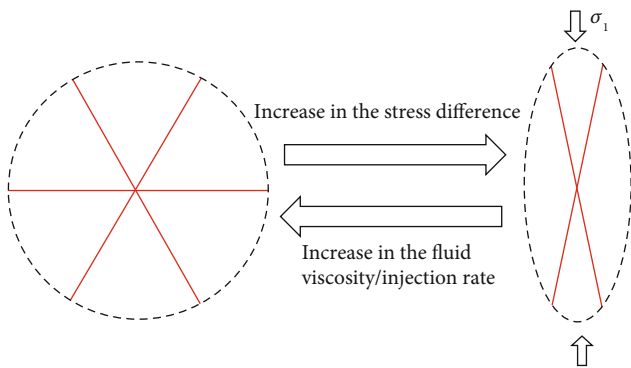


FIGURE 27: Evolution of the HFN geometry.

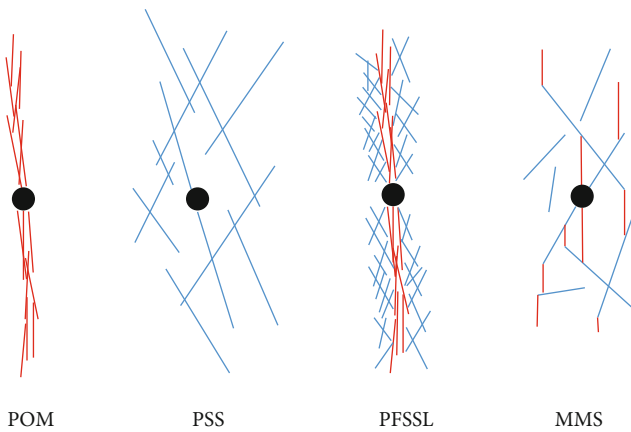


FIGURE 28: Four proposed stimulation mechanisms. The new HF and the NFs are indicated by red and blue lines, respectively. The mechanisms are POM, PSS, PFSSL, and MMS [44].

- (1) HF propagation tended to remain parallel to the direction of maximum principal stress. The in situ stress significantly affects the global orientation of the fracture propagation on a large scale. In contrast, NFs can alter the fracture pathway on a local scale owing to HF crossing, diversion, or arrest
- (2) With a large stress difference, the global orientation of fracture propagation is restricted to the direction

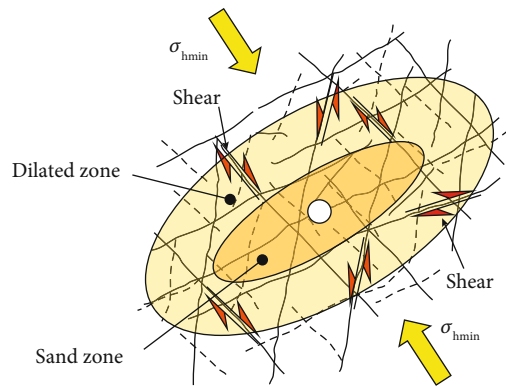


FIGURE 29: Schematic of the stimulated (dilated) zone around the sand-propped zone [41].

of maximum principal stress, changing the geometry of the HFN from circular to elliptical. With an increase in the fluid viscosity or injection rate, the evolution of the HFN geometry exhibits the opposite trend

- (3) The growth of multiple branches and the complexity of the HFN are reduced under a large stress difference. Conversely, a high injection rate and fluid viscosity contribute to the growth of multiple branches from the borehole and the complexity of the HFN. With a reduction in the angle between the NF and the maximum principal stress, the fracture branches and the complexity of the HFN are reduced
- (4) An NFN with higher connectivity tends to induce a larger shear zone and smaller fluid pressure gradient. The variations in the ratio of the tensile fracture (HF) to the shear fracture (shear slip on NF) can be significant. They depend on the stress state, treatment parameters, and NFN, which determine the dominant stimulation mechanism

**Data Availability**

All relevant data used to support the findings of this study are included within the article.

## Conflicts of Interest

The authors declare that there are no conflicts of interest regarding the publication of this paper.

## Acknowledgments

The first author wishes to thank China Scholarship Council for their support for visiting Simon Fraser University and Itasca Consulting Group, Inc. for providing XSite used for the modelling. This research was funded by the National Natural Science Foundation of China (grant number 51704160) and Tiandi Science and Technology Co., Ltd. Science and Technology Innovation Venture Capital Special Project (grant number 2019-TD-ZD008 and KJ-2018-TDKCZL-05).

## References


- [1] Z. Chong, Q. Yao, and X. Li, "Effect of joint geometrical parameters on hydraulic fracture network propagation in naturally jointed shale reservoirs," *Geofluids*, vol. 2018, 23 pages, 2018.
- [2] C. Ma, Y. Jiang, H. Xing, and T. Li, "Numerical modelling of fracturing effect stimulated by pulsating hydraulic fracturing in coal seam gas reservoir," *Journal of Natural Gas Science and Engineering*, vol. 46, pp. 651–663, 2017.
- [3] Q. He, F. T. Suorinen, and J. Oh, "Review of hydraulic fracturing for preconditioning in cave mining," *Rock Mechanics and Rock Engineering*, vol. 49, no. 12, pp. 4893–4910, 2016.
- [4] K. Fisher and N. Warpinski, "Hydraulic-fracture-height growth: real data," *SPE Production & Operations*, vol. 27, no. 1, pp. 8–19, 2013.
- [5] Z. Zhang, X. Li, W. Yuan, J. He, G. Li, and Y. Wu, "Numerical analysis on the optimization of hydraulic fracture networks," *Energies*, vol. 8, no. 10, pp. 12061–12079, 2015.
- [6] J. Zhou, Y. Jin, and M. Chen, "Experimental investigation of hydraulic fracturing in random naturally fractured blocks," *International Journal of Rock Mechanics and Mining Sciences*, vol. 47, no. 7, pp. 1193–1199, 2010.
- [7] J. Zhou, M. Chen, Y. Jin, and G.-q. Zhang, "Analysis of fracture propagation behavior and fracture geometry using a tri-axial fracturing system in naturally fractured reservoirs," *International Journal of Rock Mechanics and Mining Sciences*, vol. 45, no. 7, pp. 1143–1152, 2008.
- [8] L. J. L. Beugelsdijk, C. J. De Pater, and K. Sato, "Experimental hydraulic fracture propagation in a multi-fractured medium," *SPE Asia Pacific Conference on Integrated Modelling for Asset Management*, pp. 177–184, 2000.
- [9] Z. Yushi, Z. Shicheng, Z. Tong, Z. Xiang, and G. Tiankui, "Experimental investigation into hydraulic fracture network propagation in gas shales using CT scanning technology," *Rock Mechanics and Rock Engineering*, vol. 49, no. 1, pp. 33–45, 2016.
- [10] M. K. Fisher, C. A. Wright, B. M. Davidson et al., "Integrating fracture mapping technologies to improve stimulations in the Barnett shale," *SPE Production & Facilities*, vol. 20, no. 2, pp. 85–93, 2013.
- [11] M. J. Mayerhofer, E. P. Lonon, N. R. Warpinski, C. L. Cipolla, D. W. Walser, and C. M. Rightmire, "What is stimulated reservoir volume?," *SPE Production & Operations*, vol. 25, no. 1, pp. 89–98, 2013.
- [12] F. Cruz, D. Roehl, and E. d. A. Vargas Jr., "An XFEM element to model intersections between hydraulic and natural fractures in porous rocks," *International Journal of Rock Mechanics and Mining Sciences*, vol. 112, pp. 385–397, 2018.
- [13] B. Lecampion, "An extended finite element method for hydraulic fracture problems," *Communications in Numerical Methods in Engineering*, vol. 25, no. 2, pp. 121–133, 2009.
- [14] H. Y. Wang, "Numerical modeling of non-planar hydraulic fracture propagation in brittle and ductile rocks using XFEM with cohesive zone method," *Journal of Petroleum Science and Engineering*, vol. 135, pp. 127–140, 2015.
- [15] J. Guo, B. Luo, C. Lu, J. Lai, and J. Ren, "Numerical investigation of hydraulic fracture propagation in a layered reservoir using the cohesive zone method," *Engineering Fracture Mechanics*, vol. 186, pp. 195–207, 2017.
- [16] X. Zhang, R. G. Jeffrey, and M. Thiercelin, "Deflection and propagation of fluid-driven fractures at frictional bedding interfaces: a numerical investigation," *Journal of Structural Geology*, vol. 29, no. 3, pp. 396–410, 2007.
- [17] J. Tang, K. Wu, B. Zeng et al., "Investigate effects of weak bedding interfaces on fracture geometry in unconventional reservoirs," *Journal of Petroleum Science and Engineering*, vol. 165, pp. 992–1009, 2018.
- [18] O. Kresse and X. Weng, "Numerical modeling of 3D hydraulic fractures interaction in complex naturally fractured formations," *Rock Mechanics and Rock Engineering*, vol. 51, no. 12, pp. 3863–3881, 2018.
- [19] F. Zhang and M. Mack, "Integrating fully coupled geomechanical modeling with microseismicity for the analysis of refracturing treatment," *Journal of Natural Gas Science and Engineering*, vol. 46, pp. 16–25, 2017.
- [20] F. Zhang, E. Dontsov, and M. Mack, "Fully coupled simulation of a hydraulic fracture interacting with natural fractures with a hybrid discrete-continuum method," *International Journal for Numerical and Analytical Methods in Geomechanics*, vol. 41, no. 13, pp. 1430–1452, 2017.
- [21] B. Damjanac and P. Cundall, "Application of distinct element methods to simulation of hydraulic fracturing in naturally fractured reservoirs," *Computers and Geotechnics*, vol. 71, pp. 283–294, 2016.
- [22] X. Weng, "Modeling of complex hydraulic fractures in naturally fractured formation," *Journal of Unconventional Oil and Gas Resources*, vol. 9, pp. 114–135, 2015.
- [23] A. Dahi Taleghani, M. Gonzalez, and A. Shojaei, "Overview of numerical models for interactions between hydraulic fractures and natural fractures: challenges and limitations," *Computers and Geotechnics*, vol. 71, pp. 361–368, 2016.
- [24] B. Lecampion, A. Bungler, and X. Zhang, "Numerical methods for hydraulic fracture propagation: a review of recent trends," *Journal of Natural Gas Science and Engineering*, vol. 49, pp. 66–83, 2018.
- [25] A. D. Taleghani and J. E. Olson, "Analysis of multistranded hydraulic fracture propagation: an improved model for the interaction between induced and natural fractures," *Society of Petroleum Engineers (SPE)*, 2009.
- [26] S. Abbas, E. Gordeliy, A. Peirce, B. Lecampion, D. Chuprakov, and R. Prioul, "Limited height growth and reduced opening of hydraulic fractures due to fracture offsets: an XFEM application," *SPE Hydraulic Fracturing Technology Conference*, pp. 587–599, 2014.
- [27] A. Ghaderi, J. Taheri-Shakib, and M. A. Sharif Nik, "The distinct element method (DEM) and the extended finite element method (XFEM) application for analysis of interaction



- between hydraulic and natural fractures,” *Journal of Petroleum Science and Engineering*, vol. 171, pp. 422–430, 2018.
- [28] J. E. Olson, “Multi-fracture propagation modeling: Applications to hydraulic fracturing in shales and tight gas sands,” in *The 42nd US rock mechanics symposium (USRMS)*. American Rock Mechanics Association, San Francisco, California, June–July 2008.
- [29] D. Elmo and D. Stead, “An integrated numerical modelling-discrete fracture network approach applied to the characterisation of rock mass strength of naturally fractured pillars,” *Rock Mechanics and Rock Engineering*, vol. 43, no. 1, pp. 3–19, 2010.
- [30] F. Gao, D. Stead, and D. Elmo, “Numerical simulation of microstructure of brittle rock using a grain-breakable distinct element grain-based model,” *Computers and Geotechnics*, vol. 78, pp. 203–217, 2016.
- [31] D. Mas Ivars, N. Deisman, M. E. Pierce, and C. Fairhurst, “The synthetic rock mass approach—a step forward in the characterization of jointed rock masses,” in *11th ISRM Congress. International Society for Rock Mechanics and Rock Engineering*, pp. 485–490, Lisbon, Portugal, July 2007.
- [32] B. Damjanac, C. Detournay, and P. A. Cundall, “Application of particle and lattice codes to simulation of hydraulic fracturing,” *Computational Particle Mechanics*, vol. 3, no. 2, pp. 249–261, 2016.
- [33] E. Bakhshi, V. Rasouli, A. Ghorbani, M. Fatehi Marji, B. Damjanac, and X. Wan, “Lattice numerical simulations of lab-scale hydraulic fracture and natural interface interaction,” *Rock Mechanics and Rock Engineering*, vol. 52, no. 5, pp. 1315–1337, 2019.
- [34] K. Zhao, D. Stead, H. Kang, B. Damjanac, D. Donati, and F. Gao, “Investigating the interaction of hydraulic fracture with pre-existing joints based on lattice spring modeling,” *Computers and Geotechnics*, vol. 122, p. 103534, 2020.
- [35] X. Liu, Z. Qu, T. Guo, Y. Sun, Z. Wang, and E. Bakhshi, “Numerical simulation of non-planar fracture propagation in multi-cluster fracturing with natural fractures based on lattice methods,” *Engineering Fracture Mechanics*, vol. 220, p. 106625, 2019.
- [36] X. Wan, V. Rasouli, B. Damjanac, and H. Pu, “Lattice simulation of hydraulic fracture containment in the North Perth Basin,” *Journal of Petroleum Science and Engineering*, vol. 188, p. 106904, 2020.
- [37] P. A. Cundall, “Lattice method for modeling brittle, jointed rock,” in *Proceedings of the 2nd Int’l FLAC/DEM Symposium on Continuum and Distinct Element Numerical Modeling in Geomechanics*, Melbourne, Australia, 2011.
- [38] G. Q. Zhang and M. Chen, “Dynamic fracture propagation in hydraulic re-fracturing,” *Journal of Petroleum Science and Engineering*, vol. 70, no. 3–4, pp. 266–272, 2010.
- [39] Z. Liu, M. Chen, and G. Zhang, “Analysis of the influence of a natural fracture network on hydraulic fracture propagation in carbonate formations,” *Rock Mechanics and Rock Engineering*, vol. 47, no. 2, pp. 575–587, 2014.
- [40] N. R. Warpinski, “Fracture growth in layered and discontinuous media,” 2011, <https://www.epa.gov/sites/production/files/documents/fracturegrowthinlayeredanddiscontinuousmedia.pdf>.
- [41] M. Chen, J. Zhou, Y. Jin, and G. Zhang, “Experimental study on fracturing features in naturally fractured reservoir,” *Acta Petrolei Sinica*, vol. 29, no. 3, pp. 431–434, 2008.
- [42] M. B. Dusseault, “Geomechanical aspects of shale gas development,” *Rock mechanics for resources, energy and environment*, vol. 39, 2013.
- [43] T. Katsaga, A. Riahi, D. O. DeGagne, B. Valley, and B. Damjanac, “Hydraulic fracturing operations in mining: conceptual approach and DFN modeling example,” *Mining Technology*, vol. 124, no. 4, pp. 255–266, 2015.
- [44] J. B. Altmann, B. I. R. Müller, T. M. Müller, O. Heidbach, M. R. P. Tingay, and A. Weißhardt, “Pore pressure stress coupling in 3D and consequences for reservoir stress states and fault reactivation,” *Geothermics*, vol. 52, pp. 195–205, 2014.
- [45] K. Atefi Monfared and L. Rothenburg, “Poroelastic stress modifications surrounding a fully-penetrating injection well,” *Journal of Petroleum Science and Engineering*, vol. 135, pp. 660–670, 2015.
- [46] M. W. McClure and R. N. Horne, “An investigation of stimulation mechanisms in enhanced geothermal systems,” *International Journal of Rock Mechanics and Mining Sciences*, vol. 72, pp. 242–260, 2014.
- [47] S. C. Maxwell and A. Pirayehgar, “Geomechanical simulation of different conceptual models for microseismic interpretation,” in *Proceedings of the 6th Unconventional Resources Technology Conference*, Houston, Texas, July 2018.
- [48] H. Gu and X. Weng, “Criterion for fractures crossing frictional interfaces at non-orthogonal angles,” in *44th US rock mechanics symposium and 5th US-Canada rock mechanics symposium*, pp. 1–6, Salt Lake City, Utah, June 2010.
- [49] H. Kang, H. Lv, F. Gao, X. Meng, and Y. Feng, “Understanding mechanisms of destressing mining-induced stresses using hydraulic fracturing,” *International Journal of Coal Geology*, vol. 196, pp. 19–28, 2018.
- [50] D. Elmo, S. Rogers, D. Stead, and E. Eberhardt, “Discrete fracture network approach to characterise rock mass fragmentation and implications for geomechanical upscaling,” *Mining Technology*, vol. 123, no. 3, pp. 149–161, 2014.
- [51] S. Rogers, D. Elmo, R. Dunphy, and D. Bearinger, “Understanding hydraulic fracture geometry and interactions in the Horn River Basin through DFN and numerical modeling,” in *Canadian Unconventional Resources and International Petroleum Conference*, pp. 1426–1437, Calgary, Alberta, Canada, October 2010.
- [52] Q. Lei, J. P. Latham, and C. F. Tsang, “The use of discrete fracture networks for modelling coupled geomechanical and hydrological behaviour of fractured rocks,” *Computers and Geotechnics*, vol. 85, pp. 151–176, 2017.
- [53] E. Eberhardt, K. Woo, D. Stead, and D. Elmo, “Transition from surface to underground mining : integrated mapping , monitoring and modeling data to better understand complex rock mass interaction,” in *Proceedings of the international symposium on rock slope stability in open pit mining and civil engineering*, pp. 321–332, Perth, Australia, 2007.
- [54] W. Pettitt, M. Pierce, B. Damjanac et al., “Fracture network engineering for hydraulic fracturing,” *The Leading Edge*, vol. 30, no. 8, pp. 844–853, 2011.

## Research Article

# Effect of Gas Adsorption on the Application of the Pulse-Decay Technique

Shaicheng Shen,<sup>1,2</sup> Xiaochun Li,<sup>1</sup> Zhiming Fang<sup>1</sup> ,<sup>1</sup> and Nao Shen<sup>1,2</sup>

<sup>1</sup>State Key Laboratory of Geomechanics and Geotechnical Engineering, Institute of Rock and Soil Mechanics, Chinese Academy of Sciences, Wuhan, Hubei 430071, China

<sup>2</sup>University of Chinese Academy of Sciences, Beijing 100049, China

Correspondence should be addressed to Zhiming Fang; [zhmfang2002@163.com](mailto:zhmfang2002@163.com)

Received 22 August 2020; Revised 14 September 2020; Accepted 22 September 2020; Published 5 October 2020

Academic Editor: Mandadige S. A. Perera

Copyright © 2020 Shaicheng Shen et al. This is an open access article distributed under the Creative Commons Attribution License, which permits unrestricted use, distribution, and reproduction in any medium, provided the original work is properly cited.

The permeability of coal is an indispensable parameter for predicting the coalbed methane (CBM) and enhanced CBM (ECBM) production. Considering the low permeability characteristics of coal, the permeability is usually measured by the transient technique in the laboratory. Normally, it is assumed that the calculated permeability will not greatly vary if the pulse pressure applied in the experiment is small (less than 10% of pore pressure) and previous studies have not focused on the effect of the pulse pressure on the measurement permeability. However, for sorptive rock, such as coals and shales, the sorption effect may cause different measurement results under different pulse pressures. In this study, both nonadsorbing gas (helium) and adsorbing gas (carbon dioxide) were used to investigate the adsorption effect on the gas permeability of coal measurement with the pulse-decay technique. A series of experiments under different pore pressures and pulse pressures was performed, and the carbon dioxide permeability was calculated by both Cui et al.'s and Jones' methods. The results show that the carbon dioxide permeability calculated by Jones' method was underestimated because the adsorption effect was not considered. In addition, by comparing the helium and carbon dioxide permeabilities under different pulse pressures, we found that the carbon dioxide permeability of coal was more sensitive to the pulse pressure due to the adsorption effect. Thus, to obtain the accurate permeability of coal, the effect of adsorption should be considered when measuring the permeability of adsorptive media with adsorbing gas by the transient technique, and more effort is required to eliminate the effect of the pulse pressure on the measured permeability.

## 1. Introduction

To alleviate the problems of energy shortage and global warming, researchers pay more attention to the technologies of CBM, ECBM, and carbon dioxide storage in coal seams. The permeability of coal is one of the most important parameters for those projects. To predict the methane production of a coal seam and evaluate its storage potentiality, it is essential to accurately and quickly measure the coal permeability. At present, the steady flow method (SFM) and pulse-decay method (PDM) are the main methods to measure the permeability. However, for tight reservoir rocks, such as coal and shale, it is time-consuming to attain equilibrium in SFM and difficult to accurately measure the flow rate. Thus, com-

pared with SFM, PDM becomes popular due to its shorter experimental time and higher resolution [1, 2].

The PDM was used by Brace et al. [3] to measure the permeability of a granite sample, and the permeability was calculated by the decay curve of the differential pressure between upstream and downstream. However, this approximation method to assess the permeability did not consider the effect of compressive storage [4]. Hsieh et al. [5] presented a general analytical solution in the transient test considering the compressive storage of the sample. However, this solution was difficult to evaluate [6]. To more easily obtain the sample permeability, Dicker and Smits [6] constrained the volume of the storage reservoir and quickly obtained the single-exponential decay of the pressure decline curve. Jones [7]

improved the work of Dicker and Smits. In Jones' method, the permeability is calculated from "late-time" measurements which yield the overall effective permeability of a core plug in the same manner as steady-state measurements [7]. All of these methods assume that there is no interaction between the sample and the gas. However, for absorbing gases (such as methane and carbon dioxide), gas molecules will interact with the adsorbing media (such as coal and shale) [8–11], which make the matrix swell or shrink. Thus, it is necessary to discuss the effect of gas adsorption on the permeability measurement when using the pulse-decay method. Based on the previous work, Cui et al. [2] revised the pulse-decay technique to correct the impact of adsorption on the effective permeability measurement. In Cui et al.'s work, Langmuir isotherm was used to describe the gas adsorption in coal seams. However, Mahmoud et al. [12] noted that the heterogeneity of the rock surface was the main factor that affects the adsorption strength. The single-layer Langmuir isotherm adsorption model cannot accurately describe the adsorption of gas molecules on the rock surface, so the formula is revised based on the Freundlich isotherm adsorption model.

All studies assume that the fluid viscosity, fluid compressibility, porosity, and permeability are constant during the experiment if the initial differential pressure is small (within 10% of pore pressure). Thus, the gas permeability measured under different pulse pressures is relatively stable. Intuitively, it is feasible to measure the helium permeability of coal because the change in small initial differential pressure may have little effects on the differential pressure decay during the experiment. However, for adsorbing gases and media, such as carbon dioxide and coal, the changes in pore pressure may break the original ad-/desorption balance between gas and matrix and induce the difference in measured differential pressure decay curves under different pulse pressures during the experiment. The purpose of this article is to investigate the effect of the initial pulse pressure on the measurement results of the gas permeability of coal when the transient technique is used in the laboratory, especially for carbon dioxide.

## 2. Experimental Work

The PDM was used to measure the permeability of Sihe coal. Brace et al. [3] mentioned that the pulse pressure should be less than 10% of the upstream pressure because both viscosity and compressibility of fluids varied with pressure. Thus, the minimum upstream pressure is 1 MPa, and the maximum pulse pressure is 100 kPa during the experiment.

**2.1. Sample Preparation.** The sample in this study is from Sihe coal mine in Qinshui Basin. A cylindrical coal sample was prepared before the experiment. As shown in Figure 1, the length of the coal sample is 50.53 mm and its diameter is 24.99 mm. The sample surfaces were polished to enable the smooth contact between the coal and the shrinkable tube, which can prevent the shrinkable tube from rupturing and causing the confining fluid to flow into the sample. To remove residual moisture and adsorbed gases from the coal sample, the core was placed in a 60° vacuum environment

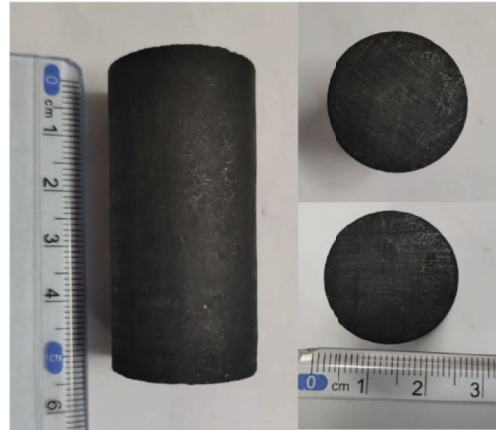


FIGURE 1: Photograph of the cylindrical core sample.

and dried for 48 hours before the experiment. The initial weight of the coal is 40.96 g, and the weight becomes 40.90 g after drying.

**2.2. Experimental Setup and Procedures.** The schematic diagram of the transient pulse-decay testing apparatus in our study is shown in Figure 2 [3, 13]. A core holder which is made of stainless steel was used to measure the gas permeability of coal under hydrostatic pressure conditions, and it can maintain a maximum confining pressure of 20 MPa. A confining pump was used to apply the confining pressure during the experiment. A thin lead foil was used to wrap the cylindrical core sample to prevent gas diffusion from the core to the confining fluid at high pressures [14], and a heat-shrinkable tube was employed to isolate the core from the confining fluid. An ISCO pump, which is with the full scale of 68.95 MPa and the accuracy of  $\pm 0.5\%$  FS at constant temperature, was applied to supply the initial pore pressure to the sample. A differential pressure transducer with the accuracy of  $\pm 0.25\%$  FS (FS = 220 kPa) was used to accurately record the pressure difference between upstream and downstream every second. The volumes of the upstream and downstream are 6.115 ml and 4.505 ml, respectively. During the experiment, the temperature was maintained at  $26 \pm 1^\circ\text{C}$ , and the net confining pressure is 3 MPa. The experimental conditions are shown in Table 1.

The test procedure is as follows: (1) Test the leakage rate of the measurement system. (2) Install the dried and wrapped coal sample into the core holder and apply a confining pressure according to the experimental condition. (3) Close valve 1, open other valves, and connect the coal sample with a vacuum pump to eliminate residual gases in the pipeline and coal sample for 1 hour. After vacuuming, close valve 4. (4) Open valve 1 and apply the initial pore pressure in the system through the ISCO pump at the constant-pressure mode. When the residual gas volume in the ISCO pump remains unchanged, close valves 2 and 3 and impose a pressure difference in the upstream through the ISCO pump. When the pressure difference between the upstream and downstream is equal to the designed value, close valve 1. (5) When the upstream pressure stabilizes, open valve 2 and collect the data of the differential pressure transducer. (6) According to the

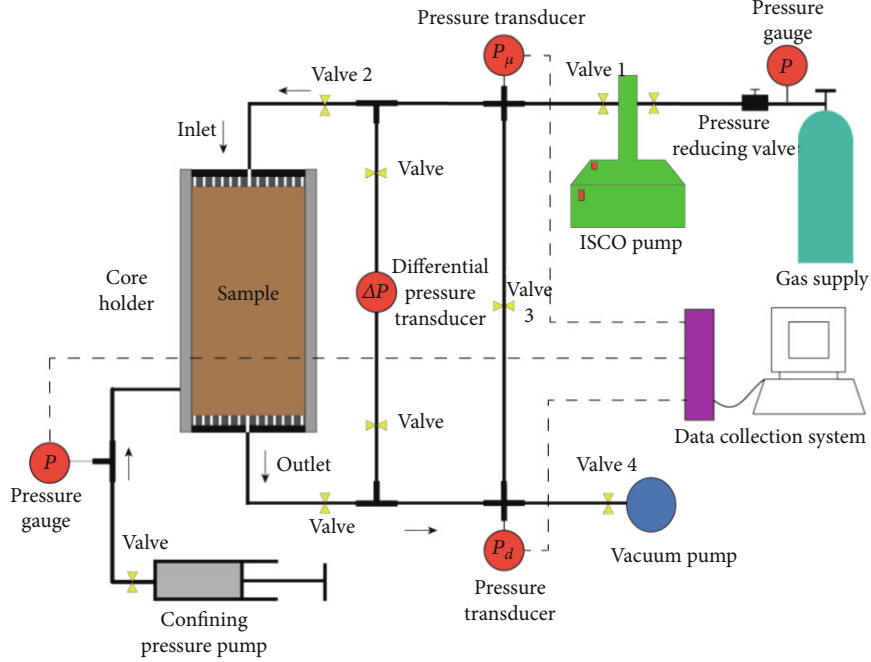


FIGURE 2: Sketch of the experimental setup for the permeability measurement.

TABLE 1: Experimental scheme for the permeability test.

Gas type	Confining pressure (MPa)	Pore pressure (MPa)	Pulse pressure (kPa)
	4	1	
Carbon dioxide,	5	2	40, 60, 80, 100
helium	6	3	
	7	4	

change in differential pressure with time, calculate the permeability using the solution. (7) Change the injected pore pressure and applied pulse pressure and measure the permeability under different conditions. When the test fluid is carbon dioxide, inject the gas into the sample for a week to achieve the balance between adsorption and desorption. When the pore pressure changes, the permeability was measured after 24 hours until equilibrium was achieved. The applied pressure difference is slightly larger than the designed pulse pressure due to the effect of the dead volume ( $V_{\text{dead}}$ ) which is the volume between valve 2 and the top face of the coal sample.

### 3. Calculation of Permeability

A tremendous amount of work has been performed to study the permeability calculation when using the PDM. Because the coal permeability is a gas type-dependent property, both carbon dioxide (adsorbing gas) and helium (non-adsorbing gas) are used in our experiment. To compare the difference in carbon dioxide permeability of coal obtained by different solutions (whether we consider the adsorption effect), both Jones' method and Cui et al.'s method were applied in this study.

3.1. *Jones' Method (1997)*. The pressure decay curve is described by the differential equation of the gas through the sample. With the given boundary conditions and initial conditions, Dicker and Smits [6] provided the relationship between dimensionless pressure difference  $\Delta P_D$  and dimensionless time  $t_D$  as follows:

$$\Delta P_D(a, b, t_D) = 2 \sum_{m=1}^{\infty} \exp(-t_D \theta_m^2) \cdot \frac{a(b^2 + \theta_m^2) - (-1)^m b \sqrt{(a^2 + \theta_m^2)(b^2 + \theta_m^2)}}{\theta_m^4 + \theta_m^2(a + a^2 + b + b^2) + ab(a + b + ab)}, \quad (1)$$

$$\tan \theta = \frac{(a + b)\theta}{\theta^2 - ab}, \quad (2)$$

where  $a$  and  $b$  are the ratios of the compressive storage of the sample's pore volume to that of the upstream and downstream reservoirs, respectively;  $\theta_m$  are the roots of Equation (2);  $t_D$  is the dimensionless time;  $t_D = kt/(c\mu\phi L^2)$ , where  $k$  is the permeability,  $t$  is the real time,  $c$  is the fluid compressibility,  $\mu$  is the fluid viscosity,  $\phi$  is the porosity, and  $L$  is the sample length.

Because Equation (1) is a form of infinite series, and Equation (2) is difficult to solve, Jones [7] defined  $f_1$  as follows:

$$f_1 \equiv \frac{\theta_1^2}{a + b}, \quad (3)$$

where  $\theta_1$  is the first root of Equation (2).

For rigid gas reservoirs, the compressibility of the reservoir is negligible compared to that of gas. If  $a$  and  $b$  are equal and  $t_D$  is sufficiently large, only the first term in Equation (1) is significant, all even terms are zero, and the sum of the remaining odd terms has little effect on the results. Thus, the dimensionless differential gas pressure is as follows:

$$\Delta P_D = \frac{2 \left[ a(b^2 + \theta_1^2) + b\sqrt{(a^2 + \theta_1^2)(b^2 + \theta_1^2)} \right]}{\theta_1^4 + \theta_1^2(a + a^2 + b + b^2) + ab(a + b + ab)} \cdot e^{\alpha t}, \quad (4)$$

$$\alpha = \left( \frac{f_1 A k_g}{\mu_g L c_g} \right) \left( \frac{1}{V_u} + \frac{1}{V_d} \right), \quad (5)$$

where  $A$  is the cross-sectional area of the cylindrical core plug;  $k_g$  is the effective permeability to gas;  $c_g$  is the gas compressibility and given by  $c_g \equiv f_z/p$  ( $f_z$  is the gas compressibility correction factor, and  $p$  is the pore pressure);  $\mu_g$  is the viscosity of gas;  $V_u$  and  $V_d$  are the volumes of the upstream and downstream, respectively.

With the linear regression of Equation (4), slope  $\alpha$  of the late-time experimental data can be obtained. Thus, the gas effective permeability can be calculated by

$$k_g = - \frac{\alpha \mu_g L f_z}{f_1 A p_m ((1/V_u) + (1/V_d))}, \quad (6)$$

where  $p_m$  is the mean absolute pore pressure (the gas compressibility is evaluated at  $p_m$ ).

**3.2. Cui et al.'s Method (2009).** Considering the effect of adsorption on the permeability measurement, Cui et al. [2] combined the Langmuir isotherm adsorption model with Jones' simplified algorithm, and the adsorption term was introduced into the seepage equation to modify the traditional algorithm. The modified values of  $a$  and  $b$  are as follows:

$$a = \frac{V_p(1 + (\varnothing_a/\varnothing))}{V_u}, \quad (7)$$

$$b = \frac{V_p(1 + (\varnothing_a/\varnothing))}{V_d},$$

where  $V_p$  is the pore volume of the sample, and  $\varnothing_a$  is the effective porosity.

The effective porosity due to gas adsorption is as follows:

$$\varnothing_a = \frac{\rho_s}{V_{\text{std}}} \frac{(1-\varnothing)}{c_g \rho} \frac{q_L p_L}{(p_L + p)^2}, \quad (8)$$

where  $\rho_s$  is the skeleton density of the porous samples;  $\rho$  is the density of gas;  $q_L$  and  $p_L$  are the Langmuir volume and pressure, respectively;  $p$  is the gas pressure;  $c_g$  is the gas compressibility;  $V_{\text{std}}$  is the molar volume of gas at the standard pressure and temperature (i.e., 273.1 K and 101325 Pa).

Substituting  $a$  and  $b$  into Equation (2) and Equation (3), we obtain  $f_1$ . The permeability can be calculated by Equation (6). Both porosity and adsorption characteristic parameters are required in the permeability calculation when we use Cui et al.'s method. The sample in this experiment was collected in coal seam # 3 in Sihe coal mine, which is similar to the sample in Han et al.'s [15] and Sun's [16] studies. Based on their experimental results, it is reasonable to assume that the porosity is approximately 5%, the Langmuir volume is approximately  $40 \text{ cm}^3 \text{ g}^{-1}$ , and the Langmuir pressure is  $2 \times 10^6 \text{ Pa}$ .

## 4. Results and Discussion

**4.1. Measurement Results.** Thirty-two permeability measurements were conducted with helium and carbon dioxide under different pore pressures and pulse pressures using the transient technique. Figure 3 shows the typical curves (recorded in the experiment with the helium pressure of 1 MPa and the pulse pressure of 100 kPa) of the pressure difference between upstream and downstream  $\Delta P(t)$  with time and  $\ln(\Delta P(t)/\Delta P(0))$  with time. Although the designed initial pulse pressure is 100 kPa, the applied pressure difference ( $\Delta P'(0)$ ) between upstream and downstream is up to 216 kPa due to the effect of  $V_{\text{dead}}$ . The volume of the pipeline in the blue-shaded part (from the valve to the top face of the sample) in Figure 3 is  $V_{\text{dead}}$ , which causes the steep drop of  $\Delta P(t)$  (dotted line). The initial pulse pressure ( $\Delta P(0)$ ) is the actual pressure difference between the upper and lower surfaces of the coal sample without the effect of  $V_{\text{dead}}$ . All other fitted slopes of  $\ln(\Delta P(t)/\Delta P(0)) - t$  and corresponding calculated permeability are listed in Table 2.

**4.2. Comparison of the Carbon Dioxide Permeability of Coal Calculated by Jones' and Cui et al.'s Methods.** Both Jones' and Cui et al.'s methods were used to calculate the carbon dioxide permeability of coal in this study to investigate their differences. The main difference between these two methods is whether the density of adsorbed gas changes with time. In Jones' method, the control equation only contains the term of free gas. If we use Jones' method to calculate the carbon dioxide permeability of coal, the density of adsorbed gas remains constant during the experiment. In Cui et al.'s method, both free gas and adsorbed gas are considered. The results calculated by these two methods are shown in Figure 4. The relative error is defined as the ratio of the absolute values of the difference to the value calculated by Cui et al.'s method. The carbon dioxide permeability calculated by Cui et al.'s method is larger than that by Jones' method. In addition, when the pore pressure increases from 1 MPa to 4 MPa, the relative error decreases from 57% to 27%. Thus, the carbon dioxide permeability calculated by Jones' method is severely underestimated, and the underestimation declines with the increase in pore pressure. This phenomenon may be attributed to the sorption behavior between carbon dioxide and coal matrix. As shown in Figure 5, on the one hand, according to Feng et al. [4] and Wang et al. [17], it is reasonable to speculate that the pulse pressure may break the ad-/desorption balance between gas and matrix, which makes the free

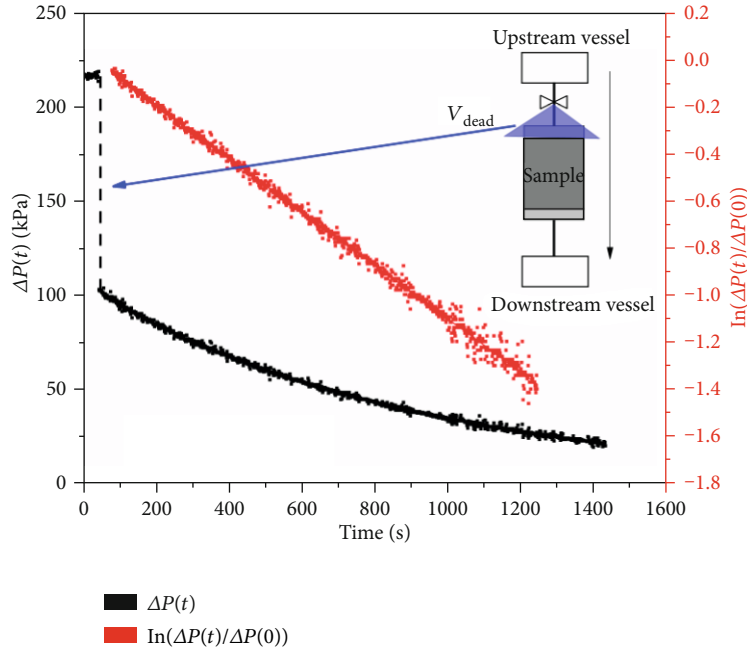


FIGURE 3: Typical curves of  $\Delta P(t) - t$  and  $\ln(\Delta P_t/\Delta P_0) - t$  measured in the experiment.

TABLE 2: Permeability measurement results under different conditions in the experiment.

Pore pressure (MPa)	Pulse pressure (kPa)	Helium			Carbon dioxide			
		Slope	$R^2$	$K$ ( $\mu\text{D}$ ) (Jones, 1997)	Slope	$R^2$	$K$ ( $\mu\text{D}$ ) (Jones, 1997)	$K$ ( $\mu\text{D}$ ) (Cui et al., 2009)
1	40	-0.0011	0.9843	5.86	-0.0441	0.9843	185.5	432.1
	60	-0.0011	0.9923	5.81	-0.0395	0.9936	163.52	379.13
	80	-0.0011	0.9951	5.77	-0.0375	0.9953	154.02	356.85
	100	-0.0011	0.9973	5.72	-0.0349	0.9974	141.13	323.91
2	40	-0.0017	0.9738	4.65	-0.0461	0.9519	97.4	164.71
	60	-0.0018	0.9885	4.88	-0.0407	0.9913	85.66	144.02
	80	-0.0018	0.99253	4.86	-0.038	0.9976	79.66	133.34
3	100	-0.0018	0.99503	4.84	-0.0354	0.9946	73.93	123.02
	40	-0.002	0.9819	3.68	-0.0307	0.9829	44.46	62.49
	60	-0.002	0.9907	3.67	-0.0289	0.9958	41.74	58.4
4	80	-0.002	0.9935	3.66	-0.0264	0.9957	37.85	53.34
	100	-0.002	0.9969	3.64	-0.0244	0.9979	34.98	49.01
	40	-0.0025	0.9777	3.47	-0.0199	0.9896	20.39	27.84
4	60	-0.0026	0.9904	3.6	-0.0175	0.9886	17.9	24.25
	80	-0.0026	0.9945	3.6	-0.0162	0.9973	16.51	22.37
	100	-0.0026	0.9967	3.58	-0.015	0.9964	15.29	20.85

gas change into adsorbed gas, and the real equilibrium pressure is less than the pseudoequilibrium pressure. On the other hand, the hysteresis of the downstream pressure caused by the adsorption of upstream gas may also change the differential pressure. For nonadsorbing gas, the decrease in upstream pressure will quickly trigger a response in the downstream and induce the increase in downstream pressure. For adsorbing gas, after the pulse pressure is applied, the upstream gas is adsorbed, and the response of the increase in downstream pressure becomes relatively slow.

Therefore, the differential pressure decay in the permeability measurement process is slower than that of nonadsorbing gas. If the adsorption effect is not considered in the calculation, the permeability will be underestimated. In addition, according to Langmuir isotherm, the carbon dioxide adsorption capacity, which is defined as the slope of the amount of gas adsorbed to the gas pressure, weakens with the increase in pore pressure. The hysteresis and deviation between real equilibrium pressure and pseudoequilibrium pressure are not apparent at high pressure. Thus, with the increase in pore

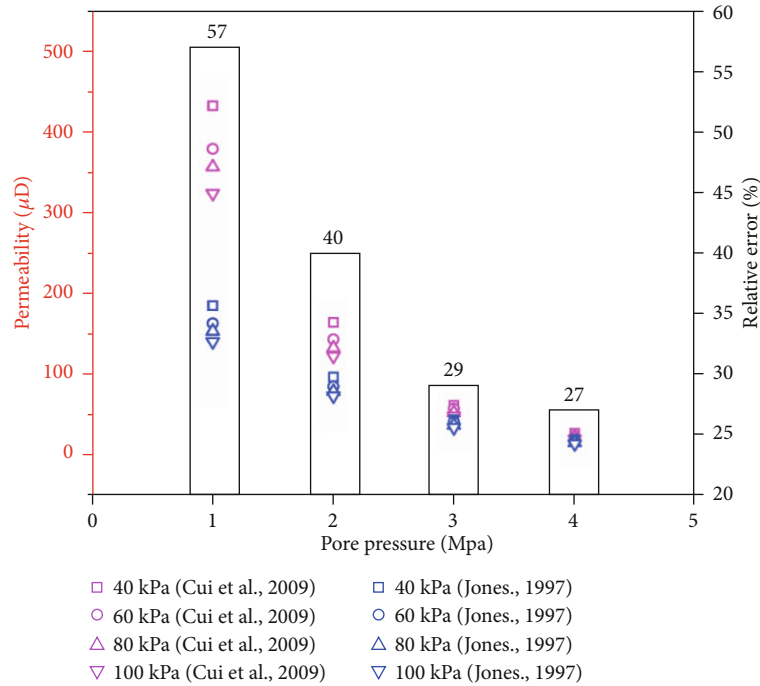


FIGURE 4: Comparison of the carbon dioxide permeability of coal calculated by Jones' and Cui et al.'s method.

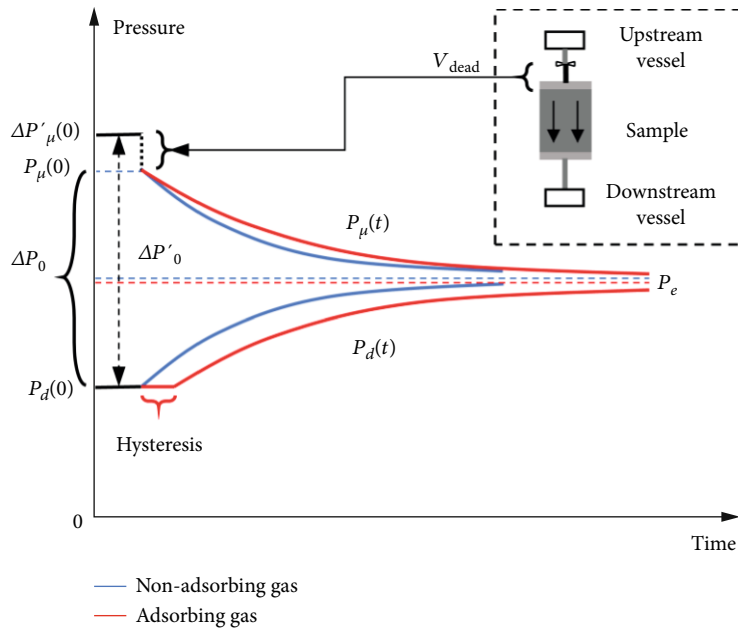


FIGURE 5: Change in pressure for adsorbing and nonadsorbing gases in the transient pulse-decay technique ( $P_u(t)$  and  $P_d(t)$  are the upstream pressure and downstream pressure, respectively;  $P'_u(0)$  and  $P_u(0)$  are the pseudo and actual upstream pressures, respectively (the difference between them is caused by  $V_{dead}$ );  $P_d(0)$  is the initial downstream pressure;  $P_e$  is the final equilibrium pressure; hysteresis is caused by the sorption of gas in the upstream).

pressure, the relative error between these two solutions decreases. Thus, when we test the adsorbing gas permeability of coal using the pulse-decay technique, the adsorption effect must be considered to accurately determine the measurement result. In this paper, the carbon dioxide permeability of coal is calculated by Cui et al.'s method, which better reflects the actual permeability of coal.

4.3. *Gas Permeability under Different Pore Pressures.* To further test the adsorption effect on the permeability of coal, we performed the gas permeability measurements under different pore pressures with PDM. The result is shown in Figure 6. In Figure 6(a), the permeability of helium decreases with the increase in pore pressure under constant net confining pressure, which was also observed by Chen et al. and Pan

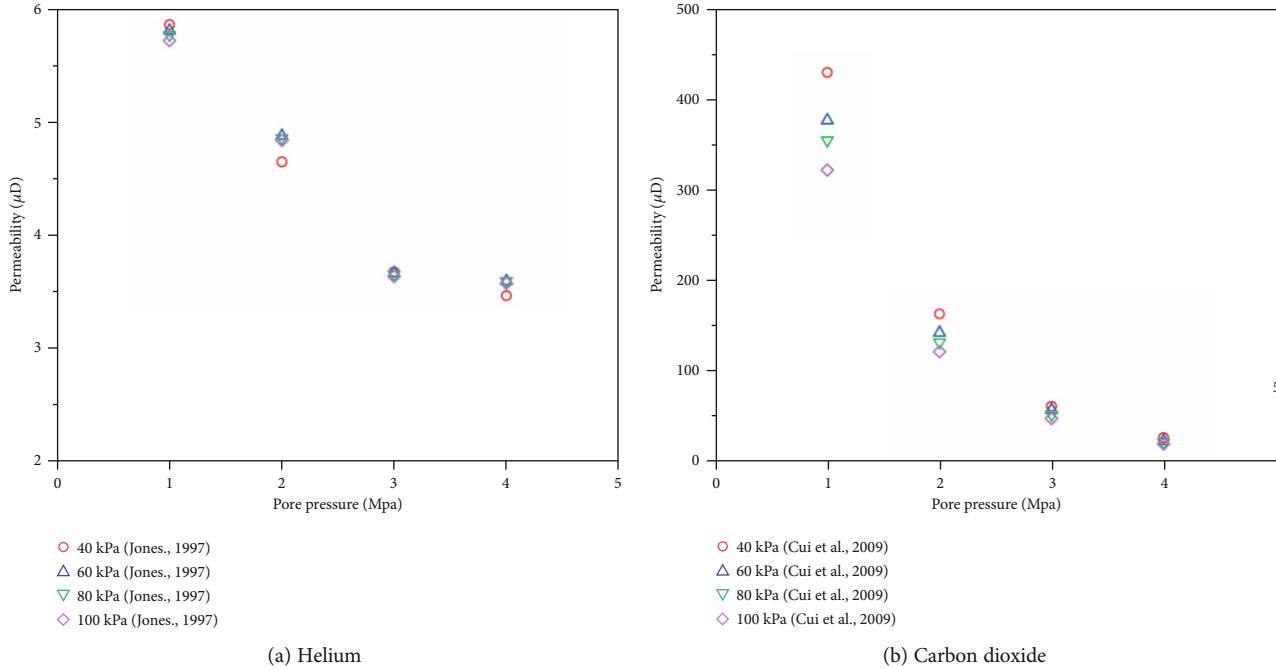


FIGURE 6: Gas permeability under different pore pressures (net confining pressure = 3 MPa).

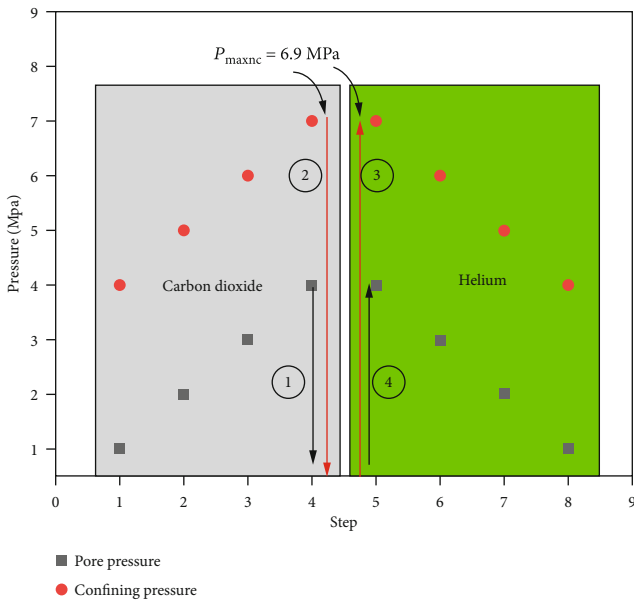


FIGURE 7: Experimental steps during the experiment.

et al. [18, 19]. When the pore pressure is 1 MPa, the measured permeability under different pulse pressures is 5.72-5.86  $\mu\text{D}$  with an average of 5.79  $\mu\text{D}$ . When the pore pressure increases to 2 MPa, the permeability is 4.65-4.88  $\mu\text{D}$  with an average of 4.81  $\mu\text{D}$ . When the pore pressure is 3 MPa, the permeability is 3.64-3.68  $\mu\text{D}$  with an average of 3.66  $\mu\text{D}$ . When the pore pressure continues to increase to 4 MPa, the permeability becomes 3.47-3.60  $\mu\text{D}$  with an average of 3.56  $\mu\text{D}$ . The decrease in permeability may be attributed to the combined impact of Klinkenberg effect [20] and effective stress effect.

On the one hand, Klinkenberg effect may significantly affect the gas flow behavior in low-permeability media [21–23]. In the experiment, when the pore pressure is low, the mean free path of helium molecules approaches the aperture of the coal cleats, and significant molecular collisions occur with the solid walls instead of other gas molecules [24]. Then, the gas permeability can be enhanced by the “slip flow.” Therefore, with the increase in pore pressure, the gas slippage effect diminishes, and the permeability decreases. On the other hand, based on the law of effective stress [25], the effective stress depends on the confining pressure, pore pressure, and effective stress coefficient. Zhao et al. [26] noted that the effective stress coefficient is not a constant for coal and is a bilinear function of volumetric stress and pore pressure. Thus, with the change in pore pressure, the effective stress coefficient may also change, which causes various permeabilities.

Similar to the result obtained in helium, the carbon dioxide permeability of coal decreases with the increase in pore pressure when the net confining pressure remains constant, as shown in Figure 6(b). The result is consistent with Chen et al. [19], Feng et al. [4], and Pan et al. [18]. The carbon dioxide permeability has a deeper decline with the increase in pore pressure than helium permeability. When the pore pressure increases from 1 MPa to 4 MPa, the carbon dioxide permeability decreases from approximately 400  $\mu\text{D}$  to 20  $\mu\text{D}$  (95% reduction), while the helium permeability only decreases from approximately 5.8  $\mu\text{D}$  to 3.5  $\mu\text{D}$  (40% reduction). In addition to Klinkenberg effect and effective stress effect, the adsorption effect may also decrease the permeability. Because carbon dioxide is an adsorbing gas to coal, it is well accepted that the decrease in permeability can be attributed to the swelling of the coal matrix induced by carbon dioxide adsorption [27–30].



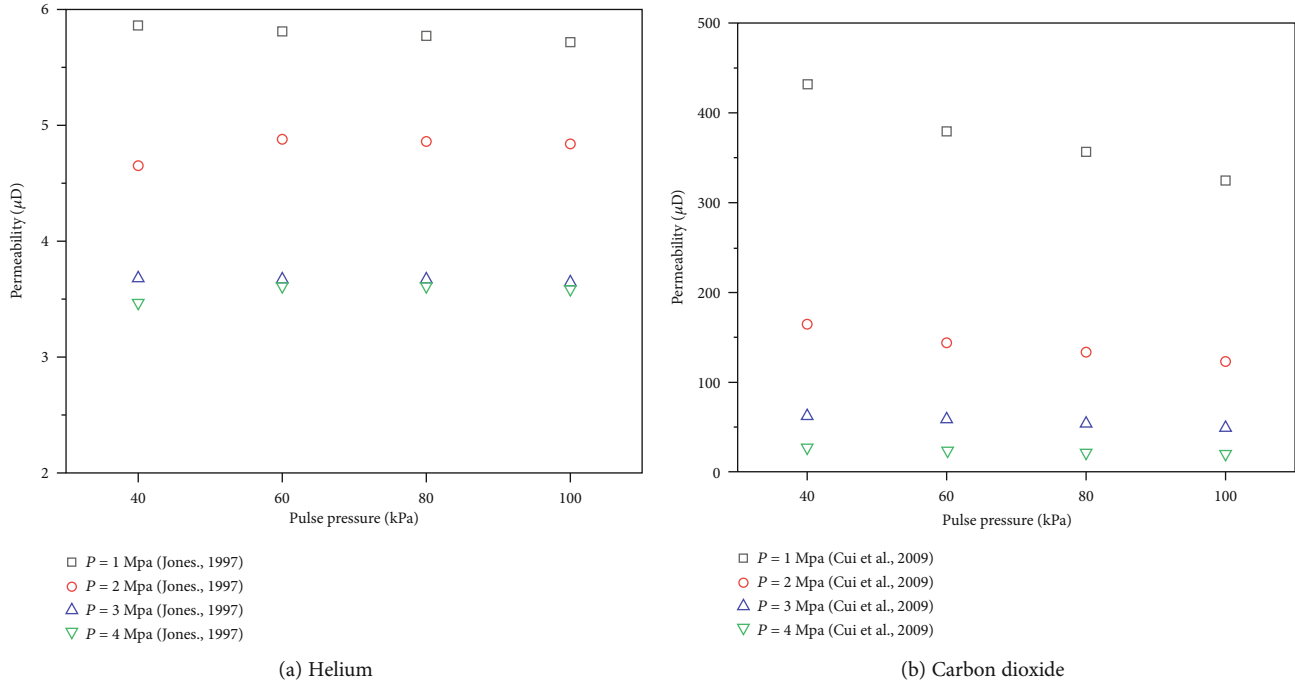


FIGURE 8: Gas permeability under different pulse pressures (net confining pressure = 3 MPa)

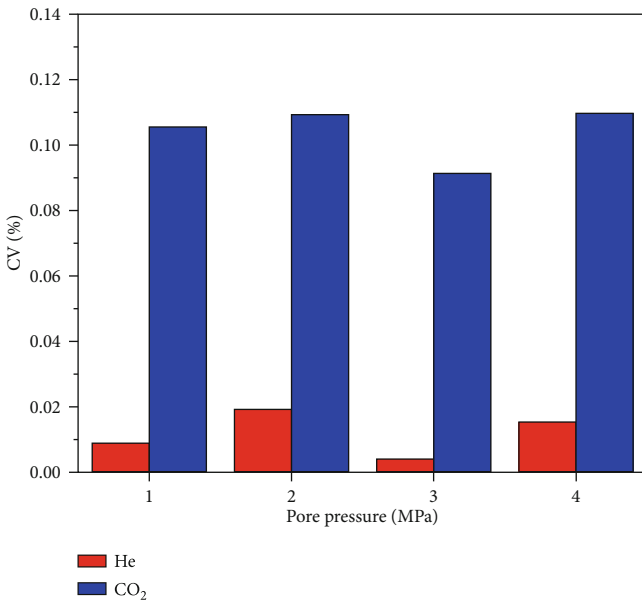


FIGURE 9: CV of the gas permeability measured by different pulse pressures under different pore pressures.

The permeability of coal tested by helium is obviously less than that tested by carbon dioxide, which may be related to the experiment process in our study. As shown in Figure 7, carbon dioxide was first used as the test fluid. It is commonly accepted that the change in pore structure induced by gas adsorption is irreversible [29, 31–33]. Thus, even when the carbon dioxide was released after the test, the pore structure of the coal will not revert to the original state. In addition, the permeability of coal is sensitive to stress [18, 34]. After step 4,

carbon dioxide was firstly exhausted (①); then, the confining pressure decreased (②). In this process, the maximum net confining pressure ( $P_{\max nc}$ ) is 6.9 MPa. Before the helium test (step 5), the confining pressure was first applied (③); then, helium was injected (④), and  $P_{\max nc}$  was also 6.9 MPa. Thus, the maximum net confining pressure of coal in history is 6.9 MPa before the helium test, which may also cause the decrease in coal permeability.

**4.4. Gas Permeability under Different Pulse Pressures.** To investigate the effect of the pulse pressure on the measurement of helium and carbon dioxide permeability of coal using the transient technique, a series of experiments were conducted, and the result is shown in Figure 8. Figure 8(a) visually shows the calculated values of helium permeability measured at each pulse pressure. With the increase in pulse pressure, the changing trend of helium permeability under different pore pressures is inconsistent. When the pore pressure is 1 MPa and 3 MPa, the calculated permeability decreases with the increase in pulse pressure. When the pore pressure is 2 MPa and 4 MPa, the permeability first increases and subsequently decreases. However, by comparing the decay curve of the pulse pressure, we easily find that the slope of  $\ln(\Delta P_t/\Delta P_0) - t$  is almost the same (Table 2) under different pulse pressures at each pore pressure condition. The fluctuation of the calculated permeability is attributed to the change in pore pressure, which changes the gas compressibility and viscosity. Generally, the change in helium permeability with pulse pressure is negligible, especially when the pulse pressure is 60–100 kPa.

The change in carbon dioxide permeability with pulse pressure is shown in Figure 8(b). The carbon dioxide permeability of coal decreases with the increase in pulse pressure, and the degree of permeability decrease is related to the pore

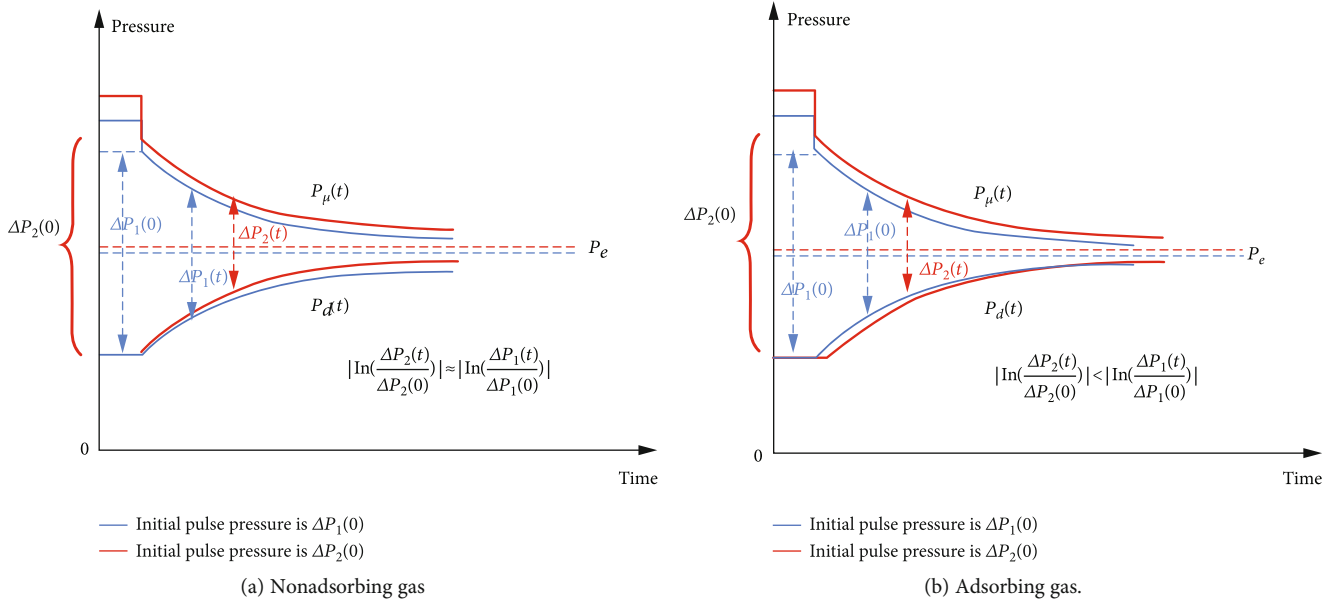


FIGURE 10: Changes of pressure for nonadsorbing and adsorbing gases under different pulse pressures in the transient technique.

pressure. In our experiment, when the pore pressure is 1 MPa, as the pulse pressure increases from 40 kPa to 100 kPa, the measured permeability decreases from 432.1  $\mu\text{D}$  to 323.91  $\mu\text{D}$ . When the pore pressure becomes to 2 MPa, the calculated permeability decreases from 164.71  $\mu\text{D}$  to 123.02  $\mu\text{D}$ . When the pressure further increases to 3 MPa and 4 MPa, the measured permeability only decreases from 62.49  $\mu\text{D}$  to 49.01  $\mu\text{D}$  and from 27.84  $\mu\text{D}$  to 20.85  $\mu\text{D}$ , respectively, i.e., it becomes relatively stable.

To illustrate and compare the degree of dispersion of the data measured by different pulse pressures under different pore pressures, the coefficient of variation (CV) was calculated, and the result is shown in Figure 9. The CV is extremely small for helium (less than 0.02) but greater than 0.1 for carbon dioxide. By comparing the CV of helium and carbon dioxide under each pore pressure, we find that the CV for carbon dioxide is at least five times larger than that for helium, which indicates that the carbon dioxide permeability of coal is more sensitive to the pulse pressure than the helium permeability.

The survey of the fitted slopes of  $\ln(\Delta P_t/\Delta P_0) - t$  for helium and carbon dioxide under different pulse pressures (Table 2) indicates that their difference may be attributed to the hysteresis caused by the adsorption effect. As shown in Figure 10(a), for nonadsorbing gas, with the decrease in pressure in the upstream, the pressure in the downstream can immediately respond. Thus, when the pulse pressure increases, the downstream pressure can correspondingly increase, and the differential pressure under different pulse pressures is almost constant. For adsorbing gas, as shown in Figure 10(b), due to the effect of hysteresis, the attenuation of the pressure difference between upstream and downstream slows down when the pulse pressure increases, which makes the permeability underestimated. Therefore, when the PDM is used to measure the permeability of coal, if the test fluid is carbon dioxide, the pulse pressure applied during the

experiment (within 10% of the pore pressure) will greatly affect the measurement result; if the test fluid is helium, its effect on the measurement result is negligible.

### 5. Conclusion

In this study, the PDM was employed to measure the gas permeability of coal. Both helium and carbon dioxide were used in our study, and the coal permeability was measured under different pore pressures and pulse pressures. According to the completed work, we made the following conclusions:

- (1) The carbon dioxide permeabilities of coal calculated by Jones' and Cui et al.'s methods show a great difference, which decreases with the increase in pore pressure. The difference may be attributed to the combined effect of gas adsorption and hysteresis of the downstream pressure, which decreases the differential pressure decay in the permeability measurement process. Thus, when measuring the permeability of coal with adsorbing gas, it is necessary to consider the adsorption effect
- (2) For nonadsorbing gas (helium), the calculated permeabilities under different pulse pressures are extremely similar, while for adsorption gas (carbon dioxide), the measured permeability greatly varies. The carbon dioxide permeability of coal is more sensitive to the pulse pressure than the helium permeability due to the adsorption effect

### Data Availability

The data used to support the findings of this study are available from the corresponding author upon request.

## Conflicts of Interest

The authors declare that they have no conflicts of interest.

## Acknowledgments

This work is supported by the National Key Research and Development Program of China (No. 2018YFB0605601).

## References

- [1] K. Coyner, T. Katsube, M. Best, and M. Williamson, "Gas and water permeability of tight shales from the venture gas field, offshore Nova Scotia," in *Papers-Geological Survey of Canada*, p. 129, GEOSCAN, 1993.
- [2] X. Cui, A. M. M. Bustin, and R. M. Bustin, "Measurements of gas permeability and diffusivity of tight reservoir rocks: different approaches and their applications," *Geofluids*, vol. 9, no. 3, pp. 208–223, 2009.
- [3] W. F. Brace, J. B. Walsh, and W. T. Frangos, "Permeability of granite under high pressure," *Journal of Geophysical Research*, vol. 73, no. 6, pp. 2225–2236, 1968.
- [4] R. M. Feng, S. Harpalani, and R. Pandey, "Evaluation of various pulse-decay laboratory permeability measurement techniques for highly stressed coals," *Rock Mechanics and Rock Engineering*, vol. 50, no. 2, pp. 297–308, 2017.
- [5] P. A. Hsieh, J. V. Tracy, C. E. Neuzil, J. D. Bredehoeft, and S. E. Silliman, "A transient laboratory method for determining the hydraulic properties of 'tight' rocks—I. Theory," *International Journal of Rock Mechanics and Mining Sciences & Geomechanics Abstracts*, vol. 18, no. 3, pp. 245–252, 1981.
- [6] A. I. Dicker and R. M. Smits, "A practical approach for determining permeability from laboratory pressure-pulse decay measurements," in *International Meeting on Petroleum Engineering*, pp. 285–292, Society of Petroleum Engineers, 1988.
- [7] S. C. Jones, "A technique for faster pulse-decay permeability measurements in tight rocks," *SPE Formation Evaluation*, vol. 12, no. 1, pp. 19–25, 2013.
- [8] K. Aminian and S. Ameri, "Predicting production performance of CBM reservoirs," *Journal of Natural Gas Science and Engineering*, vol. 1, no. 1-2, pp. 25–30, 2009.
- [9] P. N. K. De Silva, P. G. Ranjith, and S. K. Choi, "A study of methodologies for CO<sub>2</sub> storage capacity estimation of coal," *Fuel*, vol. 91, no. 1, pp. 1–15, 2012.
- [10] A. Ghanizadeh, M. Gasparik, A. Amann-Hildenbrand, Y. Gensterblum, and B. M. Krooss, "Experimental study of fluid transport processes in the matrix system of the European organic-rich shales: I. Scandinavian Alum Shale," *Marine and Petroleum Geology*, vol. 51, pp. 79–99, 2014.
- [11] A. Ghanizadeh, A. Amann-Hildenbrand, M. Gasparik, Y. Gensterblum, B. M. Krooss, and R. Littke, "Experimental study of fluid transport processes in the matrix system of the European organic-rich shales: II. Posidonia Shale (Lower Toarcian, northern Germany)," *International Journal of Coal Geology*, vol. 123, pp. 20–33, 2014.
- [12] M. Mahmoud, M. Eliebid, H. Y. al-Yousef, M. S. Kamal, K. al-Garadi, and S. Elkhatny, "Impact of methane adsorption on tight rock permeability measurements using pulse-decay," *Petroleum*, vol. 5, no. 4, pp. 382–387, 2019.
- [13] Z. Fang, X. Li, and L. Huang, "Laboratory measurement and modelling of coal permeability with different gases adsorption," *International Journal of Oil, Gas and Coal Technology*, vol. 6, no. 5, p. 567, 2013.
- [14] S. Mazumder, A. A. Karnik, and K.-H. A. A. Wolf, "Swelling of coal in response to CO<sub>2</sub> sequestration for ECBM and its effect on fracture permeability," *SPE Journal*, vol. 11, no. 3, pp. 390–398, 2013.
- [15] S. J. Han, S. X. Sang, J. J. Liang, and J. C. Zhang, "Supercritical-CO<sub>2</sub> adsorption in a simulated deep coal reservoir environment, implications for geological storage of CO<sub>2</sub> in deep coals in the southern Qinshui Basin, China," *Energy Science & Engineering*, vol. 7, no. 2, pp. 488–503, 2019.
- [16] J. Sun, *Adsorption Containment Mechanism of Supercritical CO<sub>2</sub> in Deep Anthracite Coal Reservoirs with CO<sub>2</sub>-ECBM*, China University of Mining and Technology, 2017.
- [17] Y. Wang, S. M. Liu, and D. Elsworth, "Laboratory investigations of gas flow behaviors in tight anthracite and evaluation of different pulse-decay methods on permeability estimation," *International Journal of Coal Geology*, vol. 149, pp. 118–128, 2015.
- [18] Z. J. Pan, L. D. Connell, and M. Camilleri, "Laboratory characterisation of coal reservoir permeability for primary and enhanced coalbed methane recovery," *International Journal of Coal Geology*, vol. 82, no. 3-4, pp. 252–261, 2010.
- [19] Z. W. Chen, Z. J. Pan, J. S. Liu, L. D. Connell, and D. Elsworth, "Effect of the effective stress coefficient and sorption-induced strain on the evolution of coal permeability: experimental observations," *International Journal of Greenhouse Gas Control*, vol. 5, no. 5, pp. 1284–1293, 2011.
- [20] L. J. Klinkenberg, "The permeability of porous media to liquids and gases," in *Drilling and Production Practice*, American Petroleum Institute, 1941.
- [21] D. C. Reda, "Slip-flow experiments in welded tuff: the Knudsen diffusion problem," in *Coupled Processes Associated with Nuclear Waste Repositories*, pp. 485–493, Elsevier, 1987.
- [22] W. Tanikawa and T. Shimamoto, "Comparison of Klinkenberg-corrected gas permeability and water permeability in sedimentary rocks," *International Journal of Rock Mechanics and Mining Sciences*, vol. 46, no. 2, pp. 229–238, 2009.
- [23] A. S. Ziarani and R. Aguilera, "Knudsen's permeability correction for tight porous media," *Transport in Porous Media*, vol. 91, no. 1, pp. 239–260, 2012.
- [24] Y.-S. Wu, K. Pruess, and Persoff, "Gas flow in porous media with Klinkenberg effects," *Transport in Porous Media*, vol. 32, no. 1, pp. 117–137, 1998.
- [25] M. A. Biot, "General theory of three-dimensional consolidation," *Journal of Applied Physics*, vol. 12, no. 2, pp. 155–164, 1941.
- [26] Y. S. Zhao, Y. Q. Hu, J. P. Wei, and D. Yang, "The experimental approach to effective stress law of coal mass by effect of methane," *Transport in Porous Media*, vol. 53, no. 3, pp. 235–244, 2003.
- [27] C. O. Karacan, "Heterogeneous sorption and swelling in a confined and stressed coal during CO<sub>2</sub> injection," *Energy & Fuels*, vol. 17, no. 6, pp. 1595–1608, 2003.
- [28] S. Kelemen, L. Kwiatek, and A. Lee, *Swelling and Sorption Response of Selected Argonne Premium Bituminous Coals to CO<sub>2</sub>, CH<sub>4</sub>, and N<sub>2</sub>*, International CBM Symposium, Tuscaloosa, Alabama, 2006.
- [29] C. O. Karacan, "Swelling-induced volumetric strains internal to a stressed coal associated with CO<sub>2</sub> sorption," *International Journal of Coal Geology*, vol. 72, no. 3-4, pp. 209–220, 2007.

- [30] H. Siriwardane, I. Haljasmaa, R. McLendon, G. Irdi, Y. Soong, and G. Bromhal, "Influence of carbon dioxide on coal permeability determined by pressure transient methods," *International Journal of Coal Geology*, vol. 77, no. 1-2, pp. 109–118, 2009.
- [31] Y. Liu, S. Cao, Y. Li et al., "Experimental study of swelling deformation effect of coal induced by gas adsorption," *Chinese Journal of Rock Mechanics and Engineering*, vol. 29, no. 12, pp. 2484–2491, 2010.
- [32] Z. Majewska, S. Majewski, and J. Ziętek, "Swelling of coal induced by cyclic sorption/desorption of gas: experimental observations indicating changes in coal structure due to sorption of CO<sub>2</sub> and CH<sub>4</sub>," *International Journal of Coal Geology*, vol. 83, no. 4, pp. 475–483, 2010.
- [33] D. Zhou, Z.-C. Feng, D. Zhao, Y.-S. Zhao, and T.-T. Cai, "Experimental study of meso-structural deformation of coal during methane adsorption-desorption cycles," *Journal of Natural Gas Science and Engineering*, vol. 42, pp. 243–251, 2017.
- [34] I. Palmer and J. Mansoori, "How permeability depends on stress and pore pressure in coalbeds: a new model," in *SPE Annual Technical Conference and Exhibition*, Denver, Colorado, October, 1996.

## Research Article

# A Crack Propagation Control Study of Directional Hydraulic Fracturing Based on Hydraulic Slotting and a Nonuniform Pore Pressure Field

Yugang Cheng <sup>1,2,3,4</sup>, Zhaohui Lu,<sup>2,3</sup> Xidong Du <sup>5</sup>, Xuefu Zhang,<sup>1</sup> and Mengru Zeng<sup>4</sup>

<sup>1</sup>State Key Laboratory of Mountain Bridge and Tunnel Engineering, Chongqing Jiaotong University, Chongqing 400074, China

<sup>2</sup>National and Local Joint Engineering Research Center of Shale Gas Exploration and Development, Chongqing Institute of Geology and Mineral Resources, Chongqing 400042, China

<sup>3</sup>Key Laboratory of Shale Gas Exploration, Ministry of Land and Resources, Chongqing Institute of Geology and Mineral Resources, Chongqing 400042, China

<sup>4</sup>School of Resources and Safety Engineering, Chongqing University, Chongqing 400030, China

<sup>5</sup>State Key Laboratory of Nuclear Resources and Environment, School of Earth Sciences, East China University of Technology, Nanchang, Jiangxi 330013, China

Correspondence should be addressed to Xidong Du; [xidongdu@126.com](mailto:xidongdu@126.com)

Received 27 April 2020; Revised 1 July 2020; Accepted 11 July 2020; Published 3 August 2020

Academic Editor: Mandadige S. A. Perera

Copyright © 2020 Yugang Cheng et al. This is an open access article distributed under the Creative Commons Attribution License, which permits unrestricted use, distribution, and reproduction in any medium, provided the original work is properly cited.

Hydraulic fracturing techniques for developing deeply buried coal reservoirs face routine problems related to high initial pressures and limited control over the fracture propagation direction. A novel method of directional hydraulic fracturing (DHF) based on hydraulic slotting in a nonuniform pore pressure field is proposed. A mechanical model is used to address crack initiation and propagation in a nonuniform pore pressure field, where cracks tend to rupture and propagate towards zones of high pore pressure for reducing the effective rock stress more. The crack initiation pressure and propagation morphology are analyzed by rock failure process analysis software. The numerical results show that the directional propagation of hydraulic fracturing cracks is possible when the horizontal stress difference coefficient is less than or equal to 0.5 or the slotting deviation angle is less than or equal to 30°. These findings are in good agreement with experimental results, which support the accuracy and reliability of the proposed method and theory.

## 1. Introduction

In 2018, the proportion of coal consumption declined to 27.2% in the global primary energy consumption structure while that of natural gas increased to 23.8%. The natural gas market has a strong development momentum, both production and consumption have achieved substantial growth. Efficient exploitation of coalbed methane (CBM), an important unconventional natural gas, is of significant demand for global coal production safety and poses an important strategy for energy structure optimization [1, 2]. China remains one of the world's largest energy consumer, accounting for more than 30% (34%) of the global net increase in

energy consumption in 2018. Despite their abundance of about 36.81 trillion m<sup>3</sup>, the occurrence conditions of CBM in China are extremely complex, with the prominent characteristics of low permeability and high geostress. Effective stress increases with CBM depth and can lead to restrained gas slippage and compressed coal seam cracks, which reduce coal seam permeability and complicate exploration [3].

With the development of science, engineering technology has gradually become refined in practical application. Hydraulic fracturing was first applied to the petroleum industry and then was subsequently applied to coal mines [4]. Now, it is one of the most effective methods to increase coal seam permeability [5–9]. In theory, the hydraulic

fracture orientation is dictated by and is perpendicular to the minimum in situ stress orientation [10]. However, certain problems controlled by original ground stresses (e.g., high initial pressure, single crack propagation direction) continue to pose practical challenges [11, 12]. In some cases, directional hydraulic fracturing (DHF) is more advantageous and efficient than conventional hydraulic fracturing [13]. For example, the treatment of high mining pressure on a coal seam goaf roof requires DHF to cut the hard rock [14–16]. Coal roadway driving also requires DHF to increase permeability and preextract gas from the coal seam along the preset direction [17, 18]. Initially, scholars used multihole drilling arrangements to relieve the stresses in a certain direction within the coal seam, while at the same time, controlling the expansion direction of hydraulic fracture [19]. Subsequently, some scholars put forward prefabricated artificial cracks in the coal seam to influence the hydraulic cracks based on the effect of hydraulic slotting [20, 21]. Then, DHF is gradually used to prevent rockburst or increase the permeability directionally in underground coal mining as a combination of hydraulic fracturing and multihole drilling or hydraulic slotting [17, 22, 23]. Compared with multihole drilling, hydraulic slotting offers improved control over the direction range of crack propagation from a single borehole. DHF experiments were first explored by Mizuta et al. but did not address how to expand fractures in a desired direction [24]. Yan et al. showed that certain hydraulic slotting arrangements can improve fracture control, which have been verified by gas field extraction experiments [22]. However, the variation of in situ stress and the angle of the maximum horizontal principal stress to the direction of hydraulic slot layout were not considered, both of which are critical to crack propagation and deflection [25]. Physical experiments and numerical analysis have also been used to investigate the relationship of a single hydraulic slot and its initial pressure and crack propagation behavior [26, 27], while practical applications must consider interactions between multiple drilling holes or slots. Although many scholars have made great breakthroughs in the method of DHF, the conditions under which the directional crack propagation can be controlled therefore remain poorly understood, in addition to the DHF crack propagation mechanism.

In this study, a new DHF method is proposed based on the integration of hydraulic slotting and a nonuniform pore water pressure gradient. We have designed a mechanical model that demonstrates the guiding control mechanism of hydraulic fracturing using a nonuniform pore water pressure gradient. Numerical analysis is used to constrain the relationship between the DHF crack propagation direction and two key parameters: (1) the coefficient of horizontal stress difference and (2) the angle between the hydraulic slotting and direction of maximum horizontal principal stress. The results are compared with physical experiments.

## 2. DHF Methodology and Inducing Theory by a Nonuniform Pore Water Pressure Gradient

*2.1. DHF Methodology.* The technical principles of crack propagation control using the DHF methods proposed in

this paper are shown in Figure 1. Hydraulic slotting is first used to form an orderly and consistent groove layout in the coal seam. Stable water pressure is then maintained in the slotting borehole prior to fracturing to form a nonuniform pore pressure gradient field. Hydraulic fracturing is then implemented, and hydraulic cracks are obtained in the desired direction.

DHF methods based on the integration of hydraulic slotting and nonuniform pore water pressure gradient show strategic advantages over conventional hydraulic fracturing. For example, the original stress field surrounding the slot can be redistributed with the aid of a water jet. A DHF zone is built where the maximum principal stress exceeds the original stress, and the direction of the former is then deflected from the original horizontal orientation into the slotting direction. The original in situ stress can thus be overcome, and control of the fracturing crack propagation direction can be obtained [28, 29]. Another advantage of this approach is that a nonuniform pore pressure gradient can form in the coal mass upon the injection of water in different boreholes, which reduces the effective stress and energy required for crack expansion [30]. Altammar et al. have proved that hydraulic fracture trajectories and fracturing pressures can be significantly affected by injection-induced stress through an experimental study [31]. Therefore, a theoretical analysis of the effect of pore pressure field on fracture initiation and propagation pressure was studied in this study.

The proposed method combines hydraulic slotting with a nonuniform pore pressure gradient to expand hydraulic fracturing cracks and transform in situ stress. Reasonable borehole arrangement, hydraulic slotting, water injection, hydraulic fracturing, and other steps, as described in the following sections, can improve hydraulic crack initiation, expand crack extension, and meet engineering requirements regarding the orientation or specified location of propagated cracks to increase coal seam permeability.

The transformation of a coal body's stress field by hydraulic slotting has been described in detail in literature and is not included here [18]. The following section is a theoretical explanation of the effects of nonuniform pore pressure gradient on the initiation and fracture propagation pressures.

### 2.2. Effects of a Nonuniform Pore Pressure Gradient on the Directional Crack Propagation Mechanism

*2.2.1. Effect of Nonuniform Pore Water Pressure on the Fracture Initiation Pressure.* The stress state of a borehole perpendicular to a coal seam is shown in Figure 2. A guiding borehole is set near the hydraulic fracturing borehole to study the effect of a nonuniform pore pressure gradient. High-pressure water is injected into the guiding borehole to form a nonuniform pore pressure gradient in the coal seam, which affects the stress of the hydraulic fracturing borehole.

When the effect of a nonuniform pore water pressure gradient is not taken into account, the stress state of the fracturing borehole wall can be expressed as Equation (1) [32–34]. The stress state of the fracturing borehole wall in Equation

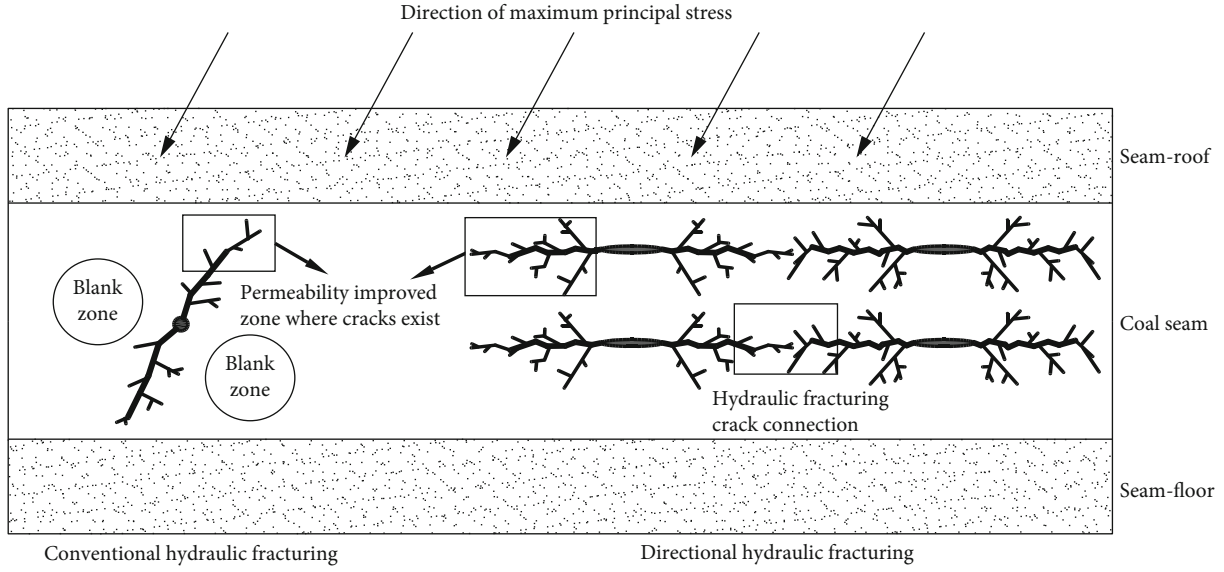


FIGURE 1: Schematic diagram of directional hydraulic fracturing (DHF) based on hydraulic slotting and a nonuniform pore pressure gradient.

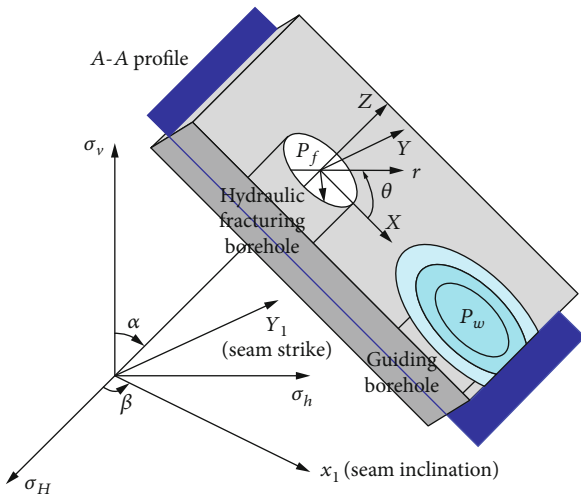


FIGURE 2: Stress state of a borehole under a nonuniform pore pressure gradient.

(1) was calculated in the cylindrical coordinate of  $(X, Y, Z)$ , which was transferred from the coordinate of in situ rock stress  $(\sigma_H, \sigma_h, \sigma_v)$  [35].

$$(1) \quad \begin{cases} \sigma_r = p_f, \\ \sigma_\theta = (\sigma_x + \sigma_y) - 2(\sigma_x - \sigma_y) \cos 2\theta - 4\tau_{xy} \sin 2\theta - p_f, \\ \sigma_{zz} = \sigma_z - \nu [2(\sigma_x + \sigma_y) \cos 2\theta + 4\tau_{xy} \sin 2\theta], \\ \tau_{\theta z} = 2\tau_{yz} \cos \theta - 2\tau_{xz} \sin \theta, \\ \tau_{r\theta} = \tau_{zr} = 0, \end{cases}$$

where  $\sigma_v$  is the vertical principal stress,  $\sigma_H$  and  $\sigma_h$  are the maximum and minimum horizontal principal stresses in the coordinate of in situ rock stress, respectively,  $p_f$  is the water pressure in the hydraulic fracturing borehole, and  $\sigma_r, \sigma_\theta, \sigma_{zz}, \tau_{r\theta}, \tau_{\theta z}$ , and  $\tau_{zr}$  are the radial, tangential, and axial components of the normal and shear stresses at the hydraulic fracturing borehole wall inclined at an angle of  $\theta$  with  $\sigma_y$ , respectively.

Figure 2 shows a coal seam that is cut along the  $A-A$  plane, and the stress variation of the fracturing borehole wall is shown in Figure 3. The guiding borehole is assumed to maintain a stable injection of high-pressure water in the coal seam reservoir with an influence range  $R$ . According to the thick-wall planar radial flow theory, the pressure distribution equation and boundary conditions at a distance  $d$  from the guiding borehole can be written as

$$\begin{cases} \frac{d}{dd} \left( d \frac{dp}{dd} \right) = 0, (r_w \leq d \leq R), \\ p(d = r_w) = p_w, \\ p(d = R) = p_o, \end{cases} \quad (2)$$

where  $r_w$  is the radius of the guiding borehole,  $p_w$  is the control water pressure in the guiding borehole, and  $p_o$  is the original pore water pressure of the coal seam. The pore pressure variation within  $R$  of the guiding borehole can be obtained as

$$p' = p_w - \frac{p_w - p_o}{\ln(R/r_w)} \ln \frac{d}{r_w}. \quad (3)$$

According to the principle of effective stress, stresses change in the vicinity of the hydraulic borehole within  $R$ . Since the pore water pressure only affects the normal stress,

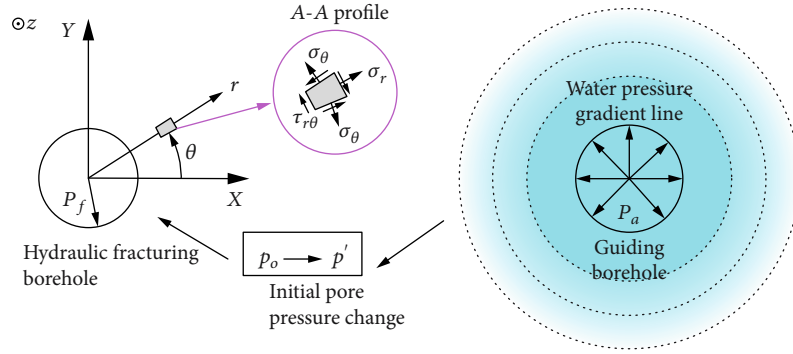


FIGURE 3: The formation of nonuniform pore pressure field and its influence on fracturing borehole stress.

it has no effect on the shear stress. The normal stress in Equation (1) can therefore be rewritten as

$$\begin{cases} \bar{\sigma}_x = \sigma_x - p', \\ \bar{\sigma}_y = \sigma_y - p'. \end{cases} \quad (4)$$

Fluid loss can occur at the fracturing borehole wall due to differences between the water pressure in the fracturing borehole and the pore pressure of the coal seam, which cause variation of the stress surrounding the borehole. According to the thermoelastic stress solution for a thick-walled cylinder, the change of tangential stress on the wall can be obtained as

$$\Delta\sigma_\theta = (p_f - p')\varphi \frac{1-2\nu}{1-\nu}, \quad (5)$$

where  $\varphi$  is the Biot constant of the coal seam and  $\nu$  is Poisson's ratio. The tangential stress is therefore modified to

$$\sigma_\theta' = \sigma_\theta + \Delta\sigma_\theta. \quad (6)$$

When the wall of the pressure-cracked hole is damaged,

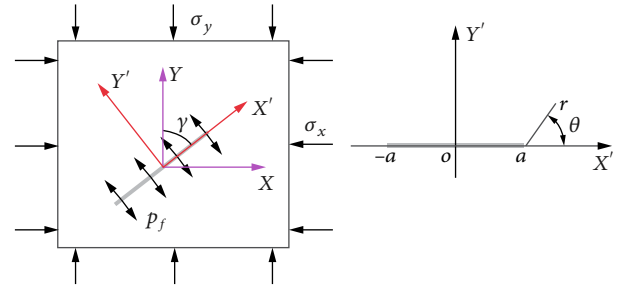


FIGURE 4: Stress state of a propagating crack.

Equation (6) should be met according to the maximum tensile strength failure criterion of the borehole wall:

$$|\sigma_\theta'| \geq Rt, \quad (7)$$

where  $Rt$  is the tensile strength of rock around the borehole wall.

In the presence of a nonuniform pore water pressure gradient, the critical fracture initiation pressure of the fracturing borehole can be expressed as

$$p_f = \frac{\sigma_x + \sigma_y - 2(\sigma_x - \sigma_y) \cos 2\theta - 4\tau_{xy} \sin 2\theta + Rt - (\varphi((1-2\nu)/(1-\nu)) + 2)(p_w - ((p_w - p_o)/(\ln(R/r_w))) \ln(d/r_w))}{1 - \varphi((1-2\nu)/(1-\nu))}. \quad (8)$$

Poisson's ratio of rock material is always less than 0.5, such that  $\varphi((1-2\nu)/(1-\nu)) + 2 > 0$ . When high-pressure water is injected into the guiding borehole,  $p'$  is higher than  $p_o$ . Assuming that other parameters remain constant, the pore water pressure gradient field formed by the guiding borehole will reduce the initial fracture pressure of the hydraulic fracturing borehole, that is, the borehole will preferentially crack in the direction of the directional borehole because it is the region where the pore pressure has a higher increase.

**2.2.2. Effect of Nonuniform Pore Water Pressure on Crack Propagation Pressure.** A crack propagated in a fracturing

borehole is affected by the nonuniform pore pressure gradient. The following is an analysis of the extended crack pressure. The stress state of a propagating crack of arbitrary width is shown in Figure 4.

By transforming the  $xoy$  coordinate system in Figure 4 into the crack coordinate system  $x'oy'$ , the stress state of the crack affected by in situ stress can be obtained as

$$\begin{cases} \sigma_x' = -(\sigma_x \sin^2 \gamma + \sigma_y \cos^2 \gamma), \\ \sigma_y' = -(\sigma_x \cos^2 \gamma + \sigma_y \sin^2 \gamma), \\ \tau_{xy} = (\sigma_x - \sigma_y) \sin \gamma \cos \gamma. \end{cases} \quad (9)$$



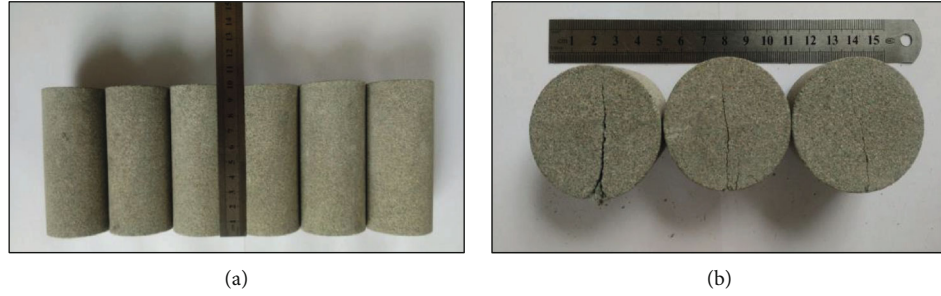


FIGURE 5: Uniaxial compression test specimen and failure results.

TABLE 1: Physical and mechanical properties of sandstone used in the numerical model.

Category	Density (kg/m <sup>3</sup> )	Tensile strength (MPa)	Compressive strength (MPa)	Poisson's ratio	Elastic modulus (GPa)
Sandstone	2333	4.09	56.4 MPa	0.24	36 GPa

Previous studies have often characterized rock mass under a complex stress state as a I-II composite. Here, pure type II cracks are not treated under strong compressional shear action. When the effects of the induced pore are ignored, the circumferential tensile strain of a I-II composite crack of length  $2a$  (Figure 4) is obtained as

$$\varepsilon_{\theta} = \frac{1}{2E\sqrt{2\pi r}} \left[ \begin{array}{l} K_{\text{I}} \cos \frac{\theta}{2} (1 - 3\nu + \cos \theta + \nu \cos \theta) - \\ K_{\text{II}} \left( 3 \cos \frac{\theta}{2} \sin \theta + 3\nu \sin \frac{\theta}{2} \cos \theta - \nu \sin \frac{\theta}{2} \right) \end{array} \right], \quad (10)$$

where  $K_{\text{I}}$  and  $K_{\text{II}}$  are the stress intensity factors of type I and type II cracks, respectively, and the stress intensity factor in Equation (10) is given as

$$\begin{cases} K_{\text{I}} = [p_f - (\sigma_x \sin^2 \gamma + \sigma_y \cos^2 \gamma)] \sqrt{\pi a}, & K_{\text{I}} > 0, \\ K_{\text{II}} = (\sigma_x - \sigma_y) \sin \gamma \cos \gamma \sqrt{\pi a}. \end{cases} \quad (11)$$

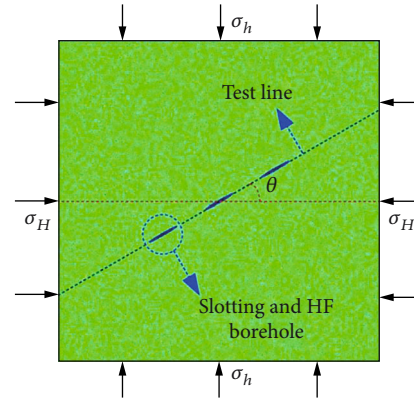
According to maximum circumferential tensile strain theory, a crack expands when  $\varepsilon_{\theta}$  reaches the critical value  $\varepsilon_e$ , namely:

$$\varepsilon_{\theta} = \varepsilon_e. \quad (12)$$

Such that the water pressure in the propagated crack can be obtained as

$$p_f = \frac{2E\varepsilon_e \sqrt{2r} + B \sin \gamma \cos \gamma \sqrt{a} (\sigma_x - \sigma_y)}{A \cos(\theta/2) \sqrt{a}} + \sigma_x \sin^2 \gamma + \sigma_y \cos^2 \gamma - \left( p_w - \frac{p_w - p_o}{\ln(R/r_w)} \ln \frac{d}{r_w} \right), \quad (13)$$

where  $A = 1 - 3\nu + \cos \theta + \nu \cos \theta$  and  $B = 3 \cos(\theta/2) \sin \theta + 3\nu \sin(\theta/2) \cos \theta - \nu \sin(\theta/2)$ .

FIGURE 6: Model design in the numerical analysis:  $\theta$  represents the slotting deviation angle.

A comparison of Equations (8) and (13) shows that the effect of a nonuniform pore water pressure gradient formed by the guiding borehole on the crack propagation pressure is consistent with the crack initiation pressure. Due to the self-organizing behavior of crack propagation, the crack will expand in the direction of the lowest propagation pressure to reduce the energy required for expansion. The formation of a nonuniform pore water pressure gradient can therefore effectively induce crack propagation. It is worth noting that higher water pressure in the guiding borehole and a closer distance from the hydraulic fracturing borehole both lead to stronger crack initiation and propagation-induced effects by the guiding borehole.

### 3. Numerical Analysis of DHF Crack Morphology

The coupled analysis of flow and solid mechanics in rock failure process analysis software (RFPA<sup>2D</sup>-Flow) was used to study initial pressure and DHF crack propagation [36, 37]. The RFPA<sup>2D</sup>-Flow was developed by Dalian Mechanics Software Co. Ltd. (China), which was designed to simulate the fracture and failure processes of quasibrittle materials

TABLE 2: Loading cases considered in the numerical analysis.

Load cases	Maximum horizontal stress $\sigma_H$ (MPa)	Minimum horizontal stress $\sigma_h$ (MPa)	Horizontal stress difference coefficient $K_h$	Slotting deviation angle $\theta$ ( $^\circ$ )
1#	4.5	3	0.5	15 $^\circ$
2#	5.25	3	0.75	15 $^\circ$
3#	6	3	1	15 $^\circ$
4#	6.75	3	1.25	15 $^\circ$
5#	4.5	3	0.5	30 $^\circ$
6#	5.25	3	0.75	30 $^\circ$
7#	6	3	1	30 $^\circ$
8#	6.75	3	1.25	30 $^\circ$
9#	4.5	3	0.5	45 $^\circ$
10#	5.25	3	0.75	45 $^\circ$
11#	6	3	1	45 $^\circ$
12#	6.75	3	1.25	45 $^\circ$
13#	4.5	3	0.5	60 $^\circ$
14#	5.25	3	0.75	60 $^\circ$
15#	6	3	1	60 $^\circ$
16#	6.75	3	1.25	60 $^\circ$
17#	4.5	3	0.5	75 $^\circ$
18#	5.25	3	0.75	75 $^\circ$
19#	6	3	1	75 $^\circ$
20#	6.75	3	1.25	75 $^\circ$
21#	4.5	3	0.5	90 $^\circ$
22#	5.25	3	0.75	90 $^\circ$
23#	6	3	1	90 $^\circ$
24#	6.75	3	1.25	90 $^\circ$

[22]. The rock in RFP A<sup>2D</sup>-Flow was assumed as a brittle elastic material with residual strength, and its loading and unloading behaviors were in accordance with elastic damage mechanics. In addition, the fluid flow in rock follows Biot's theory.

*3.1. Material Parameters.* The authors have published relevant physical simulation experiments using sandstones in order to avoid the effects of excessive coal-derived native joints or cracks on the guiding cracks. The sandstones were taken from the Songzao coal mine area in Chongqing, China. The results can be found in the references [17, 18]. To facilitate comparison, the numerical simulation parameters used in this paper are also consistent with the physical simulation experiment. Figure 5 shows a  $\Phi 50\text{mm} \times 100\text{mm}$  standard cylindrical uniaxial compression test specimen made of sandstone and results after failure in the previous physical simulation experiment. The basic mechanical parameters of sandstone used in the model are listed in Table 1.

*3.2. Numerical Model Procedure.* The model design and stress loading method are shown in Figure 6. The model size is  $300 \times 300\text{mm}$ , and the grid is divided into a total of  $3.2 \times 10^5$  sections. The horizontal direction of the model is

loaded with the maximum horizontal principal stress. Three hydraulic slots are arranged in a straight line, and all slots would be injected with water pressure as hydraulic fracturing boreholes simultaneously. The slots are oval with axes of 3 and 30 mm, and the spacing between each slot is 30 mm. The initial water injection pressure inside each slot was set to 2 MPa with a 0.1 MPa increase in each following step size. Loading stopped upon the stabilization of propagated crack morphology.

Previous studies have shown that the most important factors affecting DHF crack propagation are the difference between horizontal stresses and the angle between the maximum principal stress and the slotting direction [25, 38], hereinafter referred to as the slotting deviation angle. In this study, the horizontal stress difference coefficient is used to reflect the horizontal principal stress difference during loading. The horizontal stress difference coefficient is calculated by

$$K_h = \frac{\sigma_H - \sigma_h}{\sigma_h}. \quad (14)$$

The depth of China's CBM development is generally 400-1000 m, and the horizontal stress difference coefficient in this range is generally 0.4-1.2. The slotting

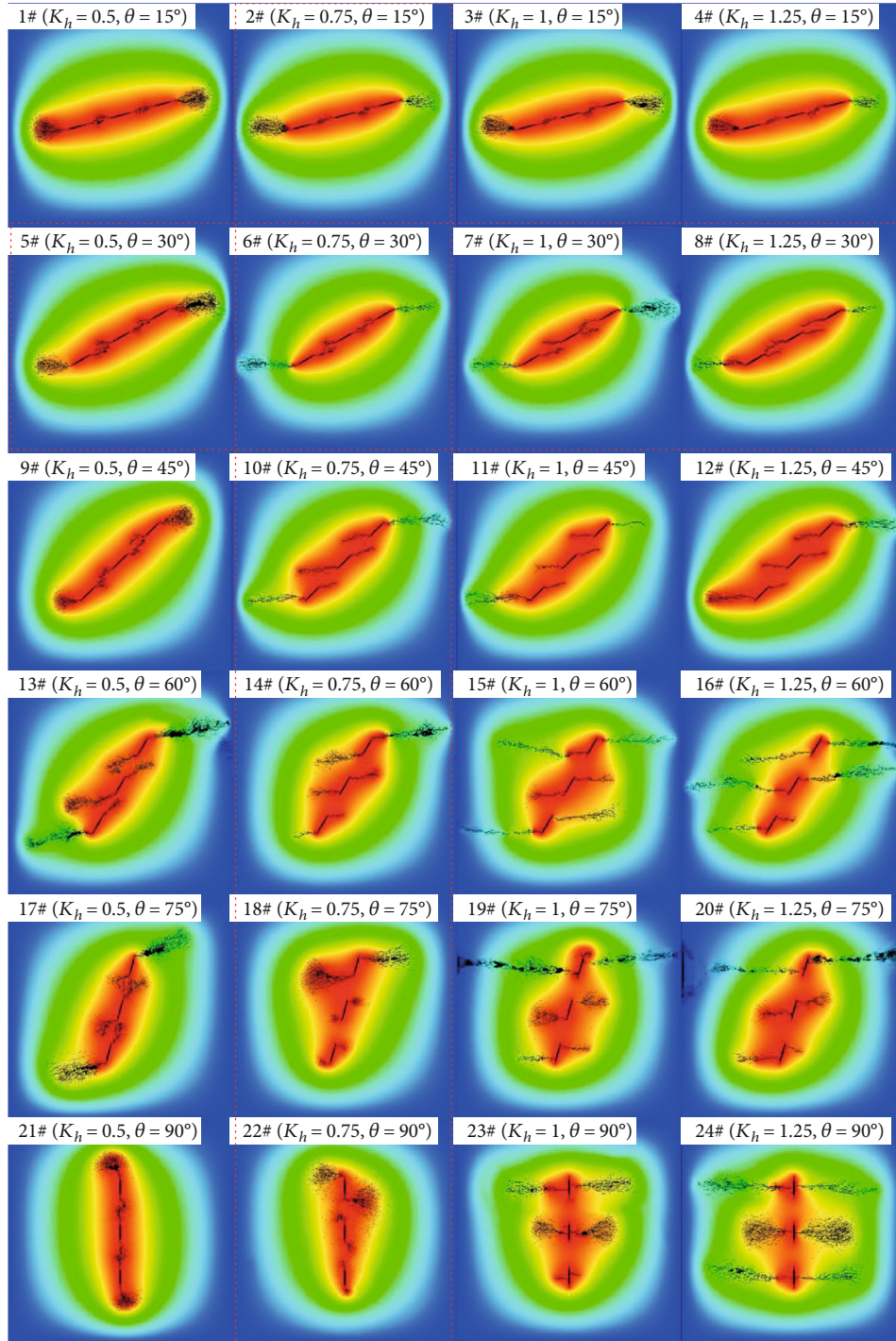


FIGURE 7: Crack propagation morphology of the 24 numerical model simulations.

deviation angle is  $0^\circ$  when the hydraulic slotting direction is parallel to the maximum horizontal principal stress direction and  $90^\circ$  when the directions are perpendicular to one another.

We designed 24 model sets with four horizontal stress difference coefficient values (0.5, 0.75, 1.0, and 1.25) and five slotting deviation angles ( $15^\circ$ ,  $30^\circ$ ,  $45^\circ$ ,  $60^\circ$ ,  $75^\circ$ , and  $90^\circ$ ). The model design number and specific stress loading sizes are listed in Table 2.

## 4. Numerical Results and Discussion

**4.1. DHF Crack Propagation Morphology.** The crack propagation morphology of 24 numerical model simulations was analyzed after extension to investigate how the horizontal stress difference coefficient and slotting deviation angle affect DHF, as shown in Figure 7. Two representative crack propagation groups are selected for comparison. The first group includes model numbers 5-8 with a fixed slotting deviation

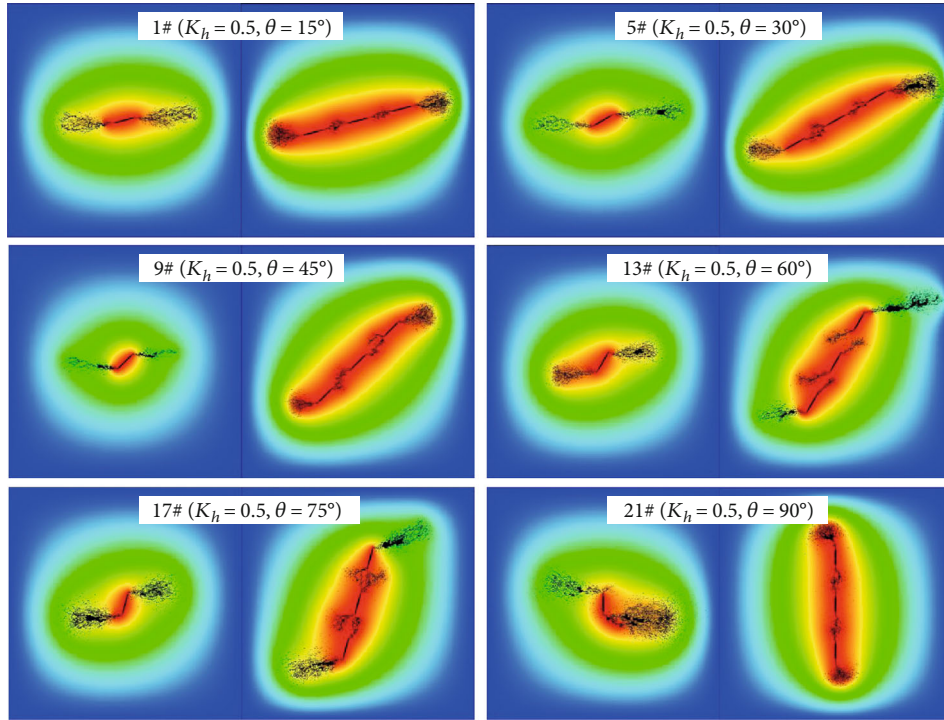
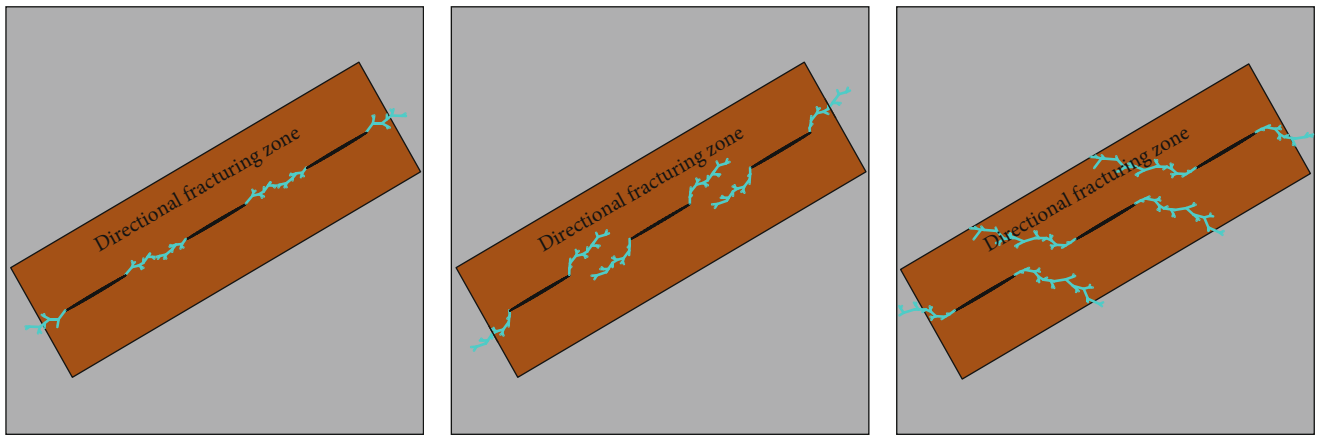


FIGURE 8: Crack propagation compared with a control group of simulations.



(a) The first crack propagation morphology

(b) The second crack propagation morphology

(c) The third crack propagation morphology

FIGURE 9: Three types of directional hydraulic fracturing (DHF) crack propagation morphology.

angle of  $30^\circ$ . As the horizontal stress difference coefficient increases from 0.5 to 1.25, the cracks start to propagate directly in the hydraulic fracturing zone and gradually spread outwards. The second group contains model numbers 2, 6, 10, 14, 18, and 22 with a fixed horizontal stress difference coefficient of 0.75. As the slotting deviation angle increases from  $15^\circ$  to  $90^\circ$ , the cracks gradually propagate out of the directional hydraulic fracturing zone. These findings indicate that larger horizontal stress difference coefficients and slotting deviation angles tend to produce a more unfavorable deviation of the cracks outside of the DHF induction zone.

To better illustrate the feasibility of the DHF method, we performed a control group of simulations. All the models in the first column of Figure 7 capable of DHF were selected, namely, models 1#, 5#, 9#, 13#, 17#, and 21#, for comparison, which the slotting deviation angle varies from  $15^\circ$  to  $90^\circ$  with a fixed horizontal stress difference coefficient of 0.5. The central slotting and HF borehole are preserved in the numerical model that means the stress field and pore water pressure gradient field between adjacent slots are not considered to induce crack propagation. The comparison results are shown in Figure 8. It can be seen that when there is no other slot near a slot, the hydraulic crack may initially rupture and

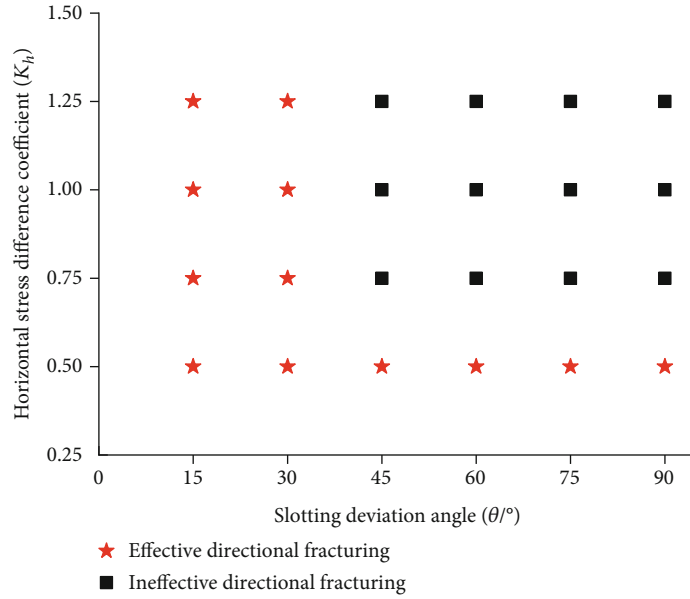


FIGURE 10: Effective directional fracturing results obtained from the 24 models.

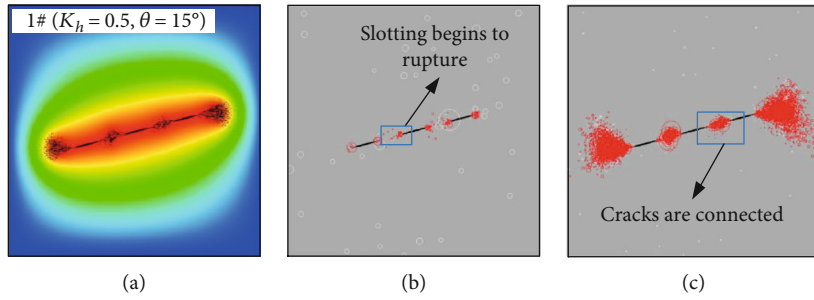


FIGURE 11: Acoustic emission events of model #1 during fracturing.

expand along the hydraulic slotting due to a certain angle of the slot. However, the maximum horizontal stress controls the direction of crack propagation rapidly. This means a single hydraulic slotting is insufficient to achieve DHF but requires interaction between a series of slots.

In addition, we separate the crack propagation results into three classification types based on morphology, as shown in Figure 9. The first crack propagation type includes direct (i.e., parallel) propagation in the DHF zone, demonstrating the best induction effects. Although the second crack pattern shows indirect crack propagation, the orientation is mostly parallel to the DHF inducing zone. The third crack type does not show a clear effect of the guiding borehole, and cracks tend to propagate along the direction of initial maximum principal stress. It is worth noting that a crack is still mainly controlled by the *in situ* stresses after propagating through the DHF inducing zone and steered to expand along the direction of maximum principal stress.

The crack propagation morphology results obtained from the 24 model simulations were statistically analyzed based on the classifications described above. The first two crack morphology types are regarded as effective directional fracturing, as shown in Figure 10. It can be seen that DHF

cracks only propagate directionally when the slotting deviation angle is less than or equal to  $30^\circ$  or the horizontal stress difference coefficient is less than or equal to 0.5. Cracks that form under other conditions are still mostly affected by the initial maximum principal stress.

4.2. Acoustic Emission Events and Initial Pressure Assessment.

We used acoustic emission (AE) images to determine and compare the cracking pressure from each model run. Figure 11 shows how the AE pattern changes during the fracturing process of model 1# with a slotting deviation angle of  $15^\circ$  and a horizontal stress difference coefficient of 0.5. The red and white circles in the figure represent the AE energy generated by tensile and compressive stress, respectively. The circle diameter represents the AE energy magnitude, and the number of circles shows the number of AE events. Figure 11(b) shows some typical tensile damage AE events at the slot tip, which represents the rupture onset. We consider the water injection pressure at this step to be the cracking pressure.

4.3. Comparative Analysis of Crack Initiation Pressure and Propagation Morphology with Experimental Results. We have

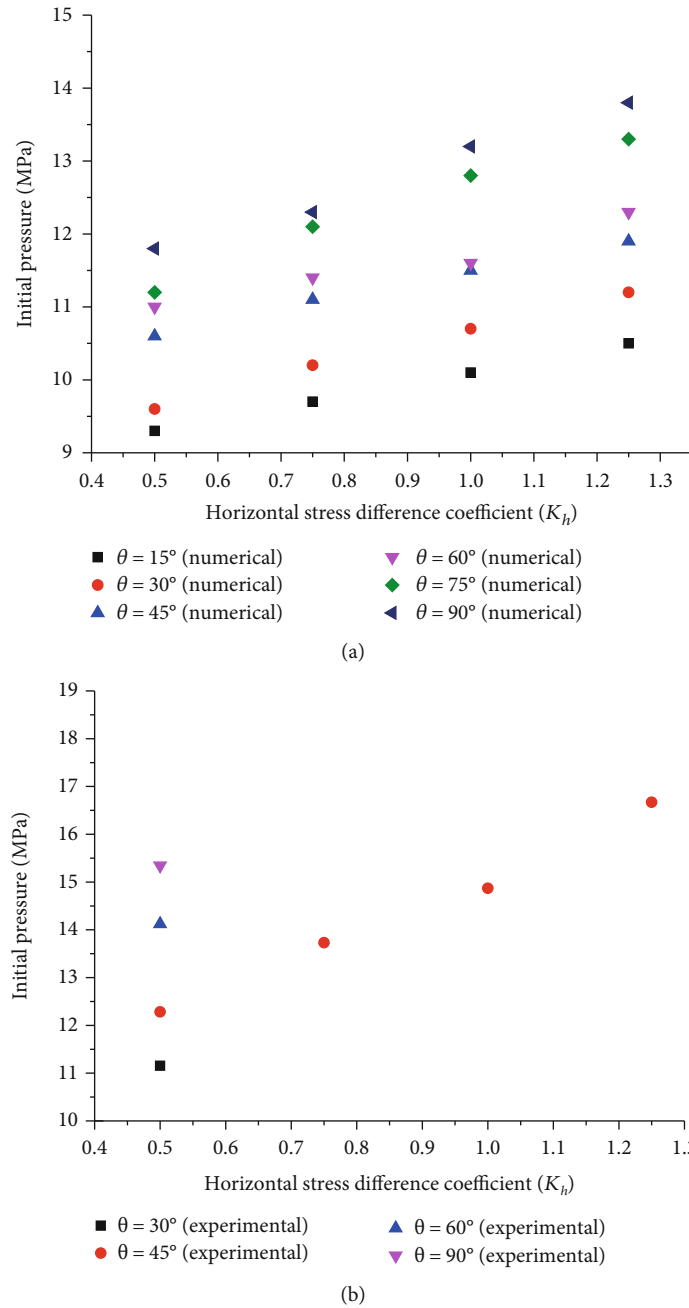


FIGURE 12: Variation of initial pressure under different conditions from (a) numerical calculation results and (b) physical experimental results [18].

previously reported results from similar and relevant physical DHF experiments. However, the experiments involved the filling of only the central slot with water, while the numerical calculations presented here involve the simultaneous injection of three slots with water and the effect of pore water pressure gradient is considered. Nevertheless, a comparison with experimental data is important for checking the validity of the numerical results.

The fracture initiation pressure of all model simulations (Table 2) was obtained from the AE-related information, and the variation law is shown in Figure 12(a). A gradual

increase of initial pressure is observed with an increase of both slotting deviation angle and horizontal stress difference coefficient. Figure 12(b) presents a summary of the primary initial pressure statistics obtained by the DHF experiments. The numerical results are in good agreement with the experimental data. However, initiation pressures calculated by numerical analysis are slightly lower than the experimental values obtained under the same conditions. This difference can be explained by the pore pressure gradients that form in the three model slotting boreholes due to simultaneous injection with water. Following the theoretical analysis

TABLE 3: Numerical model and corresponding physical experiment number.

Number	Horizontal stress difference coefficient $K_h$	Slotting deviation angle $\theta$ ( $^\circ$ )	Physical experiment number	Numerical model
1	0.5	$30^\circ$	Sample 1	5#
2	0.5	$45^\circ$	Sample 2	9#
3	0.5	$60^\circ$	Sample 3	13#
4	0.5	$90^\circ$	Sample 4	21#
5	0.75	$45^\circ$	Sample 5	10#
6	1.0	$45^\circ$	Sample 6	11#
7	1.25	$45^\circ$	Sample 7	12#

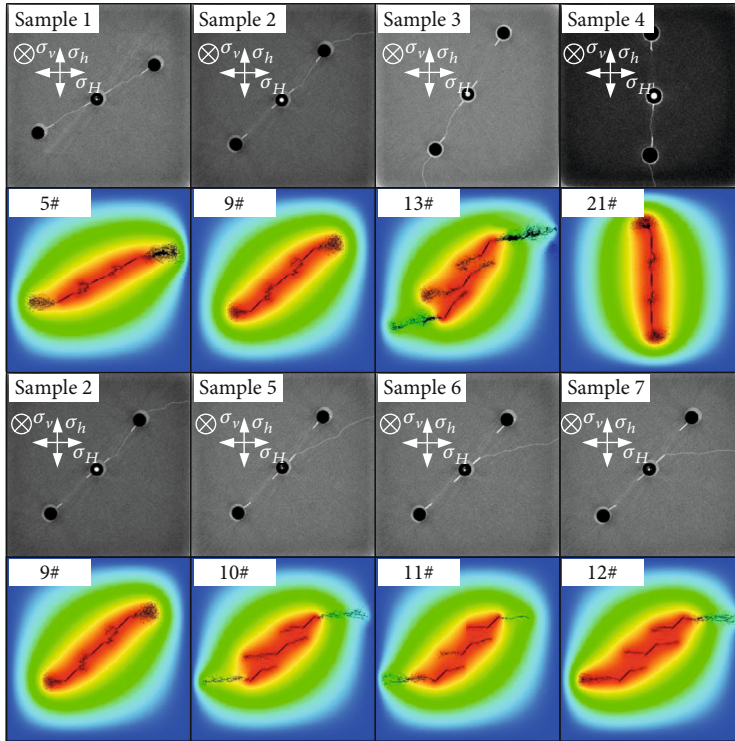


FIGURE 13: Comparison of crack propagation morphology between numerical calculations and physical experiments [18].

described in Section 2, a pore pressure gradient field can reduce the initial pressure, which explains the lower values derived from the model compared with the experiments.

Similarly, we compare crack propagation morphology obtained by numerical calculations with experimental results obtained under the same slotting deviation angle and horizontal stress difference coefficient. The corresponding relationship between physical experiments and numerical models is shown in Table 3.

Figure 13 shows CT images of the experimental cracks and numerical model crack propagation morphology. To study the influences of both preset slots and nonuniform pore pressure field on fracture propagation comprehensively, three slots were fractured simultaneously in the numerical model while only the center slot was fractured in previous physical experiments. Results obtained by the numerical calculation therefore provide more detailed insight into the

crack propagation controlled process. In general, both datasets show similar crack propagation morphology and direction. The crack orientation propagation conditions summarized in Section 4.1 are therefore verified by the experimental results.

Even though the crack propagation morphology of physical experiments and numerical simulation have high similarities, they are not exactly the same for the existence of pore water pressure gradient. As the horizontal stress difference coefficient increases (samples 2, 5, 6, and 7), the cracks in the experiments gradually deflected towards the maximum horizontal principal stress, while cracks obtained by numerical simulation under identical conditions expand in the DHF inducing zone, even in the absence of direct connection. Therefore, the induced crack propagation effect is improved obviously upon the formation of a pore water pressure gradient.

## 5. Conclusion

Based on this study, the main conclusions can be drawn as follows:

- (i) A novel method of DHF based on hydraulic slotting and a nonuniform pore pressure field is proposed in this paper. The hydraulic crack is oriented and extended using the two factors to disturb the local stress field of the rock. We have established a mechanical model of crack initiation and propagation by a nonuniform pore pressure field, which reveals the inducing effect of the nonuniform pore pressure field. The mechanical model shows that a pore water pressure gradient reduces the effective stress in the rock and that cracks tend to rupture and propagate towards higher pore pressure zones
- (ii) Crack orientation propagation conditions are clarified. That is, when horizontal stress difference coefficients are less than or equal to 0.5 or the slotting deviation angle is less than or equal to  $30^\circ$ , the crack can achieve directional expansion. The smaller the slotting deviation angle and the horizontal stress difference coefficient, the better the directional effect of the DHF
- (iii) The numerical results are verified by comparison with relevant experimental data. We compare and analyze the variation of crack initiation pressure and crack propagation morphology obtained from numerical analysis and physical experiments. Increased values of slotting deviation angle and/or horizontal stress difference coefficient lead to higher initial pressures, and a pore pressure gradient field can reduce the initial pressure. A comparison of the experimental and numerical results shows that the inducing effect improves in the presence of a pore pressure gradient field

## Data Availability

The data used to support the findings of this study are available from the corresponding author upon request.

## Conflicts of Interest

The authors declare that they have no conflicts of interest.

## Acknowledgments

This study was supported by the National Natural Science Foundation of China (No. 51904049), the Natural Science Foundation of Chongqing (General Program, No. cstc2019jcyj-msxmX0702), the Chongqing Science and Technology Innovation Talent Support Program (No. CSTCCXLJRC201712), and the Chongqing basic science and frontier technology research project (cstc2017jcyj BX0076).

## References

- [1] H. C. Lau, H. Y. Li, and S. Huang, "Challenges and Opportunities of Coalbed Methane Development in China," *Energy & Fuels*, vol. 31, no. 5, pp. 4588–4602, 2017.
- [2] Z. P. Meng, J. C. Zhang, and R. Wang, "In-situ stress, pore pressure and stress-dependent permeability in the Southern Qinshui Basin," *International Journal of Rock Mechanics and Mining Sciences*, vol. 48, no. 1, pp. 122–131, 2011.
- [3] S. M. Liu and S. Harpalani, "Determination of the Effective Stress Law for Deformation in Coalbed Methane Reservoirs," *Rock Mechanics and Rock Engineering*, vol. 47, no. 5, pp. 1809–1820, 2014.
- [4] B. X. Huang, Y. Z. Wang, and S. G. Cao, "Cavability control by hydraulic fracturing for top coal caving in hard thick coal seams," *International Journal of Rock Mechanics and Mining Sciences*, vol. 74, pp. 45–57, 2015.
- [5] J. C. Zhang and X. B. Bian, "Numerical simulation of hydraulic fracturing coalbed methane reservoir with independent fracture grid," *Fuel*, vol. 143, pp. 543–546, 2015.
- [6] Y. Y. Lu, F. Yang, Z. L. Ge, Q. Wang, and S. Q. Wang, "Influence of viscoelastic surfactant fracturing fluid on permeability of coal seams," *Fuel*, vol. 194, pp. 1–6, 2017.
- [7] L. Zhou and M. Z. Hou, "A new numerical 3D-model for simulation of hydraulic fracturing in consideration of hydro-mechanical coupling effects," *International Journal of Rock Mechanics and Mining Sciences*, vol. 60, pp. 370–380, 2013.
- [8] F. Hamidi and A. Mortazavi, "A new three dimensional approach to numerically model hydraulic fracturing process," *Journal of Petroleum Science and Engineering*, vol. 124, pp. 451–467, 2014.
- [9] X. Sun, S. Zhang, X. Ma, Y. Zou, and G. Lin, "Experimental Investigation on Propagation Behavior of Hydraulic Fractures in Coal Seam during Refracturing," *Geofluids*, vol. 2019, Article ID 4278543, 15 pages, 2019.
- [10] Q. Y. He, F. T. Suorineni, T. H. Ma, and J. Oh, "Effect of discontinuity stress shadows on hydraulic fracture re-orientation," *International Journal of Rock Mechanics and Mining Sciences*, vol. 91, pp. 179–194, 2017.
- [11] D. Q. Li, S. Zhang, and S. A. Zhang, "Experimental and numerical simulation study on fracturing through interlayer to coal seam," *Journal of Natural Gas Science and Engineering*, vol. 21, pp. 386–396, 2014.
- [12] Y. Liu, B. W. Xia, and X. T. Liu, "A novel method of orienting hydraulic fractures in coal mines and its mechanism of intensified conduction," *Journal of Natural Gas Science and Engineering*, vol. 27, pp. 190–199, 2015.
- [13] X. Fu, G. S. Li, Z. W. Huang, Y. S. Liang, Z. M. Xu, and X. Jin, "Experimental and numerical study of radial lateral fracturing for coalbed methane," *Journal of Geophysics and Engineering*, vol. 12, no. 5, pp. 875–886, 2015.
- [14] C. Lin, J. Q. Deng, Y. R. Liu, Q. Yang, and H. F. Duan, "Experiment simulation of hydraulic fracture in colliery hard roof control," *Journal of Petroleum Science and Engineering*, vol. 138, pp. 265–271, 2016.
- [15] B. Yu, R. Gao, T. J. Kuang, B. J. Huo, and X. B. Meng, "Engineering study on fracturing high-level hard rock strata by ground hydraulic action," *Tunnelling and Underground Space Technology*, vol. 86, pp. 156–164, 2019.
- [16] Y. J. Wang, J. Yang, M. C. He et al., "Test of a liquid directional roof-cutting technology for pressure-relief entry retaining



- mining,” *Journal of Geophysics and Engineering*, vol. 16, no. 3, pp. 620–638, 2019.
- [17] Z. Ge, J. Zhong, Y. Lu et al., “Directional distance prediction model of slotting–directional hydraulic fracturing (SDHF) for coalbed methane (CBM) extraction,” *Journal of Petroleum Science and Engineering*, vol. 183, article 106429, 2019.
- [18] Y. G. Cheng, Y. Y. Lu, Z. L. Ge, L. Cheng, J. W. Zheng, and W. F. Zhang, “Experimental study on crack propagation control and mechanism analysis of directional hydraulic fracturing,” *Fuel*, vol. 218, pp. 316–324, 2018.
- [19] W. Lu, Y. Wang, and X. Zhang, “Numerical Simulation on the Basic Rules of Multihole Linear Codirectional Hydraulic Fracturing,” *Geofluids*, vol. 2020, Article ID 6497368, 14 pages, 2020.
- [20] F. Gao, Y. Xue, Y. A. Gao, Z. Z. Zhang, T. Teng, and X. Liang, “Fully coupled thermo-hydro-mechanical model for extraction of coal seam gas with slotted boreholes,” *Journal of Natural Gas Science and Engineering*, vol. 31, pp. 226–235, 2016.
- [21] H. He, L. M. Dou, J. Fan, T. T. Du, and X. L. Sun, “Deep-hole directional fracturing of thick hard roof for rockburst prevention,” *Tunnelling and Underground Space Technology*, vol. 32, pp. 34–43, 2012.
- [22] F. Z. Yan, B. Q. Lin, C. J. Zhu et al., “A novel ECBM extraction technology based on the integration of hydraulic slotting and hydraulic fracturing,” *Journal of Natural Gas Science and Engineering*, vol. 22, pp. 571–579, 2015.
- [23] C. Zhai, M. Li, C. Sun, J. G. Zhang, W. Yang, and Q. G. Li, “Guiding-controlling technology of coal seam hydraulic fracturing fractures extension,” *International Journal of Mining Science and Technology*, vol. 22, no. 6, pp. 831–836, 2012.
- [24] Y. Mizuta, S. Kikuchi, and K. Tokunaga, “Studies on hydraulic fracturing stress measurement assisted by water jet borehole slotting,” *International Journal of Rock Mechanics and Mining Sciences & Geomechanics Abstracts*, vol. 30, no. 7, pp. 981–984, 1993.
- [25] D. S. Zhou, P. Zheng, P. He, and J. Peng, “Hydraulic fracture propagation direction during volume fracturing in unconventional reservoirs,” *Journal of Petroleum Science and Engineering*, vol. 141, pp. 82–89, 2016.
- [26] R. B. Mao, Z. J. Feng, Z. H. Liu, and Y. S. Zhao, “Laboratory hydraulic fracturing test on large-scale pre-cracked granite specimens,” *Journal of Natural Gas Science and Engineering*, vol. 44, pp. 278–286, 2017.
- [27] J. Q. Deng, C. Lin, Q. Yang, Y. R. Liu, Z. F. Tao, and H. F. Duan, “Investigation of directional hydraulic fracturing based on true tri-axial experiment and finite element modeling,” *Computers and Geotechnics*, vol. 75, pp. 28–47, 2016.
- [28] T. Liu, B. Q. Lin, W. Yang, Q. L. Zou, J. Kong, and F. Z. Yan, “Cracking Process and Stress Field Evolution in Specimen Containing Combined Flaw Under Uniaxial Compression,” *Rock Mechanics and Rock Engineering*, vol. 49, no. 8, pp. 3095–3113, 2016.
- [29] T. Liu, B. Q. Lin, Q. L. Zou, C. J. Zhu, C. Guo, and J. Li, “Investigation on mechanical properties and damage evolution of coal after hydraulic slotting,” *Journal of Natural Gas Science and Engineering*, vol. 24, pp. 489–499, 2015.
- [30] M. S. Bruno and F. M. Nakagawa, “Pore pressure influence on tensile fracture propagation in sedimentary rock,” *International Journal of Rock Mechanics and Mining Sciences & Geomechanics Abstracts*, vol. 28, no. 4, pp. 261–273, 1991.
- [31] M. J. AlTammar, M. M. Sharma, and R. Manchanda, “The Effect of Pore Pressure on Hydraulic Fracture Growth: An Experimental Study,” *Rock Mechanics and Rock Engineering*, vol. 51, no. 9, pp. 2709–2732, 2018.
- [32] J. S. Huang, D. V. Griffiths, and S. W. Wong, “Initiation pressure, location and orientation of hydraulic fracture,” *International Journal of Rock Mechanics and Mining Sciences*, vol. 49, pp. 59–67, 2012.
- [33] J. S. Huang, D. V. Griffiths, and S. W. Wong, “In situ stress determination from inversion of hydraulic fracturing data,” *International Journal of Rock Mechanics and Mining Sciences*, vol. 48, no. 3, pp. 476–481, 2011.
- [34] M. M. Hossain, M. K. Rahman, and S. S. Rahman, “Hydraulic fracture initiation and propagation: roles of wellbore trajectory, perforation and stress regimes,” *Journal of Petroleum Science and Engineering*, vol. 27, no. 3-4, pp. 129–149, 2000.
- [35] Y. Y. Lu, L. Cheng, Z. L. Ge, B. W. Xia, Q. Li, and J. F. Chen, “Analysis on the Initial Cracking Parameters of Cross-Measure Hydraulic Fracture in Underground Coal Mines,” *Energies*, vol. 8, no. 7, pp. 6977–6994, 2015.
- [36] L. C. Li, C. A. Tang, and Y. F. Fu, “Influence of heterogeneity on fracture behavior in multi-layered materials subjected to thermo-mechanical loading,” *Computational Materials Science*, vol. 46, no. 3, pp. 667–671, 2009.
- [37] C. A. Tang, L. G. Tham, P. K. K. Lee, T. H. Yang, and L. C. Li, “Coupled analysis of flow, stress and damage (FSD) in rock failure,” *International Journal of Rock Mechanics and Mining Sciences*, vol. 39, no. 4, pp. 477–489, 2002.
- [38] B. G. da Silva and H. H. Einstein, “Finite Element study of fracture initiation in flaws subject to internal fluid pressure and vertical stress,” *International Journal of Solids and Structures*, vol. 51, no. 23-24, pp. 4122–4136, 2014.